UNIVERSITÀ
DEGLI STUDI
DI PADOVA

Sede Amministrativa: Università degli Studi di Padova

Dipartimento di Ingegneria Civile, Edile e Ambientale

SCUOLA DI DOTTORATO DI RICERCA IN: SCIENZE DELL'INGEGNERIA CIVILE ED AMBIENTALE

INDIRIZZO: COSTRUZIONI IDRAULICHE

CICLO XXVII, 2012 - 2014

RAINFALL-TRIGGERED SHALLOW LANDSLIDES IN A LARGE-SCALE PHYSICAL MODEL

Direttore della Scuola: Ch.mo Prof. Stefano Lanzoni

Supervisori: Ch.mo Prof. Paolo Salandin

Ing. Matteo Camporese

Dottorando: Ing. Marco Lora

Dedication

Dedico questa tesi alle persone che amo. Alla mia famiglia prima di tutto dedico questo lavoro: a papà e mamma, ai mie fratelli e alle loro famiglie. In particolare ai miei nipoti, che conservano sempre per me sorrisi, abbracci e baci.

Dedico questi tre anni anche ai miei nonni: anche se per loro sarebbe stato difficile capire alcune mie scelte, spero che dall'alto mi accompagnino sempre, e mi auguro di assomigliare a loro crescendo.

Infine il mio pensiero va al mio dolce amore, alla compagna della mia vita, a te Jessica. Grazie.

Acknowledgements

I would like to express my gratitude to all people have helped me in this hard challenge. Specifically I want to thank the young boys that gave me hope and courage in these three years: Luca, Francesco and Michele. I think that the best result in this work consists of the relationships we can make by working together.

I want also to remember the great group of Biosphere 2: Nicolas and Charlene, Luke, Peter, Nathan, Michael, Wyatt Earp and all the other who supported me for 5 months. Thank you guys for enduring my bad accent and my difficulties in speaking English and for the enthusiasm you gave me in this work.

Finally I want to express my gratitude to Minseok and Yadi: they teach me that the true friendship does not come from our culture, or education, but It comes from our soul, from the richness that we transmit to each other.

Contents

List of Figures

List of Tables

Sommario

Le valutazioni di pericolosità sulle frane superficiali sono in genere estese su scala di versante, le cui limitate indagini geotecniche non consentono una caratterizzazione fedele che miri ad una comprensione dettagliata dei fenomeni di innesco. Per tale motivo, i processi fisici considerati nella spiegazione del fenomeno sono spesso riduttivi e tali da consentire una modesta risoluzione sia spaziale che temporale.

Tale approccio risulta utile per valutazioni legate alla previsione di innesco, e quindi, correttamente, non necessitano di un'elevata affidabilità nell'interpretazione del fenomeno idromeccanico, ma risultano compatibili con un'analisi sommaria e generalizzata.

Tuttavia, un'analisi a scala locale diventa necessaria quando sia richiesta una comprensione dettagliata del fenomeno di innesco che permetta di riconoscere gli elementi, e la loro intensità, nell'innesco delle frane superficiali. Tale esigenza può essere soddisfatta solo riproducendo dati sperimentali raccolti su siti a monitoraggio elevato.

Lo studio presente si occupa di un pendio artificiale per la simulazione dei fenomeni di innesco delle frane superficiali determinate da precipitazioni intense.

Il modello fisico consiste di un muro di contenimento in calcestruzzo armato: l'altezza massima è di 3.5 m, la lunghezza alla base è di 6 m e la larghezza di 2 m, così da realizzare una pendenza superficiale di 2:3.

Su ogni muro laterale, sono applicate 50 forature realizzate mediante tronchetti flangiati che consentono l'inserimento di 6 tensiometri e 6 sonde WCR (Water Content Reflectometer) nelle posizioni desiderate. La strumentazione è completata con 2 piezometri e due pozzetti per la misura delle portate di ruscellamento e sub-superficiale in uscita. Ogni misura viene acquisita e registrata mediante un sistema di acquisizione.

Il lavoro sviluppato riguarda la progettazione e l'analisi delle prestazioni dei principali dispositivi impiegati nel modello fisico, fino alla realizzazione di due prove sperimentali su uno strato di sabbia con spessore verticale di 60 cm.

Un simulatore di pioggia è stato progettato e realizzato per generare una precipitazione intensa tale da provocare l'instabilità del materiale posato nel modello fisico.

Il simulatore consiste in una rete ad anello chiuso sulla quale sono distribuiti degli ugelli appositamente scelti per evitare erosione sulla superficie del terreno dovuta all'impatto delle gocce erogate. In questo modo gli effetti indotti dalla precipitazione si riconoscono nei soli fenomeni di infiltrazione, senza innesco di processi erosivi che potrebbero aggiungere fenomeni di difficile comprensione. Le configurazioni degli ugelli distribuiti sul simulatore vengono scelte per coprire i) il campo desiderato delle intensità di pioggia, variante tra 50 e 150 mm/h, e per assicurare ii) un'elevata uniformità spaziale della precipitazione prodotta.

Un'attenta analisi è stata svolta per caratterizzare un singolo ugello mediante un apposito dispositivo, così da individuarne le principali variabili caratterizzanti il funzionamento e le prestazioni. Successivamente, l'indagine

sperimentale è stata concentrata sulla versione finale del simulatore di pioggia, al fine di definire le modalità di gestione e di regolazione della precipitazione riprodotta.

A seconda del campo di intensità desiderato, quattro differenti configurazioni di ugelli, distinte per il numero e la posizione degli ugelli attivi, sono state individuate per ricoprire l'intervallo totale di intensità da 50 a 150 mm/h.

Inoltre, è stata eseguita un'analisi per valutare i diametri delle gocce erogate mediante olio ad alta viscosità versato in dischetti Petri esposti alla pioggia artificiale. La distribuzione dei diametri così ottenuta è stata successivamente impiegata in un modello numerico per stimare la distribuzione dell'energia di impatto delle gocce sul suolo. Il modello numerico proposto calcola la traiettoria delle particelle erogate dall'ugello mediante una legge costitutiva basata sull'aerodinamica di sfere nello spazio 3D. I risultati hanno posto in evidenza la limitata erosione superficiale determinata dalla precipitazione erogata.

È stata poi realizzato un dispositivo per la calibrazione delle sonde WCR (Water Content Reflectometer), impiegate per la stima del contenuto volumetrico d'acqua del terreno. Il dispositivo consiste in un contenitore in Plexiglas di dimensione interne pari a 0.6 x 0.5 x 0.6 m^3, contenente il suolo che risulta libero nella parte superiore e, alla base, trattenuto da una piastra forata.

La procedura di calibrazione delle sonde WCR ha mirato a definire una legge per una stima accurata dei processi di infiltrazione nel suolo durante gli esperimenti di frana. Numerose prove sono state quindi condotte variando, rispettivamente, la porosità del provino di materiale posato nel contenitore; le caratteristiche del suolo erano costantemente monitorate da 3 tensiometri infissi e da altrettante sonde WCR. Il risultato finale ha restituito una legge di calibrazione dello strumento linearmente dipendente dal segnale di uscita della sonda WCR e anche dalla porosità del terreno.

Due esperimenti sul modello fisico di frana sono stati quindi realizzati su uno strato di materiale con due rispettive porosità. Il materiale impiegato consiste in una sabbia fine con distribuzione granulometrica molto uniforme. In un primo caso la sabbia è stata posata senza introdurre azioni di compattazione, a meno di una leggera battitura sulla superficie per evitare eccessive deformazioni successive alla precipitazione. In un secondo esperimento, la sabbia è stata invece posata e compattata per strati successivi, così da raggiungere uno stato addensato.

I due esperimenti sono stati rispettivamente eseguiti applicando un'intensità di precipitazione pari a 150 mm/h fino a collasso avvenuto. Le modalità di innesco osservate e l'analisi dei dati raccolti permettono di individuare gli elementi idrologici che determinano il collasso in entrambi i casi, mettendo anche in rilievo le diversità. Con sabbia sciolta, il collasso si verifica istantaneamente, senza segni premonitori che avvertano dell'imminente frana. All'innesco, il volume di terreno ha assunto le sembianze di un fluido ad alta viscosità, e i tensiometri installati registrano un picco istantaneo di pressione idraulica. Nel caso di sabbia addensata, il collasso avviene molto lentamente ed è preceduto da distacchi localizzati di strati sottili di terreno.

Un modello per la risoluzione dell'equazione di Richards è stato impiegato per riprodurre le dinamiche idrologiche che determinano l'innesco delle frane nei due casi distinti. Si è ricorso, inoltre, ad una procedura inversa per migliorare l'affidabilità della soluzione numerica rispetto ai dati sperimentali registrati durante le prove di frana. Il confronto esprime un'elevata corrispondenza tra dati numerici e sperimentali nel caso di sabbia sciolta. Nel secondo caso con sabbia addensata, le ipotesi del modello di Richards non sono sufficienti per raggiungere una corrispondenza accettabile con i dati sperimentali. Le cause possono ritrovarsi nell'influenza che la fase gassosa contenuta nei pori può determinare, nonché le deformazioni incipienti a micro-scala che si manifestano durante l'esperimento.

Parole chiave: Simulatore di pioggia, Distribuzione di diametri di gocce, Water Content Reflectometer, Innesco di frane superficiali, Porosità, Proprietà di ritenzione, Modellazione dell'equazione di Richards

Abstract

Shallow landslides studies are usually extended over landscape scale, where the investigations about geotechnical and hydrological properties of the soil are limited to some local points and not sufficient to assure an in-depth explanation of failure trigger. The physics of the phenomenon is thus minimized, and resolution in space and time is maximized. Such as approach can be useful to predict landslide occurrences for emergency purposes, but it is not effective to interpret the real triggering landslide mechanism.

A local scale analysis become needed to achieve an understanding of the processes leading to the failure. Specifically, a full comprehension requires to provide experimental data from a carefully monitored and controlled landslide field site.

The present study focuses on a large-scale device aimed at simulating shallow landslides triggered by heavy intensity rainfall. The physical model consists of an artificial hillslope built with a reinforced concrete box: the maximum height is 3.5 m, with length of 6 m and width of 2 m, so that a 2:3 slope can be built. On each lateral side of the box, 50 openings closed with screw caps allow the insertion on properly chosen positions of the control instrumentation (6 tensiometers and 6 Water Content Reflectometer sensors). The monitoring network, connected to an automatic acquisition system, was completed by two piezometers, and two stream gages able to evaluate both the surface runoff and subsurface contributions to the total outflow.

The work developed in this study concerns the design and the performance analysis of the main features characterizing the large-scale hillslope model, up to the performance of two landslide experiments on a 60 cm thick sandy soil layer.

A rainfall simulator was designed and built to reproduce an intensive precipitation causing the soil collapse. It was realized with a one-loop network equipped with spray nozzles appropriately chosen to minimize the surface splash erosion. In such a way the effects induced by the simulator concern infiltration dynamics without generating top erosion, which could introduce further factors of more difficult understanding. The nozzle configurations on the network were chosen to reproduce i) the desired range of the rainfall intensity, varying from 50 to 150 mm/h, and ii) the spatial uniformity of the produced rain.

A careful analysis of the rain sprayed by a single nozzle was developed on a prototype, in order to recognize the main variables affecting the nozzle functioning and performance. Further investigations were then carried out to test the performance of the final full-scale version of the rainfall simulator, highlighting its flexibility for the regulation and the control of the generated rain intensity. Depending on the desired rainfall range, four different configurations of nozzles, distinguished by the number of active nozzles and their location, were chosen to cover the required intensity interval.

A careful analysis about the drop diameters was conducted by recurring to an oil mixture poured in Petri dishes that were exposed to the rain. The drop size distribution thus collected characterizes the induced

rainfall and was used for a numerical simulation aimed at estimating the impact energy of the drops falling on the soil. The proposed model calculates the trajectories of the particles injected by the nozzle using a constitutive law of sphere aerodynamics in a 3D space. As a result, the rainfall potential erosion and its spatial distribution were assessed, highlighting the limited surface erosion generated by the proposed rainfall simulator.

In a second step, a suitable device was realized to calibrate the WCR (Water Content Reflectometer) sensors. It consists of a $0.6 \times 0.5 \times 0.6\ m^3$ Plexiglas box containing the soil with the top exposed to rainfall and the bottom sustained by a perforated base. The calibration of the WCR sensors pointed to obtain an effective law for an accurate assessment of the water infiltration evolution in the soil during the landslide experiments. Several tests were performed with varying porosity values of the sand sample placed into the Plexiglas box, where three tensiometers and as many as WCR probes were arranged. The final results suggest a calibration relationship linearly depending on the WCR output signal and porosity.

Two experiments on the artificial slope were then performed by applying two different porosities of the soil during the placement. The chosen soil consists of a fine sand with high particle size uniformity. The first porosity was obtained by dumping the sand without applying compacting action, such that the sand was in loose conditions. In a second case, the sand was compacted to yield a dense sand. The two experiments were carried out by applying the rainfall at $150\ mm/h$ until the sand collapse. The observation of the experiments and the analysis of the recorded data allow to examine the hydrological dynamics leading to the landslide and the triggering factors.

With loose sand, the failure occurred suddenly without warning signs; at the failure, the soil appeared like a viscous fluid and the tensiometers recorded an instantaneous peak of the water pressure head. In the case with dense sand, the failure occurred really slowly, and some local detachments of top layer preceded the advance of the whole sand volume.

A numerical model solving Richards equation was used to reproduce the hydrological processes leading to failure in the two experiments. A numerical inverse method was adopted to improve the reliability of the numerical solution with respect to the data recorded from the experiments. The comparison reveals a good agreement between the experimental and numerical results for the loose sand experiment. In the case regarding dense sand, the limits of Richards solution does not allow to reach an acceptable agreement with experimental recorded. The causes might be linked with the affection of the air phase in sand pores and the incipient deformation of the soil matrix at micro-scale.

Keywords: Rainfall simulator, Drop size distribution, Water Content Reflectometer, Landslide triggering, Porosity, Retention properties, Richards equation modeling

1 INTRODUCTION

1.1 PROBLEM STATEMENT

Rainfall may be the cause of multiple phenomena known as debris slides, debris torrent, debris floods, mudflows, mudslides, mudspates, and lahars (Varnes, 1978), which can be synthesized in the broad meaning attributed to debris flows (Iverson et al., 1997).

Although these phenomena can originate by various means, as pyroclastic soils having a loose structure, or melt snow (Pierson et al., 1990), or water that undermines and incorporates ample sediment, mobilization from shallow landslide predominates (Johnson, 1984).

Different styles of deformation help to discriminate the mobilized debris flows from landslides: debris flows exhibit pervasive, fluid-like deformation that facilities motion, whereas landslide motion is more rigid, with deformation localized along persistent slip surfaces or shear zone (Iverson et al., 1997). Therefore, landslide concerns a previous step with respect to debris flows, which is analogous to that between sand slipping incrementally along discrete failure surface and sand flowing rapidly. Landslide occurrence may completely or partially mobilize to form debris flows, and particular conditions must exists for mobilization to occur. Understanding these specific conditions is essential to produce a correct prediction of landslide and its consequences in steep hillslopes, where the failure emergency can happen during rainfall events.

Scientific efforts aiming at clarifying the landslide triggering mechanism and the spatial distribution of landslide susceptibility are significant and cover several decades of research. Initially, scientists focused on simplified or conceptual models of the hydrologic response of a basin to rainfall events, in order to provide topographic (wetness) indexes measuring the landslide potential.

Montgomery and Dietrich (1994), for instance, schematized the hydrologic response with a model that predicts the degree of soil saturation in response to a steady state rainfall for topographic elements defined by the intersection of contours and flow tube boundaries. More recently advancements have been made by more sophisticated hydraulic and soil mechanics models accounting for the transient evolution of the rain infiltration (Iverson, 2000; Chirico et al., 2000; Frattini et al., 2004; Morissey et al., 2008). Several subsequent hydrologic models have been inspired by this approach (Borga et al., 2002; Casadei et al., 2003;D'Odorico et al., 2005; Tarolli et al., 2012).

Because of their simplifying assumptions regarding the spatial variability of soil properties, the field soil characterization is often inaccurate and not sufficient for an adequate and in-depth understanding of rain-soil interactions preceding failure. Specifically, the lack of an adequate amount of information forces the landslides scientists to develop simplistic models simulating failure occurrences. These models are calibrated on real data taken from field sites, where the evolution of the process may be heavily different from modeling. An evident example concerns the role of the bedrock layer underlying the soil susceptible to failure: in most of real cases, the basement plays a significant role in the hydraulic interaction with the top soil, due to an appreciable

conductivity or to the presence of macropores. In the usual models, the hydraulic conductivity of the basement is not experimentally assessed, since it is considered not significant.

The result goes to interpret badly the real evolution of failure mechanisms with models that do not represent effectively the hydrological dynamics leading to collapse.

The hydrologic models are usually coupled with a slope stability method allowing a stability analysis related to a certain rainfall event. The most adopted approach uses the infinite slope assumption (Montogomery and Dietrich, 1994; Iverson, 2000; Borga et al., 2002; Morissey et al., 2008; Talebi et al., 2008; Tarolli et al., 2012; Lepore et al., 2013), wherein the failure surface is postulated parallel to the basement underlying the slipping mantle.

Therefore, the failure mechanism is predetermined, and it is analytically parameterized with a stability index commonly known as the safety factor. The calculation of the safety factor appears simple, but it implicitly introduces important assumptions based on the limit equilibrium analysis. The soil is regarded as a rigid solid subject to one-dimensional rupture due to exceeding the Coulomb shear strength. However, the versatility of this conceptual treatment makes the safety factor a convenient tool to be applied in many circumstances both for saturated and unsaturated soils.

Failure modes in reality cover a broader range of situations, intimately related to the soil water dynamics prior and during the process, limiting the applicability of the infinite slope stability analysis. The major limitation lies in the inability to describe the complete development of the pore water pressure at the failure initiation, which is needed to characterize the soil mobilization and the total volume involved.

Field observations and laboratory experiments (Anderson and Sitar, 1995; Iverson et al., 1997; Iverson et al., 2000; Iverson, 2005; Gabet and Mudd, 2006) indicate that landslide mobilization is triggered by two processes: 1) widespread Coulomb failure within a sloping soil and 2) partial or complete liquefaction of the mass by high pore-fluid pressures. This behavior mainly involves pyroclastic and colluvial soils, which have a loose structure. During the shear deformation the soil particles tend to rearrange and the soil contracts. When pore voids reach saturation or near-saturation, the soil particles collapse on the pores, provoking an abrupt pulse of water pressure and a partial or complete liquefaction of the soil mass.

Conversely, with well-compacted permeable soils, the mobilization is very different. The initial Coulomb failure determines the mutual slip of the interlocked soil grains and, as a result, the mass tends to dilate. The water pressure does not enhance the soil mobilization as in the previous case, typically exhibiting moderate fluctuations as the soil slips down slowly (Iverson et al., 1997; Iverson et al., 2000; Gabet and Mudd, 2006).

For all these reasons, models based on the safety factor, although useful, seem to be limited and there is a need for more detailed analyses of the infiltration physics responsible for triggering shallow landslides.

1.2 OBJECTIVES AND OBJECTS

The main objective of this research consists in developing a highly controlled and monitored large scale model to carry out landslide simulation. At this aim, we need to define carefully the components and the procedures that can affect the experimental performances and the reliability of the provided information; these parts consist of i) a rainfall simulator, the ii) monitoring instrumentation and the iii) design of the experiments. They are essential aspects of the present research, such that they require a specific and an individual development to be accomplished. In this way, we can reduce as more as possible strong uncertainties that are usually inherent in experimental investigations. For example, factors that may introduce inaccuracy are a bad assessment of the applied rain, and its spatial distribution, the calibration law of the probes, the soil characterization and its final set up in the large model.

The rainfall simulator is aimed at producing the main input causing the hydrologic evolution of the soil leading to the final collapse. Its assessment is then fundamental to hold the physical dynamics affecting the soil. Since we are treating heavy rainfalls, the intensity range we desire to cover goes from 50 to $150\ mm/h$. In order to encompass the rain heterogeneity as much as possible, an high spatial uniformity is desirable. Traditional literature suggests to achieve a minimal uniformity coefficient (see Section 2.2.1) equal at $80\ \%$, but, since the served surface is large (see Section 2.1), we prefer to consider the minimum at $85 - 90\ \%$.

Furthermore, our preliminary interest about landslide investigation is to analyze only the role of hydrological processes in landslide causing. The concurrent presence of other possible factors, as water splash erosion, could compromise an effective understanding of the hydrology role in leading the failure. This reflects on the rainfall characteristics, specifically on the drop kinetic energy at the impact with the soil, which requires a specific investigation to prove the water splash erosion to be negligible.

The monitoring probes provide empirical data that represent our basis to develop new highlights about landslides. The sensors installed in the soil acquire information about the hydrologic soil state, and they consist of tensiometer and WCR (Water Content Reflectometer) probes, which are employed to measure respectively the water pressure head and the volumetric water content inside the soil. The calibration procedure for the tensiometers is simply performed by directly relating the output signal with the water column loaded on the electric probe. About the WCR probes, the calibration procedure does not allow to relate the output signal with a direct measurement of the volumetric water content. A specific device containing a soil sample is needed to provide a calibration law for WCR.

The fulfillment of these objectives allows to achieve the purpose of simulating landslide experiments by means of the hillslope model (Figure 1-1). The experimental results permits to provide highlights about the a) hydrological processes leading to the failure initiation and causing the mobilization of a shallow sloping soil subject to heavy rainfall and b) to relate the soil properties to different landslide triggering modes.

Figure 1-1. The artificial hillslope model.

1.3 THESIS OUTLINE

The thesis outline reflects the work developed by sequential steps useful to define the final set up of the landslide model, in order to proceed to the experiments.

The topic that is firstly treated concerns the nozzle rainfall simulator (Section 2). Its characterization starts with the analysis of the performances of a single nozzle (see Section 2.2.1 and Section 2.3.1), and it proceeds with the design (see Section 2.2.2) and the experimental results about the rainfall simulator in its final arrangement (see Section 2.3.3). Moreover, the analysis of the drop size distribution (see Section 2.2.3 and Section 2.3.4) is exposed too. A numerical model (see Section 2.2.4) treating the sphere aerodynamics in a 3-D space is proposed: its use allows to define the falling trajectory of the sprayed drops to assess the spatial distribution and the intensity of the water splash erosion (see Section 2.3.6).

The second main topic deals with the calibration of the WCR probes (see Section 3). The calibration procedure is done by recurring to a laboratory facility (see Section 3.2.1), which permits the control the water content in a large scale sample. The final results provide a linear calibration curve (see Section 3.3) depending on the output signal and on the soil density.

The last topic (see Section 4) treats the final design of the landslide experiments (see Section 4.2.1), the soil characterization in terms of geotechnical properties (see Section 4.3.1) and of retention curves (see Section 4.3.2), and the results obtained from two tests at different soil porosity (see Section 4.3.3). A numerical software to solve the Richards equation is employed to compare numerical and experimental data (see Section 4.3.4): the consequent inferences (see Section 4.3.5 and Section 4.3.6) provide a detailed explanation of the observations.

The final conclusions (Section 5) report comments about the achieved objectives.

All the central sections (Section 2, 3 and 4) have the traditional structure of a scientific paper (i. e. introduction-material and methods-results-discussion) in order to provide a complete description of the elements tackled during the evolution of the research.

2 DESIGN AND PERFORMANCE ANALYSIS OF A NOZZLE RAINFALL SIMULATOR

2.1 INTRODUCTION

In the last decades, rainfall simulators (RSs) have represented a widespread tool for studying hydrologic interactions of rain water with soils (Tossell et al, 1987; Esteves et al., 2000; Abudi et al., 2012; Caracciolo et al., 2012). The main fields of investigation include soil erosion, overland flow generation, and infiltration; furthermore, their use is increasing for the improvement of the process knowledge about landslide occurrences as well as debris-flow events in equipped laboratory devices, aimed at reproducing the phenomena under carefully controlled conditions, either in small-scale or full-scale physical models (Reid et al.,1997; Iverson et al., 1997; Iverson, 1997; Rahardjo, 2002; Ochiai et al., 2004; Moriwaki et al., 2004; Reid et al., 2010; Reid et al., 2011).

RSs are usually classified in two types (Esteves et al. 2000): (i) dripformers, realized with hypodermic needles, and (ii) nozzle rainfall simulators. The choice is made on the basis of geometrical constraints, the portability, and the economic cost related to the RS type. The former is commonly employed for small plot areas, no larger than about $1 \div 2\ m^2$, whereas the latter is frequently used for larger areas (Meyer and McCune, 1958; Swanson, 1965; Niebling et al., 1981; Parsons et al., 1990; Riley and Hancock, 1997).

Considerable attention has also been paid to estimate the kinetic energy of the induced rainfall at the impact of the drops with the soil surface, especially for simulators designed to control erosion dynamics, runoff generation, and changes of the infiltration rate due to soil crusting (Kincaid et al, 1996; Esteves et al., 2000; Fox, 2004; Pérez-Latorre, 2010; Abudi et al., 2012; Caracciolo et al., 2012). The features needed to assess these aspects are linked with both the sizes of the sprayed drops and the terminal velocity at the impact, these two terms controlling the kinetic energy of the falling drops.

Several different procedures have been proposed in the past to this aim: one of the most widespread methods consists in collecting the raindrops in a layer of flour contained in a shallow can (Kincaid et al., 1996); other techniques employ the stain method or the photographic method. Most of these methods require an extensive calibration before use and provide limited information on the rain drop size distribution (DSD). More recently, other devices have been developed to analyze the DSDs by using technologies such as the laser disdrometer and high-speed video cameras. Despite the good accuracy of these cutting-edge instruments, only local observations have been made on the potential soil erosion generated by rainfall simulators, without considering the spatial distribution in the plot area, unavoidably related to the spatial distribution of the generated rainfall.

In the present study, an experimental procedure is proposed to design a rainfall simulator for a full-scale artificial slope with horizontal plot area of $6\ m \times 2\ m = 12\ m^2$, used to simulate infiltration processes and surface landslide triggering due to heavy rainfall. The desired properties of the simulator consist in producing i) a wide range of rainfall intensity, varying from 50 to $150\ mm/h$, ii) a high spatial uniformity of the rain on the

plot area and iii) a limited soil erosion due to the drop impact. This last aspect was required to focus only on the role of infiltration, which affects the water pressure evolution in shallow soil layers causing rapid landslides. A rainfall simulator equipped with nozzles installed on a one-loop pipe network was chosen to achieve an adequate adjustment over the artificial slope. An optimal distribution of the nozzles was reached after a careful analysis for assessing the spray properties of a single functioning nozzle, with respect to both a horizontal and an inclined set-up. In this preliminary analysis, the main properties investigated were the time steadiness of the rain, guaranteed by the municipal water supply network, and the spatial uniformity on the irrigated surface. The drop size distribution generated by a single nozzle was then assessed by adopting the oil method, which makes use of a viscous oil within Petri dishes to capture the raindrops (Eigel and Moore, 1983). The results of the analysis, in terms of drop size distribution, were then used in a numerical model able to describe the falling trajectory of the drops. The method allows the estimation of the maximum potential erosion as well as its spatial distribution.

2.2 MATERIAL AND METHODS

The design of the rainfall simulator (RS) was developed based on our specific requirements. Hignett et al. (1995) listed a series of advisable features: (a) accurate reproduction of natural rainfall drop sizes and energy at the landing point; (b) spatial uniformity for plot areas of $1\ m^2$ or larger; (c) capability of reproducing rainfall of varying durations and intensities; (d) portability and low cost. In our case, recurring to nozzles (Figure 2-1) was undoubtedly preferable due to the technical constraints related to the slope structure: the rainfall simulator was intended to be applied on an full-scale slope, contained in a reinforced concrete box with internal length of $6\ m$ and internal width of $2\ m$, such that a $3{:}\,2$ slope can be obtained (Figure 2-2). This structure was used to reproduce landslide triggering under monitored hydrological dynamics induced by heavy rainfall. Multiple variables are involved in the process and they can interact with each other resulting in an increased slope instability. At this stage, we want to consider only the contribution due to infiltration forces, neglecting the soil surface erosion caused by the impact of the raindrops on the soil surface. In this way, we can study the importance and the magnitude of the water potential contribution in controlled conditions, without the disturbance of other concurring processes. Therefore, the nozzles were chosen to reduce the size of the drops, avoiding (or minimizing) soil erosion. We adopted HH square jet nozzles from Spraying System (Esteves et al., 2000; Pérez-Latorre,2010; Abudi et al., 2012) with capacity sizes of 14 WSQ, 20 WSQ, and 30 WSQ respectively, where WSQ (Wide SQuare) identifies nozzle with square spray angle.

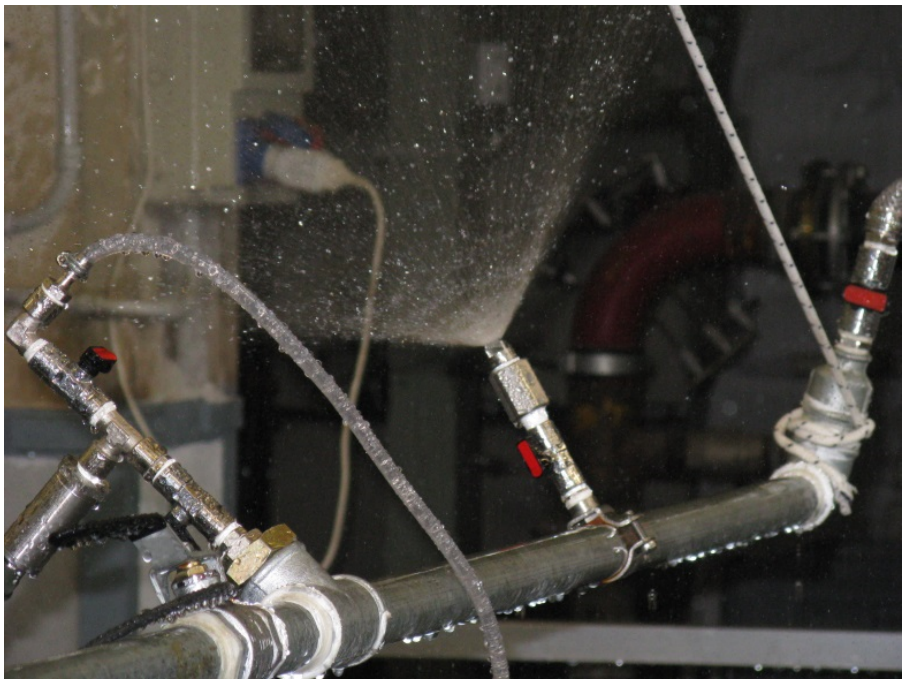

Figure 2-1. A spray nozzle during experimental test to assess its performances.

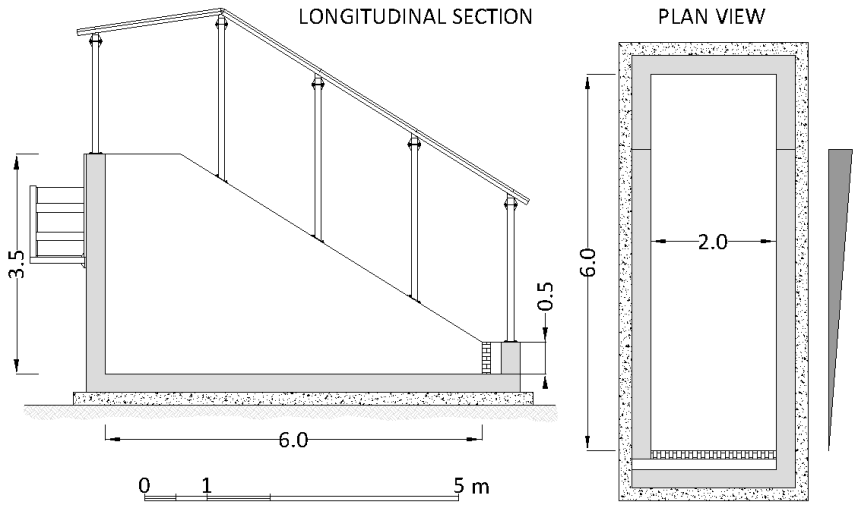

Figure 2-2. Longitudinal section and plan view of the large-scale artificial slope

2.2.1 Single nozzle performance

The functioning of the nozzles was analyzed with a laboratory device (Figure 2-3) that permitted the monitoring and control of the operating water pressure and spray discharge. The discharge and the corresponding pressure values were measured with an electromagnetic flow meter and a pressure transducer, respectively, located at suitable distances from the valves, which can induce disturbances of the flow paths and compromise the measurements. All data were recorded and collected with a data acquisition system from Campbell Scientific (DAQ model), with an acquisition frequency of 100 Hz.

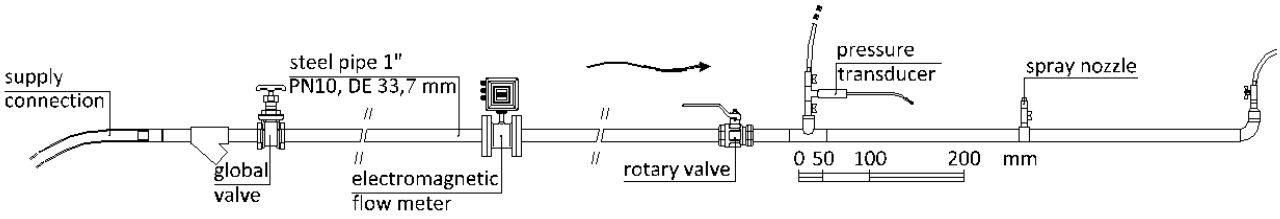

Figure 2-3. Sketch of the experimental device used to test the single nozzle performance.

The first performance tests on the nozzles consisted in spraying water on a surface with area 2 m × 2 m = 4 m^2, on which 41 rain gauges, with height of 120 mm and diameter of 87.2 mm, were distributed (Figure 2-4). The gauges were weighed after a 20-minute rain event, providing the average intensity and the spatial uniformity on the surface, computed via the uniformity coefficient defined by Christiansen (1942):

$$CU = 100\left(1 - \frac{\sum_{i=1}^{n}|X_i - \bar{X}|}{n \cdot \bar{X}}\right),$$

where X_i represents the local value of rainfall intensity, $\bar{X}$ the spatial average and n the total number of data. These preliminary tests were performed to obtain the optimal position of the nozzles with respect to the irrigated area, the best pressure range, and the elevation above the surface that keep the uniformity coefficient within acceptable limits. The nozzle was initially positioned over the center of the surface (Figure 2-4) and

pointing downwards; an additional position, on the edge and pointing upwards (Figure 2-4) is subsequently tested.

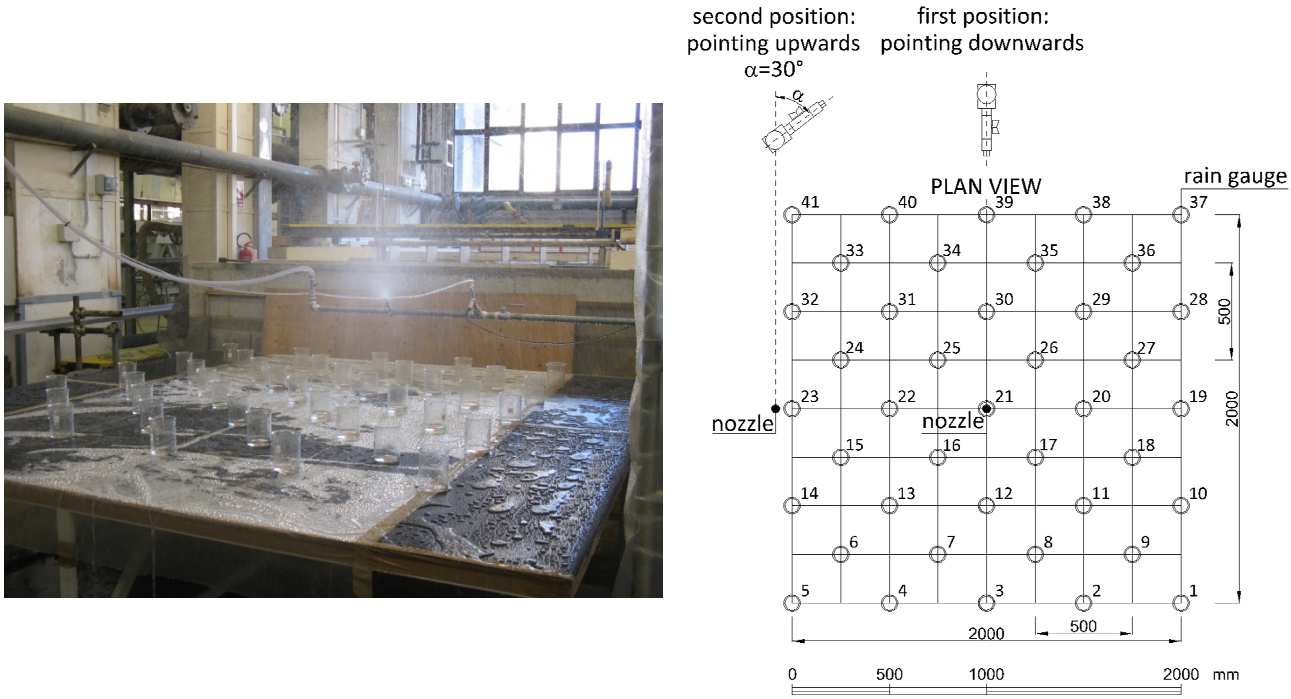

Figure 2-4. An image (on the left) of the experimental test for measuring the rainfall intensity and the spatial distribution generated by a single nozzle and (on the right) a sketch of the plot area with the location of the rain gauges and two alternative vertical positions of the nozzle.

Three tests were carried out for each nozzle (14, 20, and 30 WSQ) with varying pressures, using the same elevation of 0.4 m above the surface and an angle of 30° of the nozzle axis with respect to the vertical direction. For the nozzle WSQ 30, more tests were performed to confirm the relation law of pressure with the induced rain intensity, which was then extended to the other nozzle types. In the subsequent tests, the elevation above the surface was varied while maintaining constant pressure values (1 bar and 1.5 bar). The data collected provided useful relationships for predicting the nozzle operating conditions once installed on the rainfall simulator and the variations produced by changing the pressure and the elevation above the irrigated area.

The same experiments were then repeated over a sloping geometry. The irrigated surface consisted of 5 cm-thick polystyrene sheets (Figure 2-5) arranged to form a ladder with an overall slope of 32°, the same as the artificial hillslope (Figure 2-2). The steel pipe, where the nozzle was mounted, was positioned parallel to the slope and the rain gauges were located on the steps. These additional tests led to a direct comparison between the rain characteristics in the horizontal and the inclined set-up.

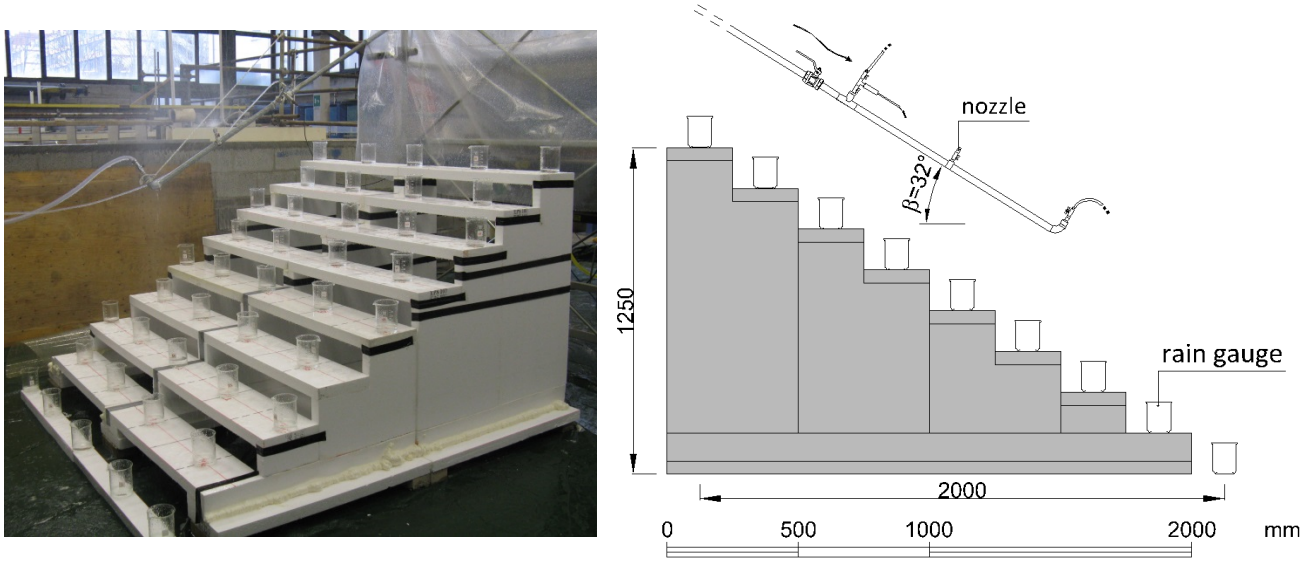

Figure 2-5. An image (on the left) and a cross- section (on the left) of the laboratory device used for measuring the rainfall characteristics on an inclined surface.

2.2.2 Rainfall simulator

The artificial rainfall was produced by the nozzles fixed on a looped network of pipes that follows the perimeter of the concrete box (Figure 2-6). The design of the rainfall simulator is constrained by the structure geometry, i.e., the wall and the roof, while valves and adequate sensors to regulate and to manage the rainfall complete the facility. The objective was to produce rainfall intensities ranging from $50\ mm/h$ to $150\ mm/h$ and with uniformity coefficient (CU) values larger than $80 - 90\ \%$ (Neff, 1979; Esteves et al., 2000).

The one-loop pipe network was designed to accommodate a maximum of 18 nozzles, fixed along the pipe and pointing upwards with an inclination equal to 30° (Figure 2-6); the distances between the nozzles are equal to $0.5 - 1\ m$. The pipe diameter is $2.54\ cm$, to minimize energy losses, which can be considered negligible for the assumed flow range. A globe valve for the discharge regulation, an electromagnetic flow meter, a rotary valve, and a vent pipe were located upstream from the loop, distributed all along a vertical pipe (Figure 2-6). The valves were kept at a distance from the flow meter equal to 10 times the pipe diameter, to prevent possible noises in the flow measurements. In the loop, 4 pressure transducers and 2 globe valves were installed, together with a blow-off valve that allows us to empty the network, if needed.

The maximum pressure of the network, measured with the nozzles shut off, results from the municipal water supply and is roughly $2.4\ bar$. When the nozzles are active, energy losses upstream from the network increase and the water pressure reaches a still acceptable value of $1 - 1.2\ bar$, for a total discharge of $45\ l/min$. The distinctive geometry of the loop, with a slope equal to that of the soil surface in the artificial hillslope, causes the nozzles to work at different pressures, with upstream nozzles operating at lower pressures compared to downstream nozzles. It was roughly estimated that the downstream nozzles release a

discharge 17 % larger than the upstream nozzle discharge for pressure values falling within 0.75 and 1 bar, and 10 % greater for higher pressures. These differences are compensated by combining adequately the active nozzles along the network, in order to produce a uniform rain.

The rainfall amount is controlled by means of: (i) the regulation of the globe valve, installed upstream from the pipe loop; (ii) the elevation of the loop above the irrigated area, variable thanks to a shifting support system; (iii) the number and the set-up of active nozzles. Therefore, the rainfall properties were evaluated by varying these specific attributes for four different nozzle set-ups, characterized by different numbers and positions of the active nozzles. Several tests were carried out by keeping a steady pressure for events lasting 15 to 20 min. The rainfall intensity was measured with 48 rain gauges positioned at the same elevation of the presumed soil surface and arranged in a vertical position (Figure 2-6). The distance between the rain gauges was 0.5 m: in order to verify the reliability of the rainfall distribution measured over the irrigated area, some tests ware repeated twice with 96 (spacing of 0.25 m distances) and 48 rain gauges (spacing of 0.5 m distances), respectively, checking that no appreciable differences occurred in the final measurements.

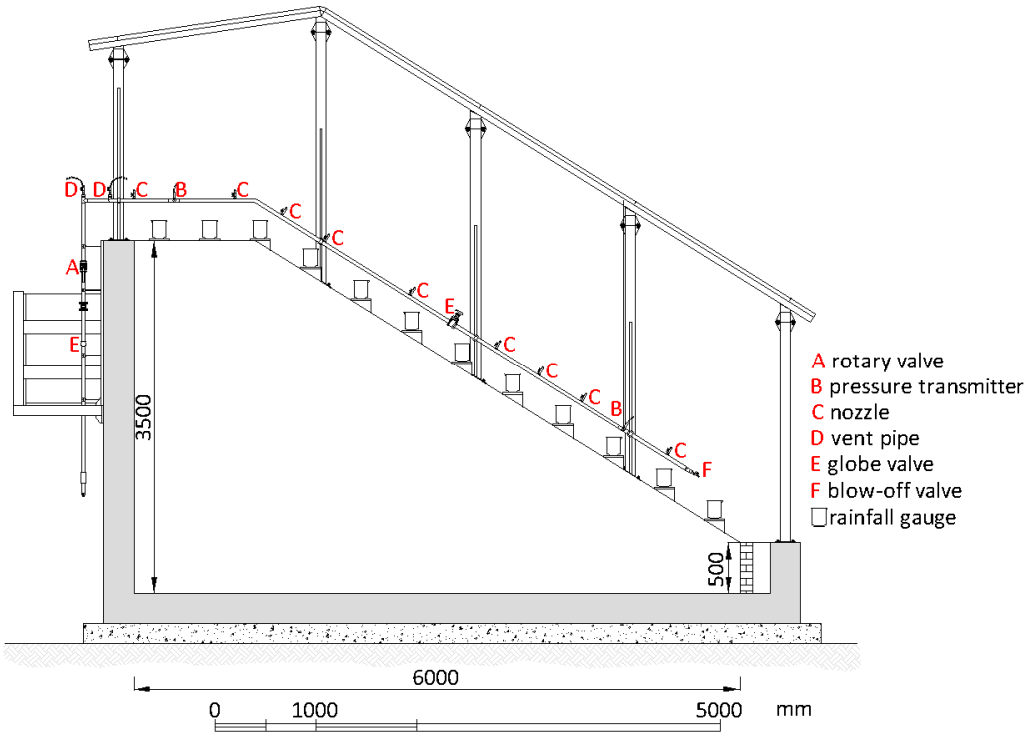

Figure 2-6. Longitudinal section of the pipe network installed on the artificial hillslope.

2.2.3 Drop size distribution

To carefully evaluate the potential erosion that could be generated at the soil surface, the drop size distribution of the sprayed rain was assessed. After pouring an oily mixture obtained with STP oil (motor oil with kinematic viscosity varying from $\nu = 5.6 \times 10^{-6}\ m^2/s$, in winter, equal to $12.5 \div 16.3 \times 10^{-6}\ m^2/s$ at 100°C,

density ρ = 893 kg/m^3), and mineral oil (density ρ = 0.862 kg/m^3 at 25° and viscosity $\nu = 63 \div 60 \times 10^{-6}$ m^2/s at 40 °C) into petri dishes, an experiment was performed by positioning 20 dishes at 0.5 m space intervals on a square surface of 2 m × 2 m (Figure 2-7). The nozzle sprayed for 3 s and an image of each petri dish was obtained with a high resolution scan (1200 dpi). All the images were subsequently processed with a MATLAB script based on the Hough Transform algorithm (Ballard, 1981; Ioannou, 1999), to obtain number and diameters of the drops. The Hough Transform is a method for detecting curves by exploiting the duality between points on a curve and parameters of that curve; in this case, the technique makes use of the property that every chord of a circle passes through its center. The analysis was conducted assuming that the raindrops are perfectly spherical (Cruvinel et al., 1999).

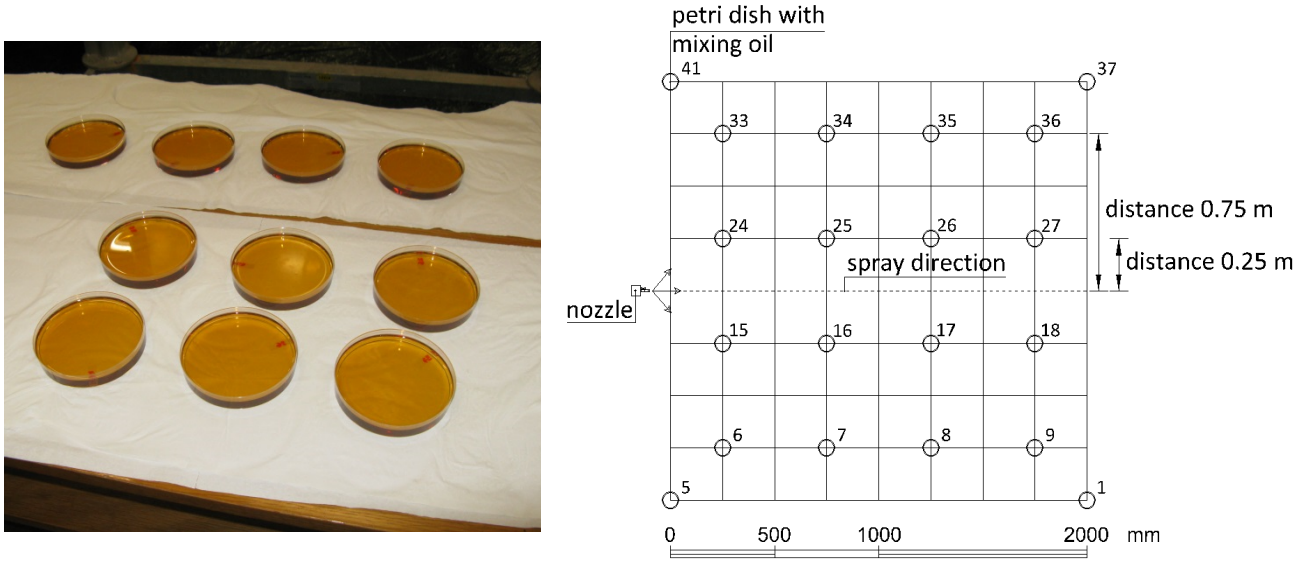

Figure 2-7. The Petri dishes (on the left) with the viscous soil and their location (on the right) for measuring the drop size distribution.

2.2.4 Numerical model for the simulation of the spray nozzle

A numerical model was developed in MATLAB to reproduce the falling trajectory of raindrops sprayed by the nozzles. The model allowed us to assess, although approximately, the kinetic energy at the impact on the irrigated surface, relating the different raindrop sizes to the falling velocity estimated by the numerical model. Such information eventually lead to the evaluation of the potential erosion induced by the rain. The modeled variable is the velocity of the raindrop at the impact with the soil surface. In natural rains, drops reach a constant terminal velocity before touching the soil, due to the equilibrium between the drag and gravity forces, whereas for the rainfall simulator, because of the position and elevation of the nozzles with respect to the surface, this constant value is never reached. The terminal velocity depends on the initial spray direction and velocity.

The constitutive law adopted in the model is derived by means of a Lagrangian approach, already used in the past to describe successfully water drop dynamics (Pérez-Latorre et al., 2010; Crosfield et al., 2009).

The following hypothesis are assumed: the injection velocity is the same for all the particles belonging to the considered drop sample; the particle diameter does not change during the trajectory; the trajectory is calculated assuming an isolated droplet, i.e., droplets do not interact with each other (Crosfield et al., 2009); air velocity is zero; the resistance law is taken from Haider and Lievenspiel, 1989.

Under these assumptions, the floating effect of the drops due to the air immersion is neglected, and the momentum equation for a water particle becomes:

$$\frac{d\bar{u}}{dt} = -\bar{g} - \overline{\overline{F_D}}\bar{u}, \qquad \textbf{(1)}$$

where $\bar{u}$ is the velocity vector of the water particle, $\bar{g}$ is the acceleration due to gravity, $\overline{\overline{F_D}}$ is the drag tensor, which defines the drag force for a unit mass particle, and t is time. The drag force is expressed as (Pérez-Latorre, 2010):

$$F_D = \frac{18}{24}\frac{C_D Re}{\rho D^2}\mu,$$

where $\rho = 1000\,\frac{\mathrm{kg}}{\mathrm{m}^3}$ is the water density, $\mu = 176.6 \times 10^{-7}\,\frac{\mathrm{kg}}{\mathrm{m{\cdot}s}}$ is the air viscosity, D is the diameter of the particle, assumed spherical, $Re = \frac{\rho_a D|u|}{\mu}$ is the Reynold's number, $\rho_a = 1.20806\,\frac{\mathrm{kg}}{\mathrm{m}^3}$ being the air density, and C_D is the drag coefficient. The latter can be expressed as (Haider and Levenspiel, 1989; Pérez-Latorre, 2010)

$$C_D = \frac{24}{Re}(1 + b_1 Re^{b_2}) + \frac{b_3 Re}{b_4 + Re},$$

where:

$b_1 = \exp(2.3288 - 6.4581\varphi + 2.4486\varphi^2)$;

$b_2 = 0.0964 + 0.5565$;

$b_3 = \exp(4.905 - 13.8944\varphi + 18.4222\varphi^2 - 10.2599\varphi^3)$;

$b_4 = \exp(1.4681 + 12.2584\varphi - 20.7322\varphi^2 + 15.8855\varphi^3)$;

$\varphi = \frac{s}{S}$ being the shape factor, with s being the surface of the sphere having the same volume as the drop and S the surface of the drop.

In a three-dimensional space, the momentum equation is projected on the axes of a Cartesian coordinate system: the particle velocity, for example, is expressed as the vector sum of the three components along the axes:

$$\bar{u} = u_x\bar{\imath_x} + u_y\bar{\imath_y} + u_z\bar{\imath_z},$$

where

$$u_x = \bar{u} \cdot \bar{\imath_x} = u \cdot cos(\alpha_x)$$

$u_y = \bar{u} \cdot \bar{\imath_y} = u \cdot cos(\alpha_y)$

$u_z = \bar{u} \cdot \bar{\imath_z} = u \cdot cos(\alpha_z)$

are the velocity components along the three directions with versors $\bar{\imath_k}$, and $\propto_k$ represents the angle between the velocity vector and the kth axis. Applying the vector decomposition, the momentum conservation (1) leads to:

$$\begin{pmatrix} \frac{du_x}{dt} \\ \frac{du_y}{dt} \\ \frac{du_z}{dt} \end{pmatrix} = -g \begin{pmatrix} 0 \\ 1 \\ 0 \end{pmatrix} - \begin{pmatrix} \frac{18}{24}\frac{C_D\mu}{D^2\rho}Re_x & 0 & 0 \\ 0 & \frac{18}{24}\frac{C_D\mu}{D^2\rho}Re_y & 0 \\ 0 & 0 & \frac{18}{24}\frac{C_D\mu}{D^2\rho}Re_z \end{pmatrix} \cdot \begin{pmatrix} u_x \\ u_y \\ u_z \end{pmatrix},$$

where the tensor $\overline{\overline{F_D}}$ is represented as a diagonal matrix, assuming that the axes coincide with the principle directions and $Re_k = \frac{\rho_a D|u_k|}{\mu}$ is the Reynold's number corresponding to the k-th components of the velocity.

The numerical model computes the raindrop trajectory using a finite difference approximation, which, for the vertical direction, leads to:

$$Re_z(t) = \frac{\rho_a D|u_z(t)|}{\mu}$$

$$C_{D_z}(t) = \frac{24}{Re_z(t)}(1 + b_1 Re_z(t)^{b_2}) + \frac{b_3 Re_z(t)}{b_4 + Re_z(t)}$$

$$F_{D_z}(t) = \frac{18}{24}\frac{C_{D_z}(t)Re_z(t)}{\rho D^2}\mu$$

$$u_z(t + \Delta t) = u_z(t) - \Delta t\left(g + F_{D_z}(t)u_z(t)\right)$$

$$z(t + \Delta t) = z(t) - \Delta t\frac{(u_z(t+\Delta t)+u_z(t))}{2}.$$

The initial position of the particles is given by the nozzle location, which represents the injection point of all the raindrops:

$x(0) = x_{start}$

$y(0) = y_{start}$

$z(0) = z_{start}$,

while the initial condition for the spray velocity is $\bar{u}(0) = \bar{u}_{start}$. The model takes into account the following geometric variables (Figure 2-8): $\propto$, the angle between the vertical axis and the nozzle axis; θ, the sloping angle of the network where the nozzle is installed; γ, the sloping angle of the plot area; and β, the spray angle, assumed equal to 100° as suggested by the manufacturer.

After defining all the geometric variables of the problem, the velocity and the directions of the drops at the injection point were established. The initial directions should cover the entire amplitude of the spray cone, which, as indicated by the manufacturer, is considered square-shaped. The injection cone is equally

subdivided into $n_p{}^2$ directions, where n_p is defined by the user and allows the drops to be sprayed from different orientations (Figure 2-8).

Considering a drop diameter sample with a sufficient size, a simulation can be made by associating the chosen sample to each of the $n_p{}^2$ starting directions: by running the model, the calculation of each single trajectory allows us to know the position of the drops and their velocity at the impact with the soil surface.

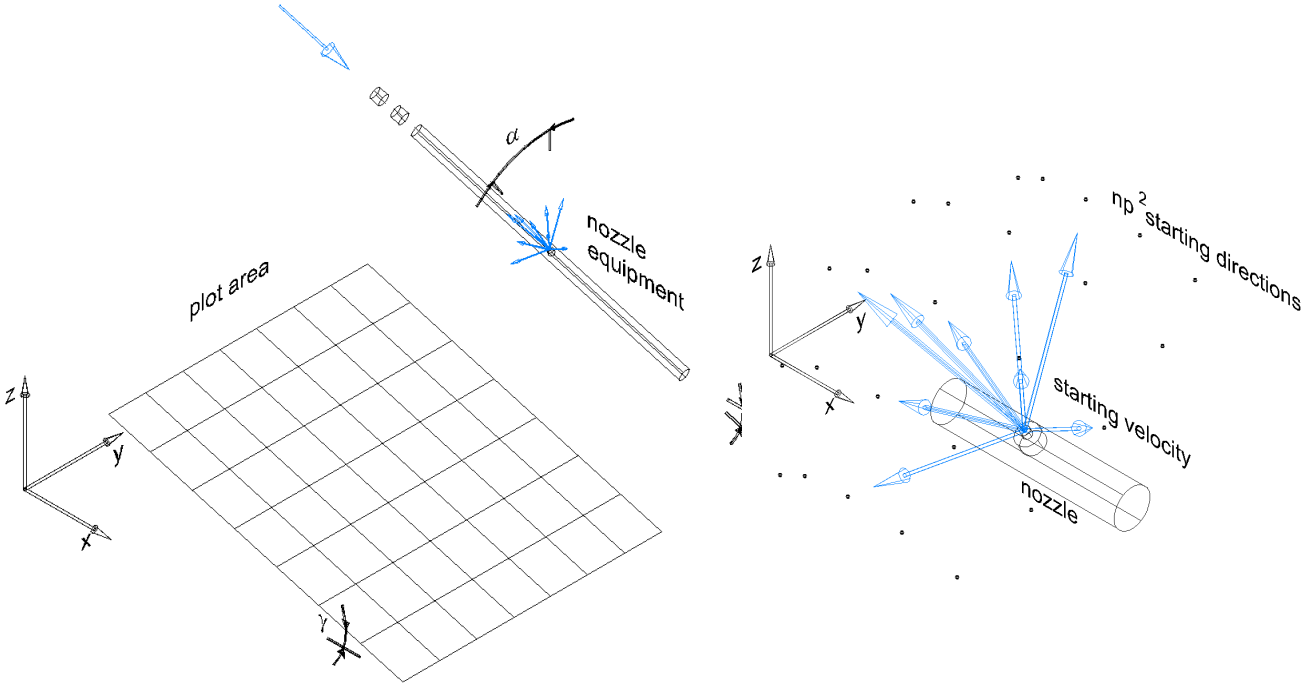

Figure 2-8. Numerical model: on the left the geometric variables accounted for reproducing the falling path of raindrops; on the right a sketch of velocity vectors imposed to the raindrop sample at the injection point.

The employed diameter sample is obtained from the experimental analysis conducted with the oil method, and the spray velocity is derived from a calibration of the model with respect to the spatial distribution of the drop diameters, again derived from the drop size distribution analysis. To this aim, the surface where drops are assumed to fall is divided in a discrete number of cells (Figure 2-8), and for each of them the relative frequency $f_i = \frac{{n_i}^p}{N_p}$ is obtained for specific drop diameters, where ${n_i}^p$ represents the number of particles with a certain diameter D_i fallen onto the p-th cell and N_p is the total number of drop particles fallen in the same cells. A similar analysis was carried out for the data inferred from the petri dishes: the comparison between the numerical and the experimental data, allows the calibration of the spray velocity at the injection point.

2.3 RESULTS

2.3.1 Performance of a single nozzle

The tests carried out to find the optimal position of the nozzle that maximizes the rainfall spatial uniformity reveal that the nozzle positioned on the side of the irrigated area and pointing upwards is the best configuration, as previously found by Pérez-Latorre et al. (2010) and Esteves et al. (2000). The uniformity coefficient for the nozzle pointing upwards, with an angle equal to 30° with respect to the vertical direction, is twice than that of the nozzle laying in the middle (~60 % vs ~30 %, respectively). A significant decrease in average rainfall intensity is found between the two configurations, due to the different working pressure and, mainly, to the jet orientation: in the first case, the whole jet is pointed downwards and no water is dispersed out of the irrigated area, whereas in the second case the wetted area becomes larger than the reference plot ($2\ m \times 2\ m = 4\ m^2$) and the effective rainfall changes drastically.

Once the position of the nozzle was fixed at the side of the irrigated area, further tests were carried out varying both the pressure and the elevation of the nozzle, to find operating conditions that yield satisfying characteristics of the produced rain. The results are shown from Figure 2-9 to Figure 2-12. In Figure 2-9, the proportional relation between the average intensity and the functioning pressure is evident. Figure 2-10 reveals the acceptable working pressure for high uniformity coefficients, where pressure values lower than 1 bar result in unsatisfying uniformity, whereas for pressure values greater than 1 bar, the uniformity coefficient seems to be approximately steady.

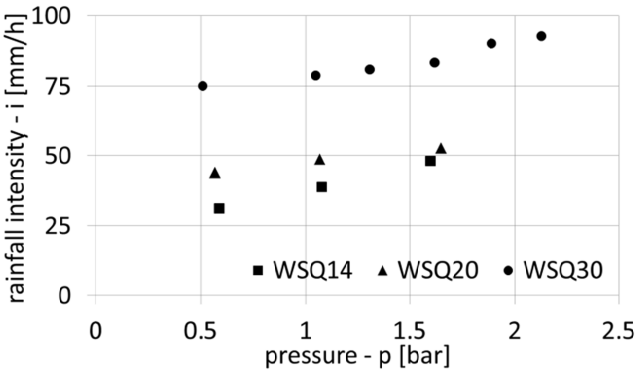

Figure 2-9. Average rainfall intensity at varying working pressures.

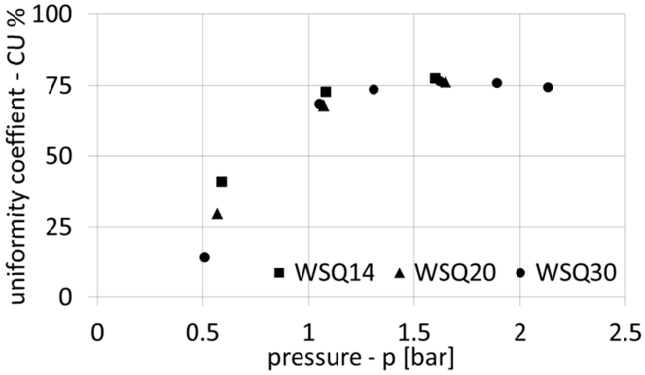

Figure 2-10. Uniformity coefficient at varying working pressures.

Several tests were conducted with the nozzle WSQ 14, changing the elevation and with two values of the pressure. The results in Figure 2-11 highlight that the average intensity and the nozzle elevation are inversely related, while no recognizable functional relation appears with the uniformity coefficient (Figure 2-12). The nozzle elevation ranges from 0.4 m to 1 m, with a uniformity coefficient that is always above 70 %, which can be considered acceptable for a small area sprayed by a single nozzle.

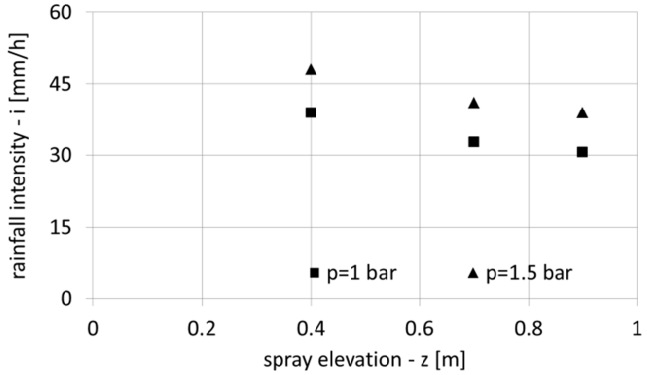

Figure 2-11. Average rainfall intensity at varying elevations above the irrigated area.

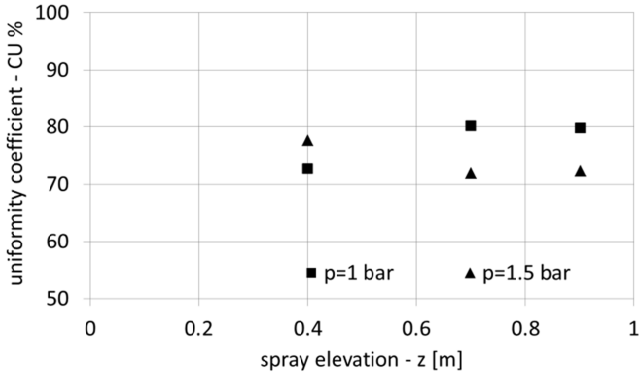

Figure 2-12. Uniformity coefficient at varying elevations above the irrigated area.

2.3.2 Comparison between a single nozzle over a horizontal and inclined irrigated area

Table 2-1 reports data from the experiments conducted with the same operating conditions previously described, but for different geometries of the irrigated area: horizontal and inclined (Figure 2-5). The comparison between the two data series highlight the effect of the sloping geometry on the distribution of the produced rain. The uniformity coefficient is slightly decreased in the sloping surface, accompanied by a significant increase of the average intensity between 28% and 49%. The results can be directly visualized in Figure 2-13, which shows the rainfall distributions in the different experiments. On the inclined surface, the rainfall intensity tends to concentrate around the maximum value, justifying the decrease in uniformity. Furthermore, the maximum intensity detected in the sloping surface is much larger than for the horizontal surface, roughly twice as much, despite the intensity measured near the boundaries being very similar. This is due to the different trajectories of the drops compared to the horizontal geometry: the sloping angle of the pipe on which the nozzle is installed causes the accumulation of water close to the projection of the nozzle on the irrigated area.

Table 2-1. Results from the experiments with the nozzle spraying on a horizontal and inclined surface.

nozzle	z [m]	α [°]	surface position	p [bar]	Q [l/min]	i [mm/h]	σ [mm/h]	CU %	CV
WSQ14	0.40	30.00	INCLINED (β=32°)	1.5	7.19	61.63	28.62	68.5	0.46
			HORIZONTAL		6.90	48.11	14.58	77.54	0.3
WSQ14	0.70	30.00	INCLINED (β=32°)	1.0	5.89	41.93	15.04	75	0.36
			HORIZONTAL		5.59	32.74	8.59	80.13	0.26
WSQ20	0.40	30.00	INCLINED (β=32°)	1.5	9.33	78.62	27.67	71.46	0.35
			HORIZONTAL		9.17	52.64	15.78	76.24	0.3

z: elevation of the nozzle; α: angle between the nozzle axis and the vertical direction; p: pressure; Q: sprayed discharge; i: average rainfall intensity; σ: standard deviation of local intensity measurements; CU: uniformity coefficient of the rainfall intensity; CV: coefficient of variation of the rainfall intensity: i/σ

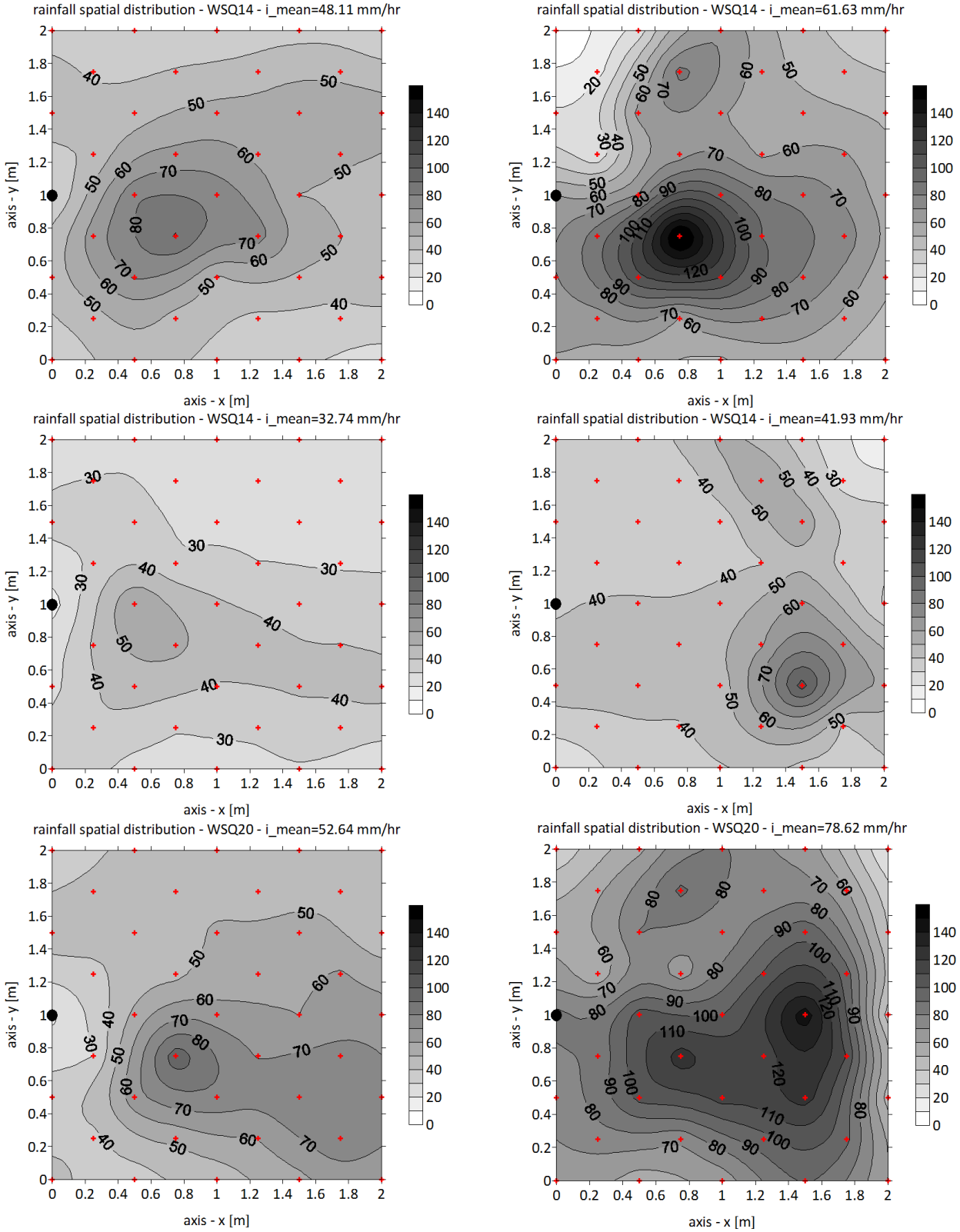

Figure 2-13. Rainfall distributions obtained from experiments with a single nozzle on a horizontal (left images) and on an inclined surface (right images). Pressure and nozzle elevation are the same for each couple of images: (top) p=1.5 bar and z=0.4 m with nozzle WSQ 14; (middle) p=1 bar and z=0.7 m with nozzle WSQ 14; (bottom) p=1.5 bar, z=0.4 m with nozzle WSQ 20. The black dots indicate the nozzle position, while the red crosses indicate the position of the rain gauges for measuring the rainfall rate.

2.3.3 Rainfall simulator

The results from the tests on a single nozzle highlight the main factors, and their relevance, affecting the uniformity and the intensity of the produced rainfall, i.e., the elevation of the nozzle above the surface and the operating pressure. Therefore, it is expected that they represent the controlling components also for the rainfall produced by the looped pipe network. We expect relevant improvements in the uniformity coefficient, compared to the values collected for the single nozzle, thanks to the overlap of the jets from different nozzles located close to each other.

Four configurations of nozzles, with different numbers and positions of active nozzles on the network (Figure 2-14), are chosen among possible others for their high uniformity performance. These configurations are denoted with 3_1, 7_2 and 5_3 (Figure 2-15), where the first digit indicates the number of operating nozzles. The 5_3 configuration works with WSQ 20 nozzles, while the 7_2 works with WSQ 14 nozzles. The 3_1 is tested with both nozzle types. The rainfall intensity resulting from the experiments as a function of operating pressure and nozzle elevation is shown in Figure 2-16 (graphs on the left): the proportional relation between average rainfall intensity and pressure is similar to the one found for the previous tests with a single nozzle, as well as the inverse relation with the nozzle elevation. For the 3_1 configurations, with both nozzle types, the rainfall intensity at different nozzle elevations does not change appreciably, because the area sprayed by only three active nozzles does not change by increasing the elevation above the surface. This is mainly due to the low number of active nozzles with respect to the wide area (12 m^2).

Figure 2-14. An image of the (on the left) rainfall simulator installed on the artificial hillslope, and (on the right) during an experimental test for measuring the rain intensity.

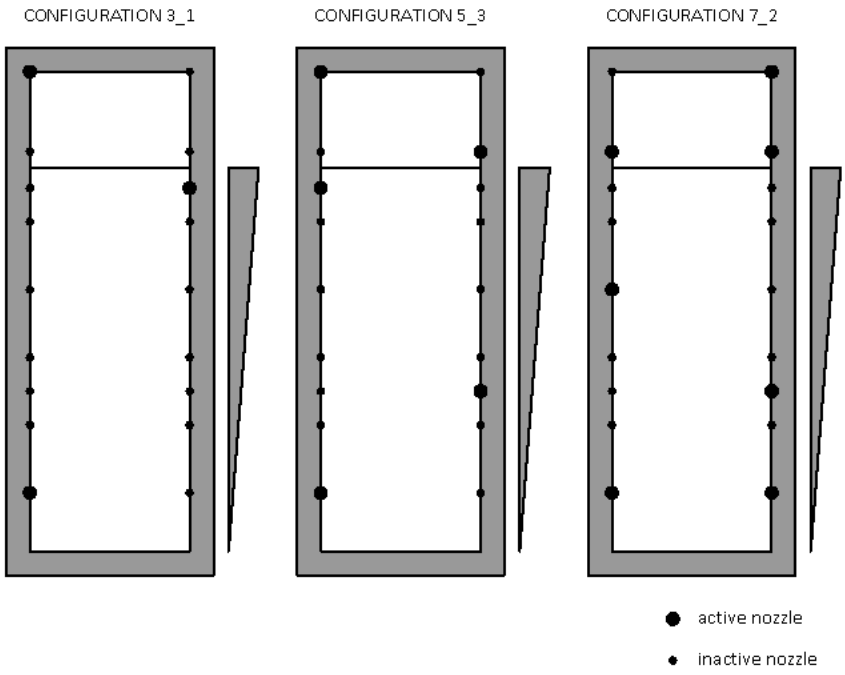

Figure 2-15. Different configurations of active nozzles in the rainfall simulator.

The results also show that the whole range of desired rainfall intensity (between 50 mm/h and 150 mm/h) is reproduced with the chosen configurations: the 3_1 configuration produces the low intensities from 50 to 100 mm/h, while the others allow us to reach the larger intensities up to 150 mm/h.

The graphs on the right panels of Figure 2-16 show the uniformity coefficient resulting from each experiment: for the majority of the tests, the values are larger than 80 %. The data with uniformity coefficient smaller than 80 % derive from working pressures lower than 1 bar, according to the results previously shown with only one nozzle (Figure 2-10). The best performances, in terms of uniformity, are obtained with the highest values of pressure and nozzle elevation; in particular (Figure 2-16, panels f and h), for small spray elevations, i.e., around 0.4 and 0.65 m, the uniformity coefficient is sensibly affected by the pressure, whereas for the highest elevations, around 0.90 m, the uniformity coefficient maintains higher values without appreciable variations due to changing pressures.

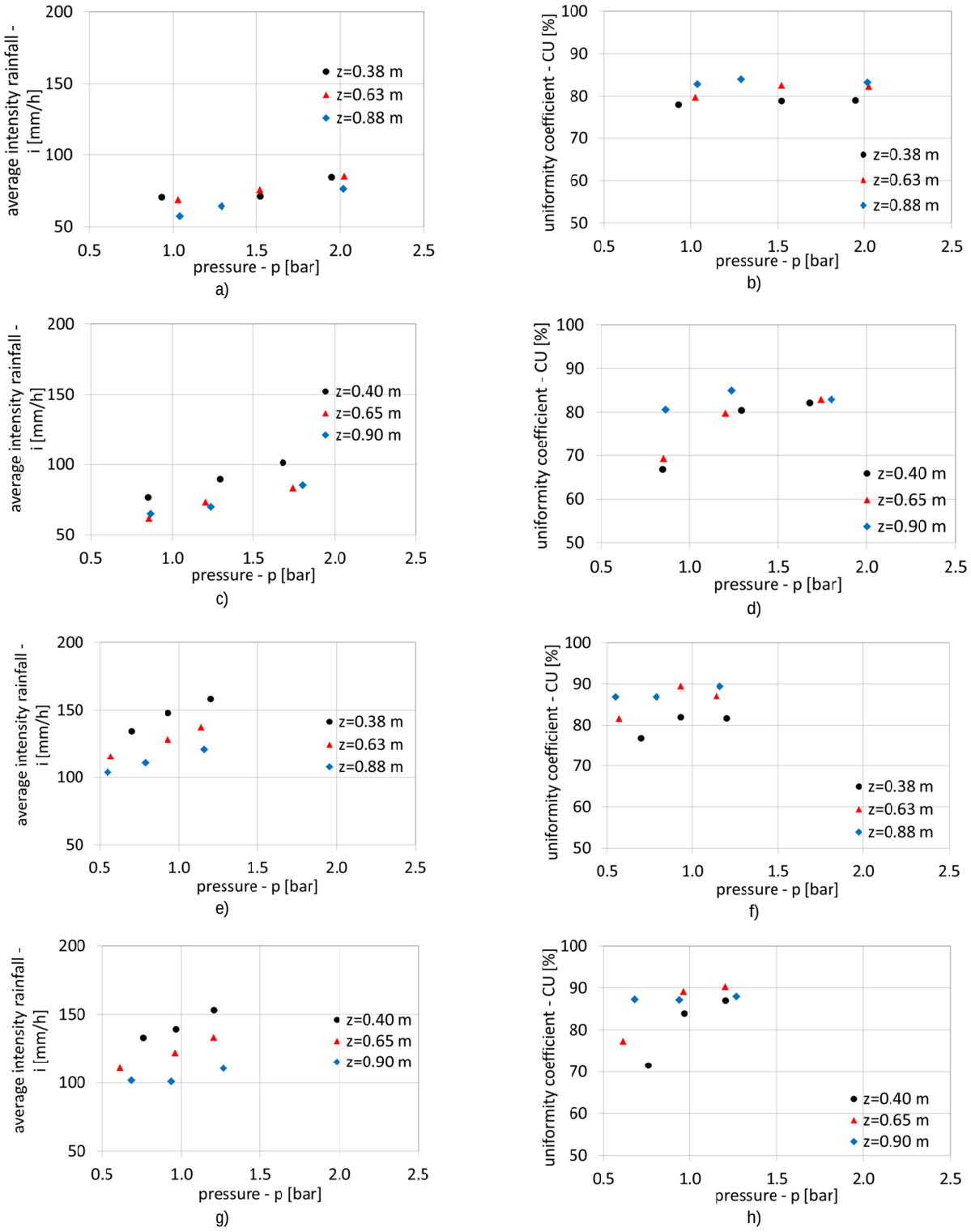

Figure 2-16. Results of the experiments with the rainfall simulator at varying operating pressures and nozzle elevations. p is the pressure measured by the sensor located in the highest corner on the right-hand side observing the pipe network from below, z designates the nozzles elevation above the surface. The graphs refer to the following configurations: a) and b) 3_1 with nozzles WSQ 14; c) and d), 3_1 with nozzles WSQ 20; e) and f), 7_2 with nozzles WSQ 14; g) and h), 5_3 with nozzles WSQ 20.

Two examples of rainfall distributions produced during the tests are reported in Figure 2-17. The left image refers to the 3_1 configuration with WSQ 20 nozzles and the right one to the 7_2 configuration with WSQ 14

nozzles. In both cases, the maximum intensity values are located along the longitudinal centerline, because of the overlap between the jets sprayed by nozzles positioned in front of each other.

Despite the small number of nozzles in the first configuration (3_1), a good uniformity coefficient is achieved ($CU = 85$ %) thanks to the large pressure ($p = 1.4$ bar) spreading the jet cone. In the second configuration the pressure value is smaller and around the inferior limit for acceptable values of the rainfall uniformity, which, based on the previous experiments with single nozzles, is 1 bar. Nevertheless, the large number of opened nozzles assures a high uniformity coefficient, equal to 90 %.

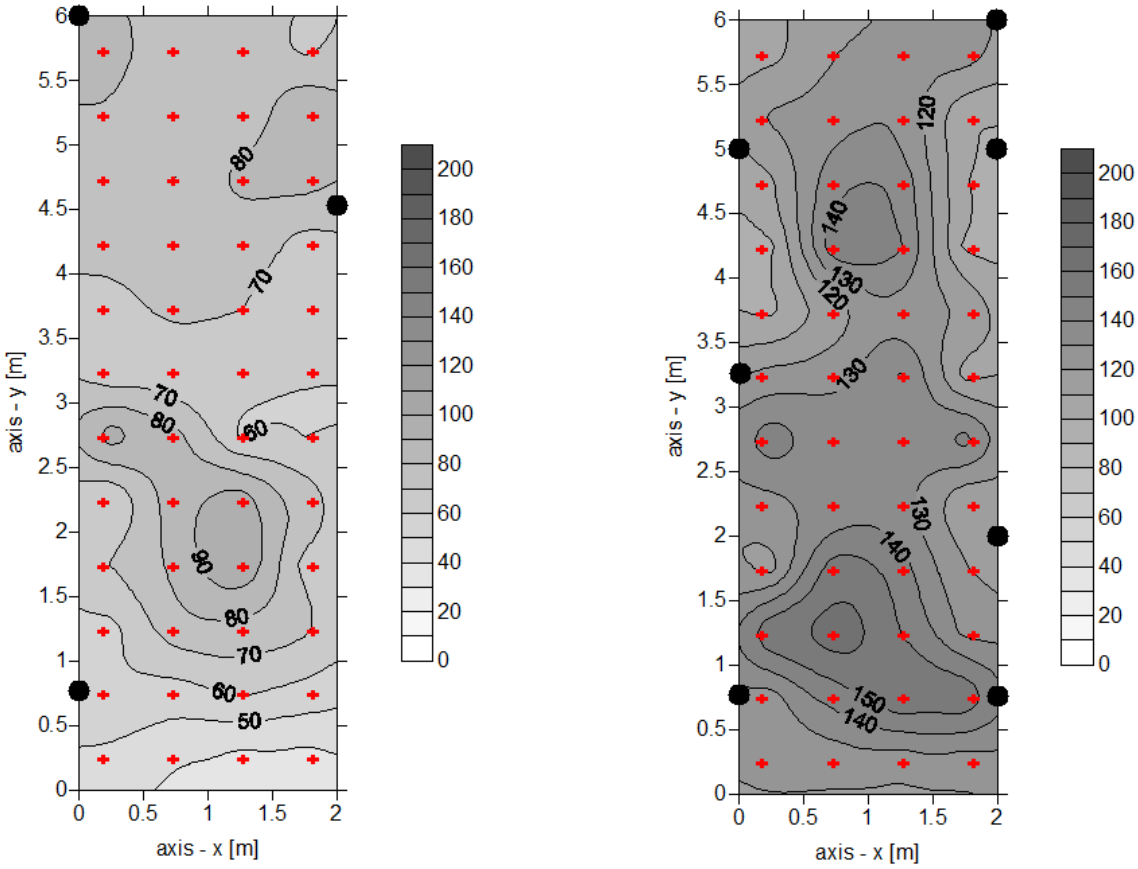

Figure 2-17. Rainfall distribution obtained during the tests with: (left) the 3_1 configuration with WSQ 20 nozzles, spray elevation z=0.90 m, and pressure p=1.4 m; (right) 7_2 configuration with WSQ 14 nozzles, spray elevation z=0.63 m, and pressure p=0.9 bar. The uniformity coefficients are *CU=85 %* and *CU=90 %*, respectively. Red crosses indicate the location of the rain gauges and black dots the active nozzles.

2.3.4 Drop size distribution

The drop size analysis, performed by the method described in Section 2.2.3 with a precision of 0.021 mm, assumes a minimum value of the drop sizes equal to 0.25 mm, in order to not count possible blots in the scanned image. Table 2-2 reports operating conditions of the experiments as well as the main results. Some tests were repeated with the same operating conditions and changing only the inclination of the surface (horizontal vs inclined).

Table 2-2. Operating conditions and results of the tests for the characterization of the drop size distribution.

	nozzle	operating pressure – p [bar]	horizontal surface nozzle elevation z [m]	D_{50} [mm] – median value of drop diameter distribution	D_{MEAN}[mm]– mean value of drop diameter distribution
test 1	WSQ14	1	0.90	0.423	0.48
test 2	WSQ14	1	0.70	0.423	0.49
test 3	WSQ14	1.5	0.40	0.423	0.45
test 4	WSQ20	1.5	0.40	0.423	0.50

	nozzle	operating pressure – p [bar]	inclined surface (γ=30°) nozzle elevation – z [m]	D_{50} [mm]– median value of drop diameter distribution	D_{MEAN}[mm]– mean value of drop diameter distribution
test 5	WSQ14	1.5	0.40	0.423	0.45
test 6	WSQ20	1.5	0.40	0.423	0.51
test 7	WSQ14	1	0.70	0.423	0.49

The relative frequency of the drop diameters resulting from the analysis exhibits a mode and is skewed to the right (Figure 2-18). The median diameter, which does not change in the experiments (Table 2-2), is equal to 0.423 mm, while mean values range from 0.48 to 0.51 mm. These dimensions are much smaller than the typical drop sizes of natural rainfall, which are reported as ranging from 1.5 to 2.5 mm (Lows and Parsons, 1943; Morin, 1993; Assouline et al., 1997; Krajewski et al., 2005; Uijlenhoet and Stricker, 1999; Abudi et al., 2012).

A commonly accepted distribution of the rain drop diameters derives from the exponential expression (Marshall and Palmer, 1948; Fox, 2004):

$$N(D) = N_0 exp(-\Lambda D), \qquad \textbf{(2)}$$

where:

$N(D) = \frac{n_i}{V_{tot}}$ is the number n_i [m^{-3}] of drops of diameter D[mm] divided by the total volume of the drops V_{tot}, $N_0 = \frac{n_{tot}}{V_{tot}}$ is the total drop concentration, and $\Lambda = \frac{3.67}{D_0}$ is a parameter related to the median drop diameter D_0 of the size spectrum for the natural rainfall (D_0 = 1.5 mm),.

Excluding the mode, equation (2) matches well the experimental relative frequency (Figure 2-18), with a coefficient equal to 2.25 instead of 3.67.

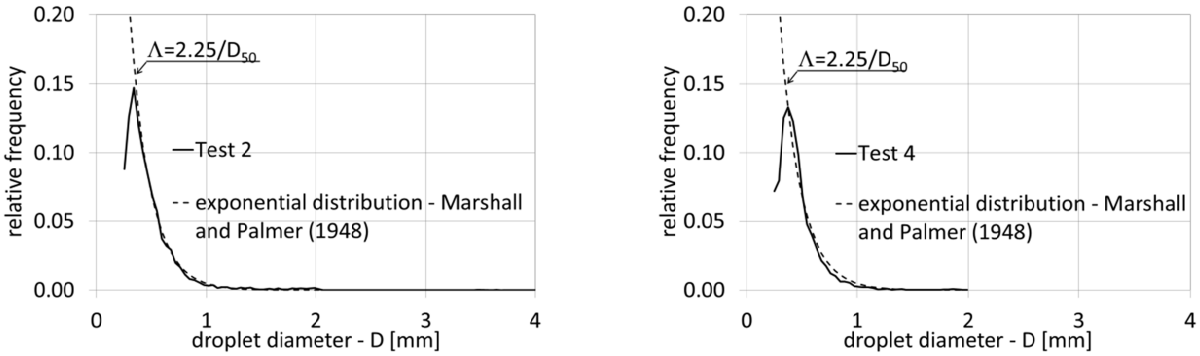

Figure 2-18. Raindrop diameter distribution from the experiments performed with the oil method and comparison with the exponential law suggested by Marshall and Palmer (1948).

Figure 2-19 compares the results between tests 4 and 6 (Table 2-2), characterized by horizontal and inclined surfaces, respectively. Although the frequency distributions do not differ, the spatial distribution of the characteristic diameters is substantially modified by the sloping geometry. The top graphs in Figure 2-19 represent the spatial distribution of the median diameters: on the horizontal surface, the median diameters are symmetrically distributed with respect to the median horizontal axis (y = 1 m), with larger drops falling far from the injection point; on the inclined surface, the spatial distribution is not symmetric and reflects the longitudinal sloping angle of both the pipe feeding the nozzle and the irrigated area. For instance, note how the median diameter of the samples collected in the petri dish 41 is much larger for the inclined surface compared to the horizontal one (Figure 2-19).

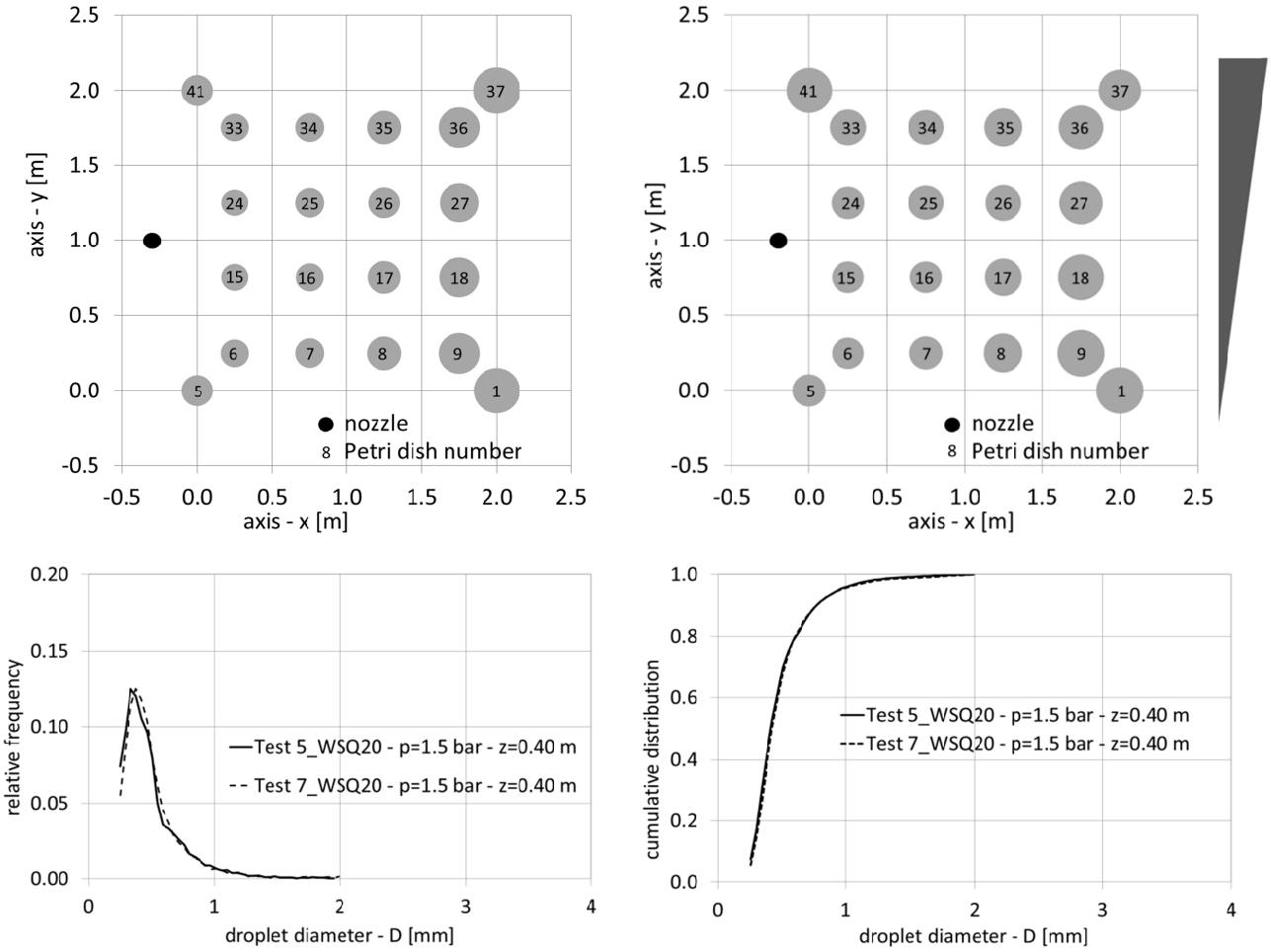

Figure 2-19. Comparison between drop size distributions from tests 4 and 6 (Table 2-2). Top graphs show the spatial distribution of the median diameter: the size of the grey circles are proportional to the diameter value; the black dot indicates the position of the nozzle. Bottom graphs show the drop size probability distributions in terms of (left) relative frequency and (right) cumulative probability.

The experiments performed with different pressure values (tests 2 and 3) and different nozzles (tests 3 and 4) highlight some slight variations in the drop size distributions, which can only be appreciated by the changes in the mean diameters (Table 2-2): as the operating pressure increases, the mean diameter decreases, due to a

stronger nebulization of the drops. This is somewhat in contrast with natural rainfall, for which larger intensities, obtainable here only with higher pressure for the nozzle, are typically associated to increasing mean drop sizes. For the second couple of experiments (tests 3 and 4) the results show again an increase in the mean drop size related to the geometry of the nozzle, with the WSQ 20 nozzle exhibiting larger discharge rate and mean diameter than the WSQ 14 nozzle.

2.3.5 Spray numerical model

An application example of the numerical model described in Section 2.2.4 can be visualized in Figure 2-20: a small sample with only three drop diameters is considered, to show the evolution of the drop trajectories and the drop distribution on the irrigated area. It is immediately apparent that the largest drops reach the longest distance, while the smaller particles fall closer to the injection point. These results are qualitatively consistent with the data from the previous experimental analysis shown in Figure 2-19.

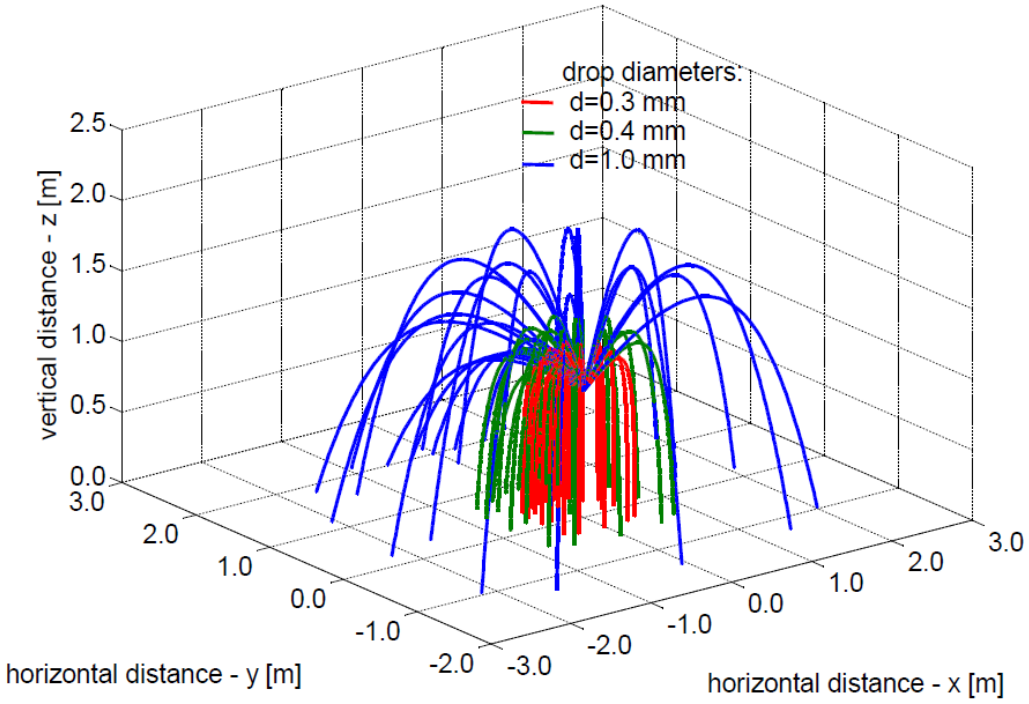

Figure 2-20. Raindrop trajectories determined with the numerical model for a sample with three drop diameters, x_start=0 m, y_start=0 m, z_start=0.90 m, spray initial velocity u=7 m/s, $\alpha = 30°$, $\beta = 100°$, $\gamma = 0°$, $\theta = 0°$, $n_p = 5$ (see Figure 2-8 for an explanation of the symbols).

In order to run the model with the real distribution of drop diameters, the samples of droplet dimensions are derived using the distributions resulting from the previous experiments: the sample for a single model run is taken from all the petri dishes and is replicated for each of the ${n_p}^2$ starting directions (Figure 2-8 on the right) at the injection point. The size of the sample is suitably reduced, compared to the real diameter data, to improve the model efficiency without losing the representative statistics. The calibration of the numerical model is made with respect to the injection velocity of the drops. To this aim, a comparison between the numerical

and experimental relative frequency of drops with a defined diameter is carried out. The results are shown in Figure 2-21, which refers to the test 3 with the WSQ 14 nozzle (Table 2-2). The nozzle is located in x=0 m, pointing upwards with an angle with respect to the vertical axis equal to 30° (Figure 2-4, second position). The experimental data shown in the figure are obtained with the oil method by detecting the drop samples collected in the petri dishes along a line parallel to the spray direction (Figure 2-7).

The comparison is done for the following values of diameters: D_1 = 0.339 mm, D_2 = 0.381 mm, D_3 = 0.423 mm, D_4 = 0.55 mm, and D_5 = 0.593 mm. From the experimental data (continuous line), the distribution of landing points for the particles at varying diameters can be observed: droplets with a small diameter (D_1 and D_2) fall mainly close to the nozzle, while drops with larger diameter (D_4 and D_5) fall far from the nozzle, as it has been previously described. The numerical results match satisfactorily the experimental data, especially if we consider the simplified hypothesis underlying the method. In particular the location where the maximum concentration of a drop diameter occurs is captured well by the numerical solution, for all the considered diameters, confirming that the assumption of an initial spray velocity independent of the drop size is acceptable.

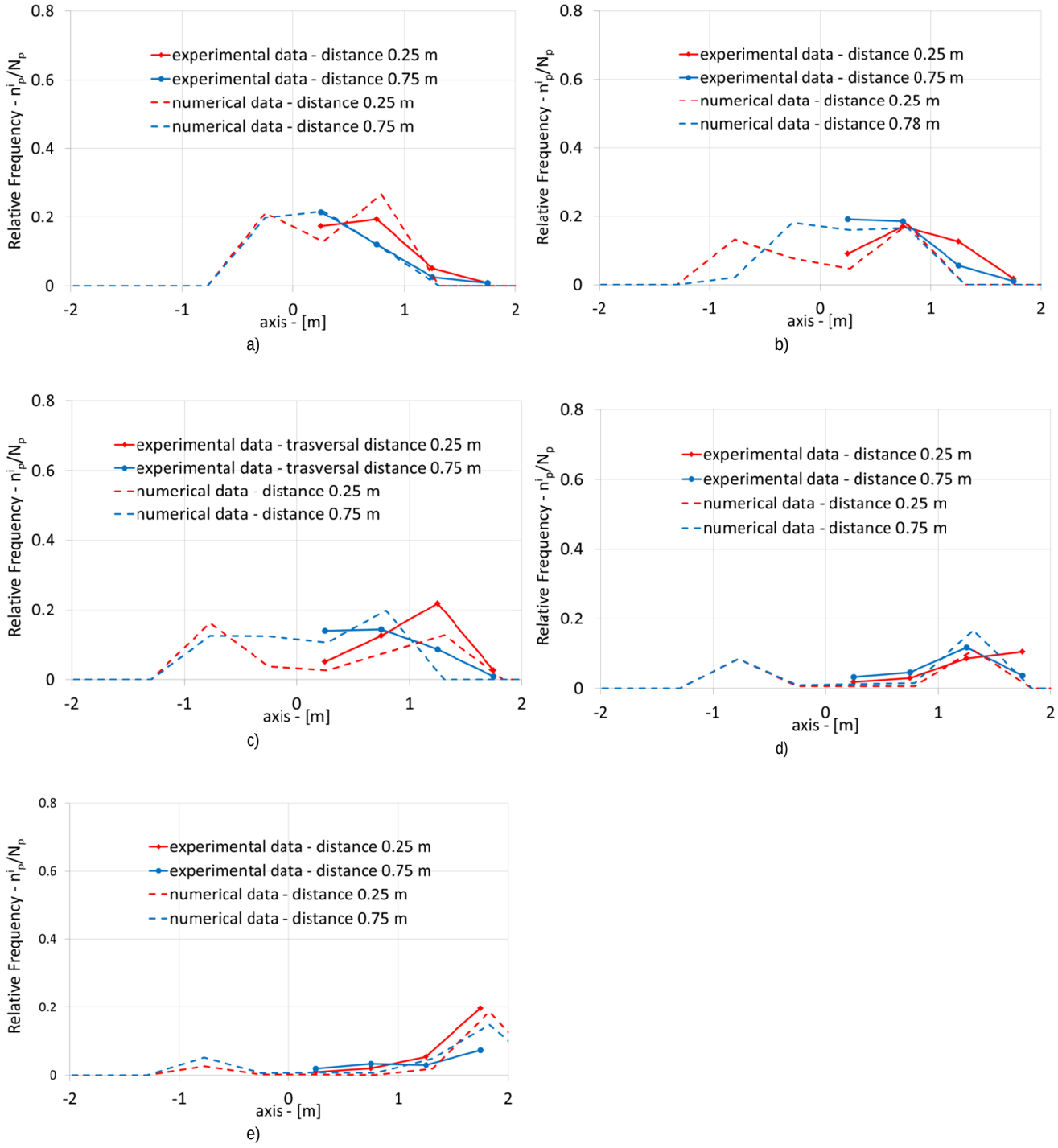

Figure 2-21. Comparison between experimental data and model results in terms of spatial distribution of the drop diameters on the irrigated area. Experimental data refer to the test number 3 (Table 2-2).The term "distance" in the legend is measured transversally between the axis of the nozzle and the row of petri dishes considered in the analysis.

The calibration of the injection velocity is repeated for all the tests conducted with the oil method at varying pressure conditions. The calibrated values of injection velocity allow us to obtain an estimate of the functional relationship between the operating pressure and the injection velocity of the nozzles. Figure 2-22 shows the

relationship found for the WSQ 14 nozzle, derived by considering two values of pressure (1 and 1.5 bar from tests 2 and 3, respectively; zero pressure corresponds obviously to zero velocity).

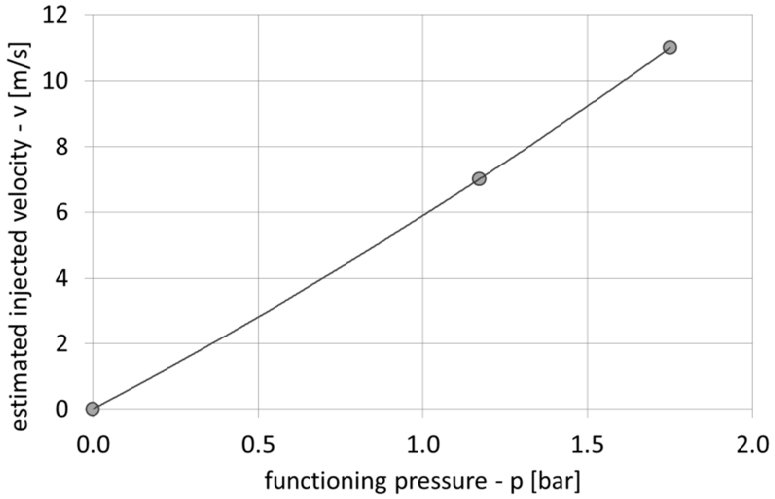

Figure 2-22. Experimental relationship between operating pressure and spray velocity assessed with the calibration of the numerical model for the nozzle WSQ 14.

2.3.6 Potential erosion

The calibrated numerical model can be used to assess the distribution of the kinetic energy associated to the drop impact with the soil, i.e., an index for the erosion potential. The kinetic energy is $E_{K,D} = \frac{1}{2} m_D {v_D}^2$, where m_D is the mass of a water particle and v_D its velocity.

The potential erosion at the soil is suitably related to the specific kinetic energy, $e_k \left[\frac{J}{m^2 mm}\right]$, which depends on the drop size (Van Dijk et al.,2002; Fox, 2004) through:

$e_K = \frac{1}{2}\rho \sum_{i=1}^{k} f_i {v_i}^2$,

where: ρ is the water density, v_i is the velocity at the impact, and f_i is the mass fraction of the particles with velocity equal to v_i.

Denoting with the subscript p the p-th cell deriving from a regular discretization of the irrigated area, the mass fraction $f_i = \frac{{V_i}^p}{V_p}$ is expressed as the ratio of ${V_i}^p$, the volume of the i-th particle falling on the p-th cell with an impact velocity v_i, and the total water volume V_p falling on the p-th cell.

The impact velocity is $v_i = \sqrt{{u_x}^2 + {u_y}^2 + {u_z}^2}$, comprehensive of all the velocity components $u_x, u_y, and\ u_z$ of the Cartesian system.

The distribution of specific kinetic energy for a number of selected simulations is shown in Figure 2-23. Two operating conditions at the injection are considered for both a horizontal surface and a sloping surface, the latter with the same angle of the artificial slope. The width of the simulated surface is 2 m and the length is

12 m, in order to reproduce the possible influence of the nozzle regardless of its position along the real artificial slope (2 m × 6 m = 12 m^2). The figures show the zones that are more susceptible to erosion: areas located farther from the nozzle are subject to the highest kinetic energy, due to the effect of the largest drops. It is interesting to note that the zone close to the nozzle, where the rainfall intensity reaches the peak values (Figure 2-13), is characterized by a negligible potential for soil erosion. This observation confirms the limited effect of the total water amount on the erosion, which is controlled by the drop size and the corresponding magnitude of the velocity vector. The comparison between the horizontal and the sloping geometry highlights a slight increase of the potential erosion for the latter configuration. The maximum values of the kinetic energy fall within 11.5 and 20 $J/(m^2 mm)$, which, according to Laws and Parsons (1943) and Wischmeier and Smith (1958, 1978), would be equivalent to the energy associated to a natural rainfall intensity ranging from 0.5 to 9.2 mm/h. Therefore, the potential soil erosion caused by the produced rainfall can be considered very limited, such that we can neglect its effect during the experimental tests on the artificial slope.

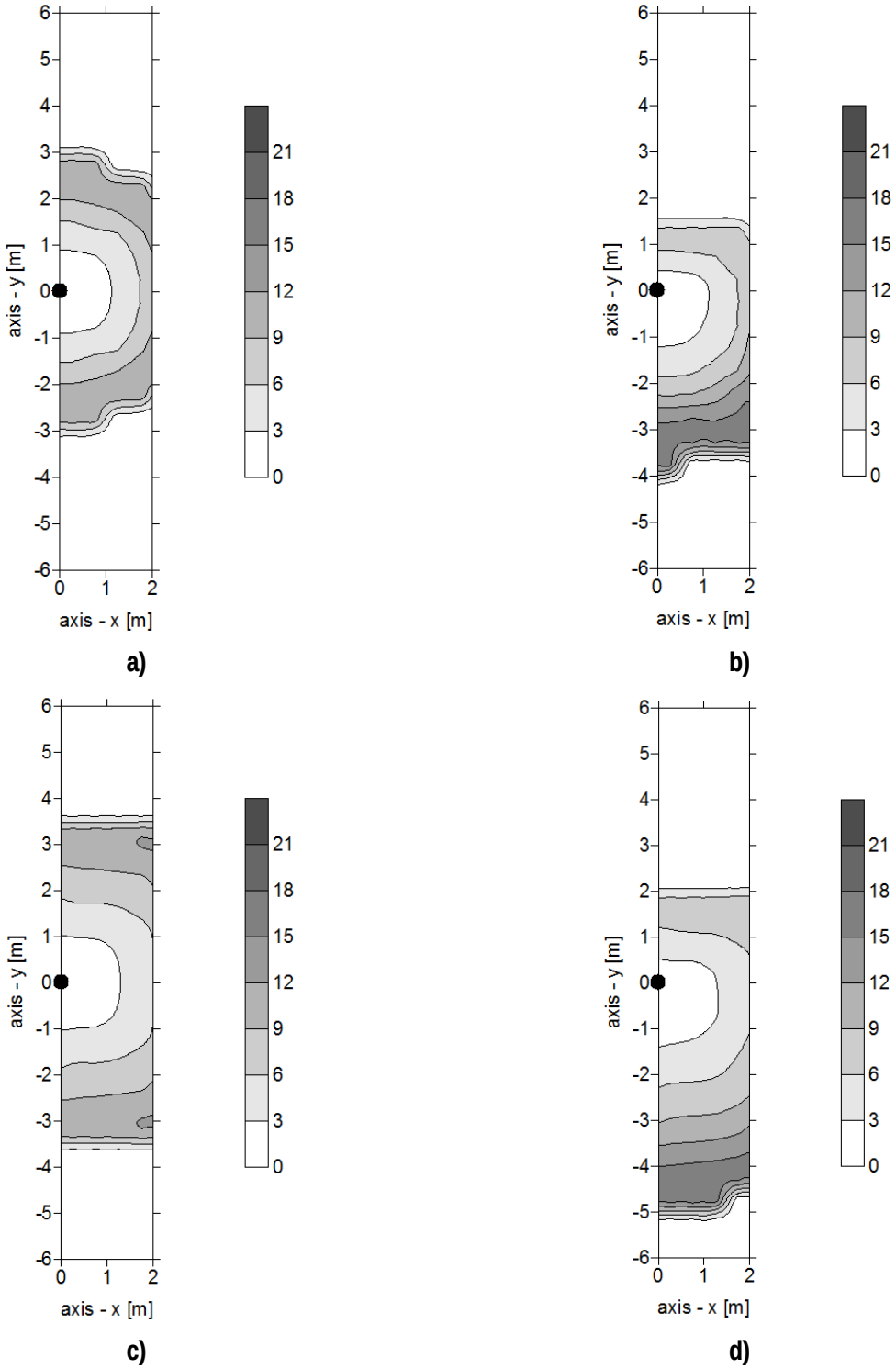

Figure 2-23. Spatial distribution of the specific kinetic energy (J/ m²mm) at the impact with the surface: the results are produced with the numerical model simulating the drop trajectories from the injection point at the nozzle (black dot). The graphs refer to the following cases : a) nozzle WSQ 14, horizontal surface; b) WSQ 14, sloping surface; c) WSQ 20, horizontal surface; d) WSQ 20, sloping surface.

2.4 DISCUSSION

2.4.1 Rainfall simulator

Several experiments have led to a detailed understanding of the key factors affecting the rain produced by the nozzles and the elements that allow a flexible management of a rainfall simulator suitable for a full-scale artificial hillslope of 2 by 6 m^2.

The analysis started with the results of a single nozzle, which is the primary element constituting the rainfall simulator. The first tests helped to understand the optimal position of the nozzle with respect to the spatial distribution of the generated rain; a nozzle located at the edge of the irrigated area and pointing upwards reveals the best configuration for the uniformity coefficient ($CU \cong 70\ \%$) on a small square area of 2 m per side. Compared to the first central position ($CU \cong 30\ \%$) of the nozzle pointing downward (Figure 2-4), the distribution of the rain is more widespread, because of the larger area reached by the raindrops. This advantage comes at the cost of a significant reduction in the average rainfall intensity and, consequently, a decrease of the efficiency in the water usage. However, the rainfall simulator is intended to be used for the analysis of heavy rainfall effects on the soil and thus the uniformity requirement is considered more important. By changing the pressure from 0.5 to 2 bar the rainfall intensity increases proportionally thanks to the increasing discharge, which is related to the operating pressure. The uniformity coefficient is not satisfactory for operating pressures lower than 1 bar ($CU < 50\ \%$), whereas for higher pressure the CU is acceptable. Therefore, a pressure of about 1 bar is considered as the lower threshold for a proper functioning. Rainfall intensity decreases with the nozzle elevation above the surface when keeping constant the operating pressure.

Overall, the uniformity coefficient does not obey to a functional law that allows its prediction for specific operating conditions. This is probably due to uncertainties during the experiments that cannot be recognized and/or controlled, such as air turbulence and possible distortions of the pipe feeding the nozzle. Nevertheless, it is possible to identify a range of pressures and nozzle elevations that ensure the minimum uniformity required by our experiments.

The same experiments were repeated on a sloping surface, with the same inclination as the artificial slope. In this experiments, also the pipe feeding the nozzle is inclined and parallel to the irrigated area. The rainfall distributions obtained by several combinations of nozzles over the artificial hillslope suggest that the spacing between the nozzles must not exceed 1 m (Figure 2-6). This guarantees a satisfying uniformity coefficient and a recognizable linear behavior of the rainfall intensity as a function of pressure and nozzle elevations, as already found for the single nozzle. The average intensity can be approximated by different expressions $i(z, p)$ for each combination of nozzles as a function of the reference pressure p and the elevation above the soil surface z . For each nozzles configuration the function is expressed as:

- configuration 3_1 with WSQ 14 nozzles: $i[mm/h] = 59.88 - 18.29z[m] + 16.36p[bar]$
- configuration 3_1 with WSQ 20 nozzles: $i[mm/h] = 67.12 - 33.05z[m] + 25.44p[bar]$
- configuration 7_2 with WSQ 14 nozzles: $i[mm/h] = 135.04 - 62.41z[m] + 37.04p[bar]$
- configuration 5_3 with WSQ 20 nozzles: $i[mm/h] = 141.32 - 74.17z[m] + 30.98p[bar]$.

The maximum relative error associated to these functions is 9.93 % for experimental values lower than 100 mm/h and 5.78 % for larger values. The mean relative error is 4.24 % for intensities lower than 100 mm/h and 1.97 % for larger values. A brief calculation leads to a maximum and mean absolute errors equal to 7 mm/h and 3 mm/h, respectively. These values are smaller than possible inaccuracies deriving from the uncertainties related to the operating conditions (for example, the nozzle elevation above the soil, which is never perfectly the same along the entire network, or the steadiness of the pressure, susceptible to possible uncontrolled fluctuations of the municipal water supply). For these reasons, we can safely state that the experimental relationships can be considered reasonably accurate for our purposes. It is interesting to note that in the above functions the coefficients of the elevation z are always greater than the corresponding pressure. This observation leads to the possibility of managing the rainfall simulator for reproducing the desired values of rainfall intensity as follows: after choosing the nozzles configuration, first the appropriate range of elevations is chosen and, subsequently, the regulation is refined by adjusting the reference pressure. The range of elevations can be identified based on the uniformity found in the experiments (Figure 2-16). For example, the configuration 3_1 using WSQ 20 nozzles is not suitable for a combination of $z < 0.65$ m and $p < 1$ bar. The WSQ 30 nozzle, which is tested as single nozzle, is not adopted in the rainfall simulator because of the great discharge rate, causing large energy losses in the network preceding the simulator.

Table 2-3 reports a summary of the characteristics for the configurations investigated. The index $\eta[\%] = 100\frac{Q_{eff}}{Q_u}$ represents the efficiency of the simulator, where Q_u is the total discharge from the nozzles and $Q_{eff} = i \times S$ is the effective flow, i being the average intensity and S the irrigated area (12 m^2). The data (Table 2-3) demonstrate that the greater efficiency is achieved for the highest intensities (69 %), because a major fraction of the sprayed jet falls on the soil surface, while for the lowest intensity ($i = 50$ mm/h) the efficiency of the simulator is much worse, with one half of the water amount falling out the soil.

Table 2-3. Summary of nozzle configurations and corresponding values of average rainfall intensities, operating conditions and water use efficiencies.

i [mm/h]	Q_{eff}[l/min]	configuration	functioning conditions	Q_u[l/min]	η
50	10	WSQ20_3_1	z=1.2 m; p=0.9 bar	22.5	44 %
75	15	WSQ20_3_1	z=1.0 m; p=1.6 bar	29.1	52 %
100	20	WSQ20_5_3	z=1.0 m; p=1.1 bar	40.9	49 %
125	25	WSQ14_7_2	z=0.75 m; p=1.0 bar	42.1	59 %
		WSQ20_5_3	z=0.75 m ; p=1.3 bar	43.7	57 %
150	30	WSQ14_7_2	z=0.4 m; p=1.1 bar	43.6	69 %
		WSQ20_5_3	z=0.4 m; p=1.2 bar	43.3	69 %

i: rainfall intensity; z: nozzle elevation above the surface; p: operatingpressure; Q_{eff}: effective flow; Q_u: total discharge; η: efficiency index

2.4.2 Potential erosion

A detailed analysis of the drop size frequency and its spatial distribution on the irrigated area was carried out by a series of experiments with the oil method. The impacts of an inclined surface are limited to the spatial distribution of the drop sizes, while their overall cumulative distribution is not affected. The experimental distribution matches well the exponential law proposed by Marshall and Palmer (1948), although the median diameter of the produced rainfall is much smaller than that typical of natural rainfall. The evaluation of the raindrop sizes is particularly relevant for the potential erosion that can be generated at the impact with the soil, depending on the drop sizes and on their final velocity. The geometry of the simulator is such that the equilibrium between gravity and the drag force cannot be achieved in our experimental facility. Therefore, an estimation of the impact velocity is carried out by means of a numerical model, whose calibration provides a useful tool to evaluate the soil erosion potential associated to the rainfall simulator.

The kinetic energy at the impact calculated by the model for specific scenarios of operating pressures, position and orientation of the nozzle, and inclination of the irrigated area (Figure 2-23) shows that the maximum erosion occurs where the produced rainfall rate is low, which corresponds to the zones reached by the largest drops. The sloping surface induces a slight increment of the kinetic energy in the zone close to the slope toe. However, maximum values do not exceed $20\,J/(m^2 mm)$, which corresponds, in terms of potential erosion, to natural rain intensities lower than $10\,mm/h$. This allows us to use the simulator for producing heavy rainfall intensities, ranging from 50 to $150\,mm/h$, avoiding erosion processes that could compromise our future experiments on the artificial slope.

3 CALIBRATION OF WATER CONTENT REFLECTOMETER SENSORS WITH A LARGE SOIL SAMPLE

3.1 INTRODUCTION

The importance of determining volumetric water content in porous media is widely recognized in a broad array of disciplines, from hydrology to agronomy (Schmugge et al., 1980; Brisco et al., 1992), soil moisture exerting a major control on main fundamental processes, such as rainfall-infiltration-runoff partitioning, surface energy balance, landslide triggering, etc..

In the last decades, the hydrologic research has been characterized by a widespread use of field sensors for the direct measurement of water content in situ, with several advantages over laboratory-based techniques, which are destructive, time-consuming and thus impractical for large-scale determinations (Topp et al., 1980). Among others, the techniques based on microwave produced by portable sensors offer great performances, thanks to the link of soil dielectric properties with the water content (Dobson and Utaby, 1986; Schmugge et al., 1986).

Time Domain Reflectometry (TDR) is one of the most effective electromagnetic techniques (Jones et al. 2002; Robinson et al., 2003; Kelleners et al., 2005). It provides measurements of the target soil apparent dielectric constant K_a, which in turn is converted into the soil volumetric water content (Schmugge, 1980; Hallikainen et al., 1985): this is possible because at microwave frequencies the dielectric constant of the soil grains is much smaller than that of the water, in such a way that the dielectric constant of wet soils is very sensitive to the water content. TDR instruments usually consist of an electric unit generating a step signal, which propagates down a standard transmission line through the receiver, from which two or three rods depart. The rods work as waveguides inserted in the soil, which represents a dielectric medium: after propagation as a plane wave through the soil, the signal (0.1 to 1 GHz frequency range) is reflected from the end of the transmission line and returns back to the TDR sampling unit (Brisco et al. 1992; Davis and Annan, 1977). The output of the measurements are the velocity of the propagation wave and its attenuation, which depend on K_a.

Nowadays, TDR can be considered the most established soil moisture measurement technique, as evidenced by countless field applications and the popularity of Topp's equation (Topp et al., 1980), as well as a number of subsequent developments.

Recently, new electromagnetic techniques have been adopted to measure soil electrical properties in a cheaper way. Among these, transmission line oscillators, better known as Water Content Reflectometers (WCRs), are particularly interesting because they still operate in the time domain, like TDR, but do not require a common electric unit connected to each sensor (Kelleners et al., 2005). In fact, WCR probes present an oscillator that is embedded in the sensor head and directly generates consecutive voltage pulses, whereby the arrival of the reflected pulse triggers the next pulse (Kelleners et al., 2005). As a result, the output consists of the period (t) of a square wave propagating along the two rods inserted in the soil. This time depends directly on the soil water content and can be linked to K_a.

The main advantages of WCR over TDR are the smaller cost (Hansson and Lundin, 2006) and the independence from the length of the transmission cables, which, in the TDR, can strongly affect the wave velocity and its attenuation, causing misleading signals. On the other hand, WCR is still a relatively new technique, without a background as well-established as the TDR: therefore, further investigations are needed on its reliability, especially in terms of the calibration law adopted to convert the output signal to water content. Popular calibration relationships include the one proposed by Bilskie (1997), where the square wave period t is a function of the apparent dielectric number K_a, accounting for a delay t_{delay} due to the electronic features of the probe (Hansson and Lundin, 2006; Kelleners et al., 2005), and by Campbell Scientific (2003) (Campbell and Anderson, 1998), where a direct link between the raw output signal and volumetric water content is suggested.

Previous calibration techniques were typically characterized by the small size of the soil samples being probed. Topp et al. (1980), for instance, used soil samples with an internal diameter of 5 cm and a length varying from 33 to 100 cm, while Kelleners et al. (2005) recurred to fluid experiments performed in 36 cm high polyvinyl chloride (PVC) columns with 28 cm i.d.. Only a few studies were carried out with samples at a larger scale, including Vaz et al. (2002), who carried out the calibration of TDR probes (and concurrently obtained the retention curve of the soil) with a funnel apparatus containing a glass porous plate of 95 cm diameter, and Hansson and Lundin (2006), who proposed an experimental calibration procedure for WCR by adopting a 20 cm wide × 40 cm long × 20 cm high container that was closed at the boundaries except at the top surface. With this last configuration, when the wetting front reaches the impermeable bottom, it is reasonable to assume that the soil moisture distribution is not uniform, but characterized by larger water content at the bottom, where the probe is located, resulting in a calibration relationship affected by a slight overestimation of the water content.

The main objective of this paper is to develop a calibration relationship for WCR sensors (model CS616 by Campbell Scientific) specific for a soil to be used in an experimental slope with maximum height of 3.5 m, width of 2 m, and length of 6 m. This facility will be subject to artificial rainfall and continuously monitored by means of tensiometers and WCRs, in order to study the infiltration dynamics and its effect on the triggering of shallow landslides. However, measurements of water flow in soils at such scale can be affected by local heterogeneity, which cannot be properly evaluated by sensors calibrated with small-size samples, unless a very fine and expensive sensor network capable of capturing this spatial variability is deployed. Here we suggest tackling this issue with a limited number of sensors, by means of a calibration relationship developed on a control volume large enough to be well-representative of the average water content sampled by the probe in the real application of the full-scale device. To this aim, a 60 cm high × 50 cm wide × 60 cm long box container was adopted to calibrate the WCR sensors. The height of the box, i.e., the soil sample, is equal to that of the soil layer that will be placed on the artificial slope to carry out the planned infiltration experiments.

Moreover, particular care was used in the design of the container to ensure that the water content profile during the experiments was as uniform as possible and to reproduce infiltration dynamics similar to those we expect from the experiments in the full-scale slope, in order to develop the calibration procedure in a setting that is as close as possible to the field conditions.

3.2 MATERIAL AND METHODS

3.2.1 Experimental device

In order to relate the volumetric water content averaged over a large control volume with the raw signal recorded by the WCR probes, i.e., to reach a meaningful calibration, we need to reproduce a known steady-state hydrologic condition in a soil sample of suitable dimensions. To this aim, we designed an ad hoc experimental device containing a soil sample whose hydrologic state is continuously monitored and controlled by means of tensiometers and WCR sensors. The use of tensiometers allows us to measure the pressure head and to check whether or not saturation conditions have been reached. Our calibration procedure takes also into account the effect of porosity, by repeating the measurements with the same soil but different degrees of compaction.

The soil considered is a silty sand with a highly uniform grain size distribution (Figure 3-1): the coefficient of uniformity is $C = \frac{D_{60}}{D_{10}} = 2.3$, where D_{60} is the grain diameter at 60 % passing in weight and D_{10} is the grain diameter at 10 % weight passing in weight.

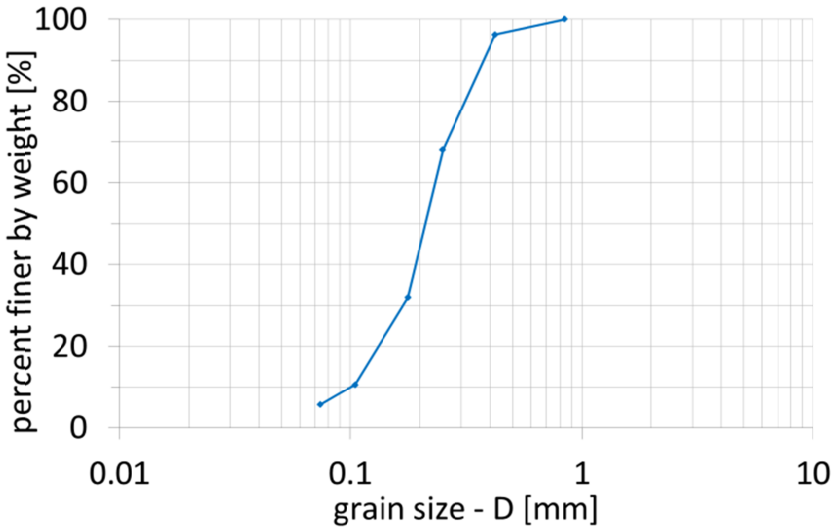

Figure 3-1. Grain size distribution of the sand used in the experiments.

The calibration device (Figure 3-2 and Figure 3-3) consists of a large Plexiglas box, with 50 cm x 60 cm base area and 60 cm height. The top of the box is completely open, such that a rainfall simulator can apply to the soil the desired rain intensity. The rain is released by 50 hypodermic needles installed on the bottom of an otherwise impermeable container, with base area equal to that of the Plexiglas box. The water supply is guaranteed by a constant head reservoir producing a constant discharge that can be measured with a chronometer and a graded cylinder. After the appropriate water level in the rainfall container is achieved, the desired rain intensity is realized on the soil surface and a wetting front propagates through the soil sample

down to the bottom, whe re, thanks to numerous 1 cm-diameter holes, the water is allowed to drain. In this way a steady-state condition is obtained by means of a constant flux through the sample, stable pressure head and water content.

At the base, a weight probe monitors the time evolution of the sample weight (P_{tot}), allowing us to estimate the changes of soil moisture; at steady-state, the weight is related to the spatial average of water content θ_{mean} through the following equation:

$$\frac{P_{tot}}{V} = \gamma_s(1-n) + \theta_{mean}\gamma_w \qquad \textbf{(3)}$$

where n is the mean porosity, V is the volume of the sample, γ_s is the specific weight of the sand (γ_s = 26.66 kN/m^3 from a pycnometer test), and γ_w the specific weight of water (γ_w = 9.81 kN/m^3).

Three tensiometers and three WCR probes in specular positions are arranged in the soil at depths of 10, 25, and 40 cm, for measuring water suction head and raw water content data in terms of period t [μs]. The tensiometers can be pushed into the soil thanks to three holes in a lateral face of the container at the respective depths, such that the ceramic cups are well inside the soil. The three WCR probes are entirely located within the soil sample, without external parts that could compromise the correct measure of the electric wave period along the two rods.

A geotextile lies on the bottom between the sample and the base holes, to prevent soil grains exiting the device.

All data from the tensiometers, the WCRs, and the weight cell are collected and recorded by an acquisition system from Campbell Scientific (CR 1000), with a frequency of 0.5 Hz.

Figure 3-2. Experimental device used for the calibration of the WCR probes

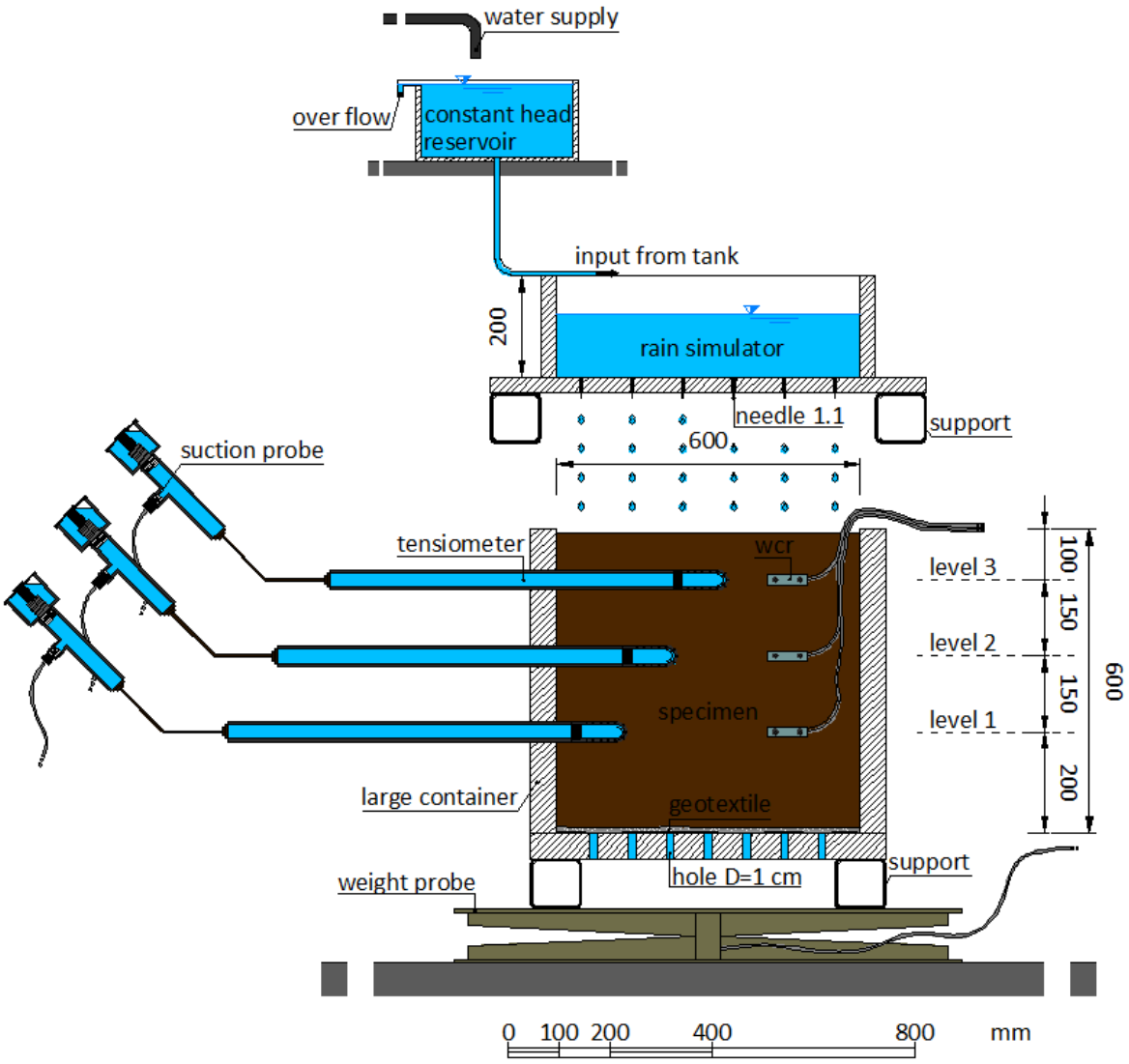

Figure 3-3. Experimental device employed for the calibration of WCR probes for a large soil sample.

3.2.2 Theoretical background

The geometry of the experimental device allows us to schematize the soil sample with a one-dimensional vertical column. The wetting front generated by a rainfall ($r < K_s$, where K_s is the saturated hydraulic conductivity) applied at the top of the sample induces an increase of the water content along the column as the front moves downward. When the wetting front reaches the bottom, the flux from the rainfall simulator is equal to the flux exiting the sample at the base, i.e., steady-state is established, the total mass of the sample remains constant, and, under the hypothesis of soil homogeneity, water content and suction are spatially constant. After the rain stops, the total mass starts decreasing as the sample drains: the evolution of the volumetric water content can be schematized with a trailing wave describing a faster decrease of the soil moisture at the top than at the base.

A preliminary simulation by means of the Richards equation solver Hydrus-1D (Šimůnek et al., 2012) confirms that the process occurs as described above. Figure 3-4 shows the evolution of water content and pressure head for a wetting and drying cycle as simulated in a vertical column of 56 cm height. The theoretical schematization represents well the experimental tests planned for the WCR calibration: the soil is homogeneous, with porosity equal to $n = 0.585$, and is subject to a rainfall of intensity 40 mm/h and duration 5 h, followed by drying. The top boundary condition is prescribed imposing flux equal to the rain intensity and the bottom boundary condition is free drainage.

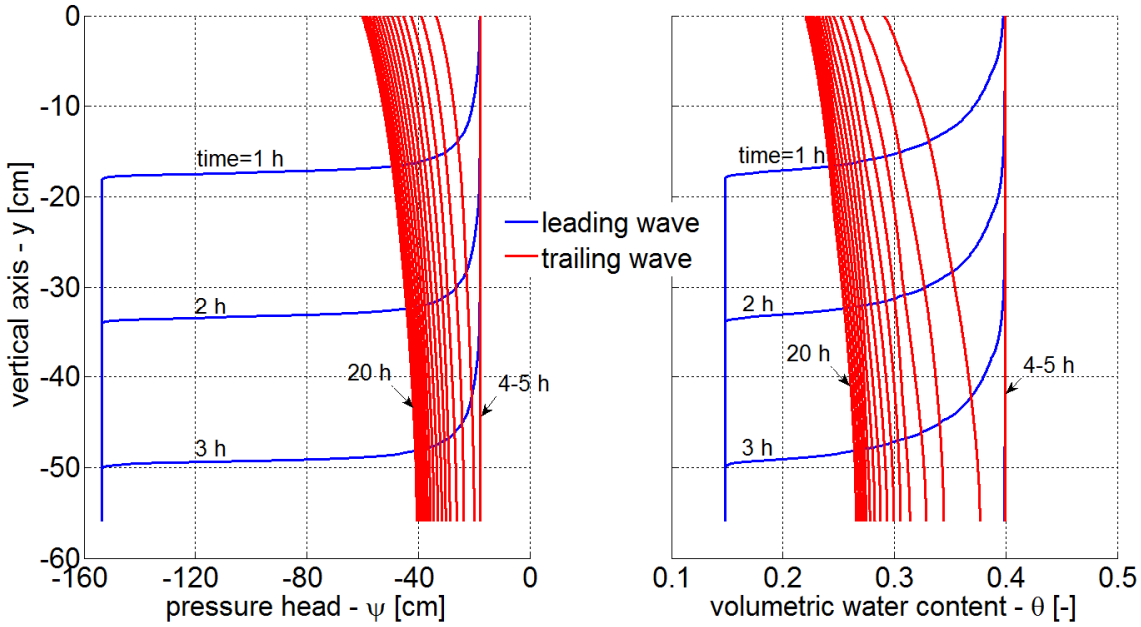

Figure 3-4. Soil water pressure head (left) and volumetric water content (right) profiles for time step Δt=1 h as simulated by Hydrus 1D in a vertical column.

Figure 3-5 shows the time series of water content and pressure head at the same depths of the probes arranged in the real sample, confirming the lack of water content and pressure head gradients at steady-state. Based on the one-dimensional Darcy's equation:

$$v = -K(\theta)\frac{\partial h}{\partial z} = -K(\theta)\left(\frac{\partial \psi}{\partial z} - 1\right)$$

where v is the specific discharge, $K(\theta)$ is the relative conductivity of the soil sample, h is the water potential, z is the vertical axis pointing downward, and ψ the water pressure head, the solution corresponds to a condition where the flux v, which is equal to the applied rainfall rate r, becomes equal to the hydraulic conductivity $K(\theta)$.

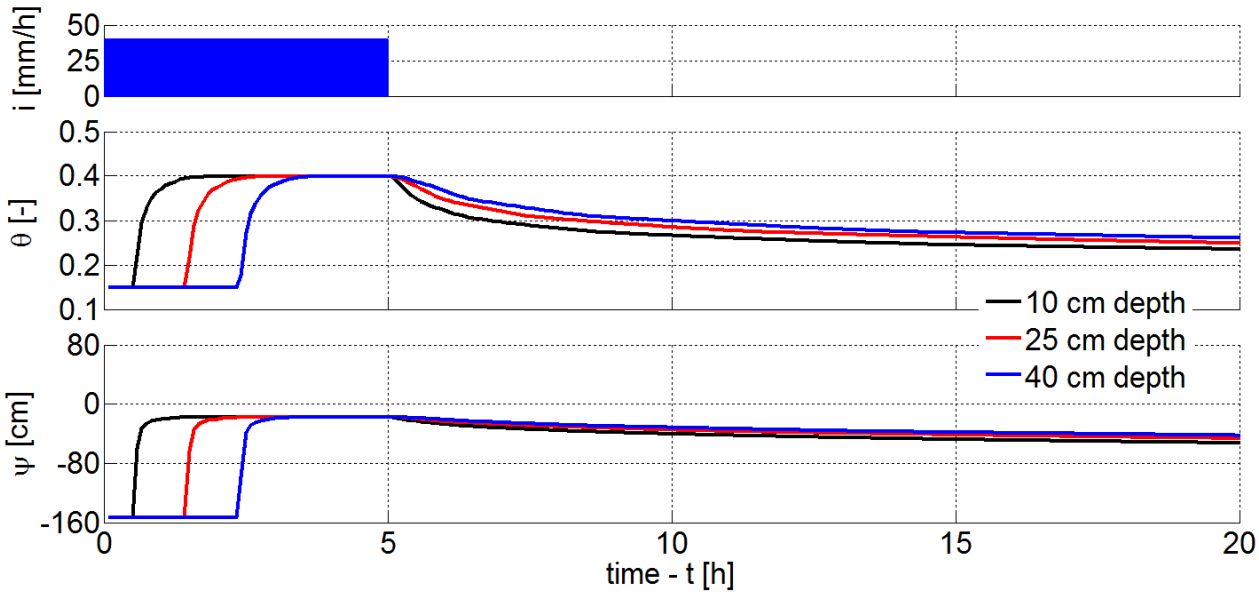

Figure 3-5. Time series of volumetric water content θ (middle) and pressure head ψ (bottom) in a soil column of 56 cm subject to the rainfall event represented in the top panel.

3.2.3 Experimental procedure and assumptions

Based on the previous theoretical considerations, the experimental procedure can be carried out by applying a sequence of gradually increasing rainfall rates until a maximum value coinciding with saturation of the sample is reached. Each of these rates lasts long enough for the soil to reach steady-state, a condition that is then maintained for at least half an hour. The corresponding water content represents an intermediate step between dryness and complete saturation and provides one record for the calibration curve. The mean porosity n is not known a priori, but can be identified at the end of the experiment once the sample is completely saturated, by re-arranging equation (3):

$$n = \frac{1-P_{tot}/(V\gamma_s)}{1-\gamma_w/\gamma_s}.$$

Once the porosity is obtained, the average water content θ_{mean} can be calculated for each rainfall rate by applying equation (3).

The calibration of the WCRs is not conducted for every single sensor, but it is carried out by employing data from all the sensors to define an average calibration curve. This assumption is justified by the technical information provided by the manufacturer, who declares a probe to probe θ variability (± 0.5 % for dry soils and ± 1.5 % for saturated soils) smaller than the single sensor accuracy (± 2.5 %).

The WCR data are linked to the mean water content measured by the weight probe: therefore, the data obtained by the calibrated sensors will refer to a large size domain, greater than the volume surrounding each single probe and equal to the total sample volume (Figure 3-3). Therefore, the influence of local heterogeneity

in the average water content is implicitly accounted for in the calibration curve, while – due to the dimension of the sand box – the heterogeneity on the porous matrix can be reasonably neglected.

To increase the amount of available data, the raw WCR signals and the corresponding values of θ_{mean} are also recorded during the drying cycles, when the signals have stabilized for long enough, even though stead-state is not strictly reached.

The experiments are repeated for three different values of the porosity. The first porosity n_1 corresponds to a loose sand, obtained by placing the soil into the box without any compaction; only a gentle hand-packing is performed to minimize consolidation due to the rearrangement of soil grains in response of the vertical flux. The intermediate porosity n_2 is attained by progressively placing 10 cm-thick soil layers and by packing each layer with a rolling 9 kg metal cylinder (Figure 3-6, left image). The lowest porosity n_3 is obtained by progressively compacting 5 cm-thick layers with a 9 kg cylinder falling from a height of 1.5 m on a metal sheet located on top of the layer (Figure 3-6, right image).

Figure 3-6. Preparation of the intermediate porosity (left) and low porosity (right) soil samples.

Additional tests are conducted with a slightly different apparatus to confirm the previous analyses and to improve the goodness of fit of the calibration curve. The soil is uniformly placed in a large box with size $50 \times 50 \times 40\,\mathrm{cm}^3$ (Figure 3-7). Six WCR probes are inserted into the soil sample: the bottom is impermeable, differently from the previous tests, and two conditions only are investigated: the initial soil moisture state and the fully saturated condition, reached by adding water to the soil sample. Four tests are performed with this device, again with different porosities.

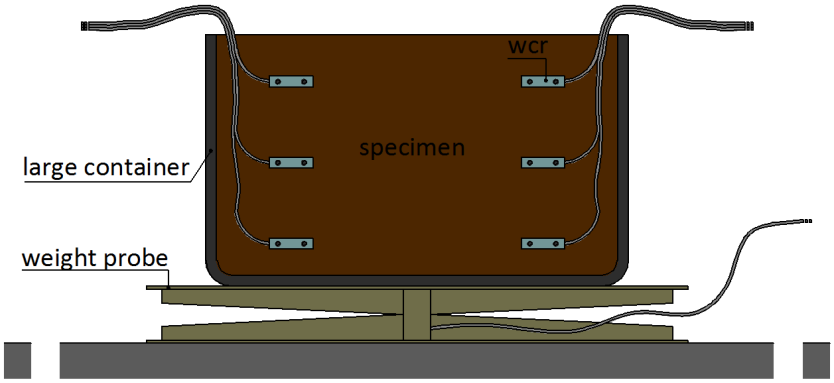

Figure 3-7. Experimental device for the additional tests, limited to two soil moisture values (initial and saturated).

3.3 RESULTS AND DISCUSSION

The data resulting from the three tests performed with the experimental device shown in Figure 3-3 are reported in Figure 3-8 and Figure 3-9, in terms of soil water mass and WCR and tensiometer signals, respectively. The estimated porosity values for the samples are $n_1 = 0.585$, $n_2 = 0.506$, and $n_3 = 0.464$. These values are relatively high, due to the elevated uniformity of the grain size distribution. Due to the fact that the rainfall rate causing saturation is not known a priori, for the experiment with porosity $n_2 = 0.506$ (Figure 3-8-b and Figure 3-9-b), after the third rainfall rate, which saturates the sample, other three smaller rainfall rates are applied in order to increase the number of data collected with intermediate intensities. The 10 cm depth tensiometer signal of Figure 3-9-c shows an anomalous behavior at the third rainfall event, caused by an incomplete adherence of the sensor cup with the soil. This inconvenience was then corrected for the subsequent rainfall rates.

The dataset used for the WCR calibration is reported in Table 3-1. Data from the wetting cycle, i.e., steady state during rainfall, are separated from those collected in the drying cycle, i.e., during soil drainage. Data from the third experiment ($n_3 = 0.464$) with $i = 50$ mm/h was not used for the calibration, as steady state was not reached. The impact of compaction on the soil infiltration capacity is evidenced by the rainfall rate causing saturation, which reduces from around 800 mm/h for $n_1 = 0.585$ to approximately 30 mm/h for $n_3 = 0.464$.

The calibration curves, calculated for each experiment (i.e., porosity) by means of a least square regression, are reported in Table 3-2 and show that the relationship between the raw WCR signal t and the water content is linear. The graphical representation of the curves (Figure 3-10) suggests that the $t - \theta$ relationship is dependent on the average porosity of the soil sample, whereas the most common petrophysical laws for both TDR (Topp et al., 1980) and WCR (Bilskie, 1997) do not admit any dependence of the apparent dielectric number and wave period, respectively, on the porosity.

In order to confirm such dependence on the soil porosity and to find a general calibration relationship as a function of both t and n, additional tests were performed with the experimental apparatus of Figure 3-7. In this case only two data points for each experiment are available, one for the initial water content and one for saturation conditions. However, in light of the previous data, which demonstrated the linearity of the $t - \theta$ relationship, this is not a significant limitation. The experiments were carried out for four degrees of compaction and the resulting data are reported in Table 3-3.

All the collected data, both from the first and second series of experiments, are reported in Figure 3-10, together with the fitting lines derived by least square regressions. The offset between the lines seems related to the variations of porosity, while differences in slope values are limited and seemingly not dependent on porosity. Moreover, the comparison between the calibration law suggested by the manufacturer (also reported

in Figure 3-10) and the experimental data points out the considerable underestimation of the volumetric water content by the latter, despite a certain agreement on the average slope.

The fitting of the whole dataset with a two-dimensional linear relationship accounting also for the porosity returns the following expression:

$$\theta = -0.5487 + 0.02959t + 0.454n \pm 0.0149, \quad \textbf{(4)}$$

which is characterized by a very good fit (Table 3-4).The last term of the equation is the square root of the residual variance. As expected, equation (4) shows that, at the same t, water content increases with porosity.

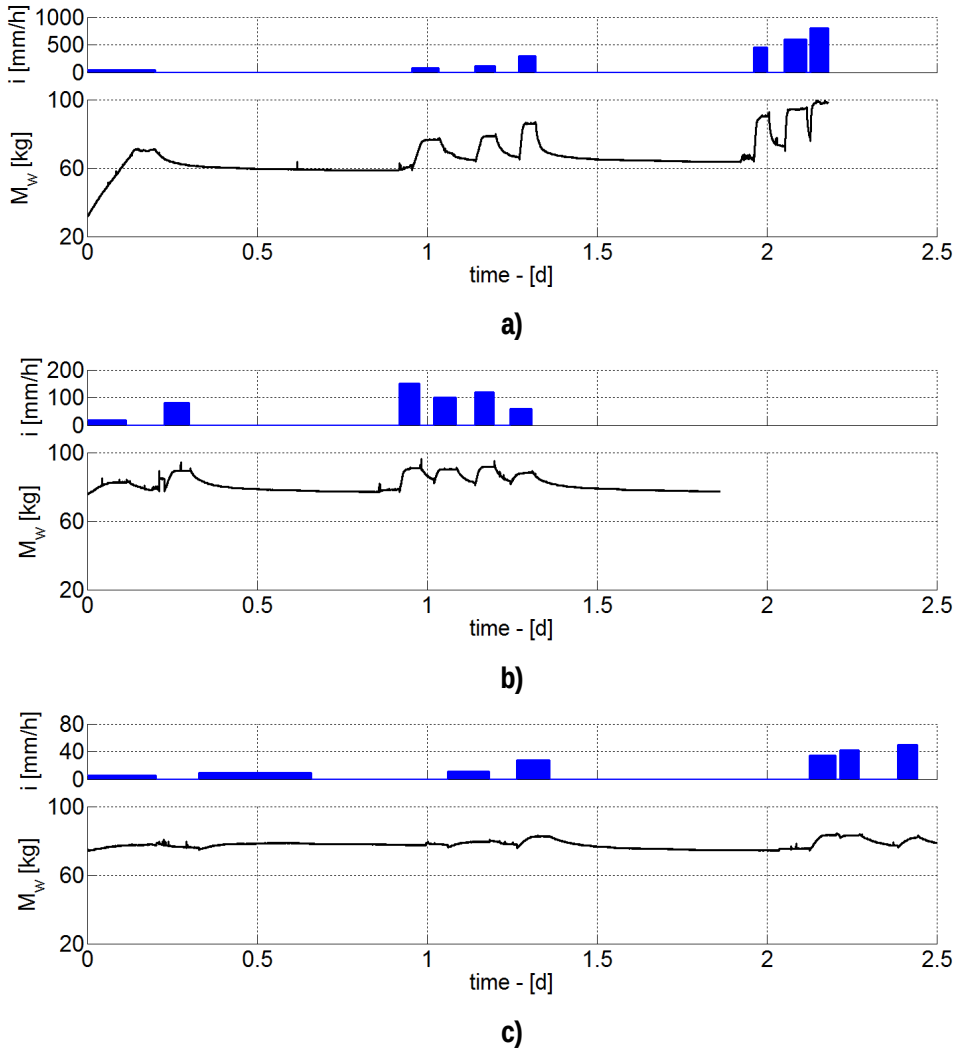

Figure 3-8. Time series of rainfall rate and water mass as recorded by the weight probe for porosities of a) $n_1 = 0.585$, b) $n_2 = 0.506$, and c) $n_3 = 0.464$.

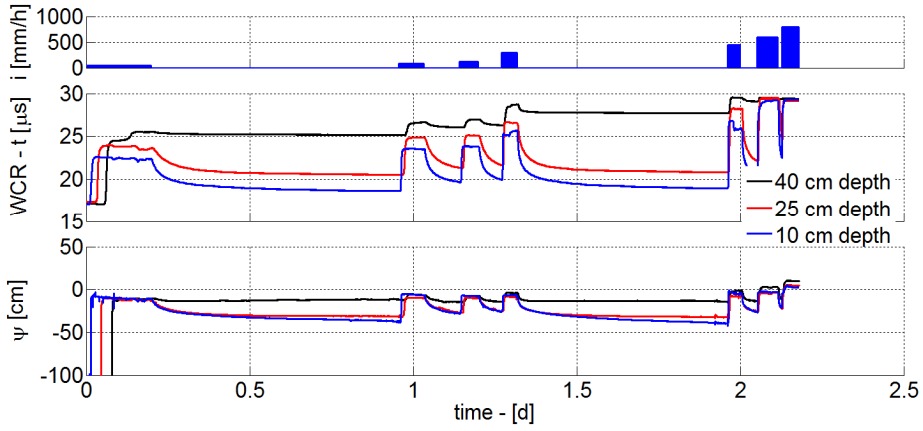

a)

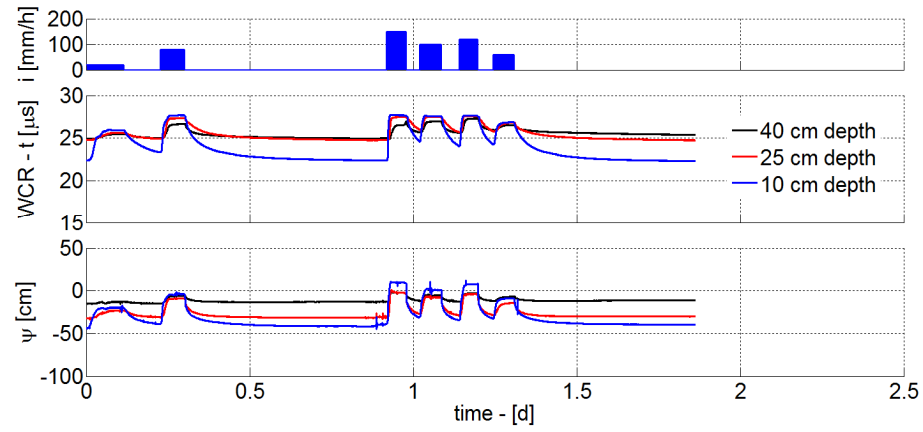

b)

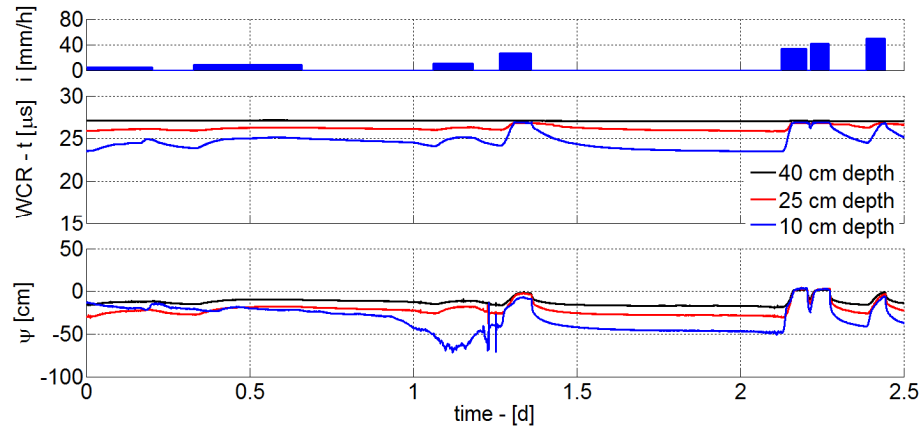

c)

Figure 3-9. Time series of rainfall rate, raw data t from the WCRs, and; water pressure head from the tensiometers for porosities a) $n_1 = 0.585$, b) $n_2 = 0.506$, and c) $n_3 = 0.464$.

Table 3-1. Summary of the data collected during the experiments with the device shown in Figure 3-3. The values for "wetting cycle" and "drying cycle" refer to steady-state reached during infiltration and quasi-steady-state reached during drainage, respectively.

FIRST TEST – n1=0.585						
	wetting cycle			drying cycle		
i [mm/h]	θmean	t [μs]	h [cm]	θmean	t [μs]	h [cm]
40	0.423	23.84	-11.24	0.187	17.19	-153.53
80	0.456	24.99	-7.91	0.359	21.43	-26.78
120	0.468	25.31	-8.54	0.378	22.35	-23.07
300	0.511	27.02	-6.49	0.387	22.64	-21.82
450	0.537	27.85	-4.84	0.380	22.50	-28.73
600	0.564	29.30	-1.27	0.416	23.88	-21.89
800	0.583	29.27	5.36	0.450	25.56	-18.27
SECOND TEST – n2=0.506						
	wetting cycle			drying cycle		
i [mm/h]	θmean	t [μs]	h [cm]	θmean	t [μs]	h [cm]
18	0.458	25.68	-18.61	0.424	24.01	-30.13
80	0.497	27.24	-6.06	0.430	24.43	-28.18
150	0.505	27.36	0.80	0.427	24.12	-27.49
100	0.501	27.32	-3.95	0.457	25.42	-23.38
120	0.508	27.48	-0.85	0.458	25.12	-25.09
60	0.490	26.75	-10.02	0.454	25.32	-24.21
THIRD TEST – n3=0.464						
	wetting cycle			drying cycle		
i [mm/h]	θmean	t [μs]	h [cm]	θmean	t [μs]	h [cm]
5	0.430	26.05	-16.12	0.419	25.54	-19.29
9	0.4360	26.155	-16.90	0.416	25.65	-21.07
11	0.440	26.19	-27.45	0.423	25.76	-30.23
27	0.458	26.95	-6.250	0.423	25.77	-27.51
34	0.462	26.93	2.94	0.412	25.49	-32.01
42	0.462	26.92	2.48	0.454	26.68	-15.72
50 – not complete	0.455	26.85	-3.32	0.423	25.95	-27.66

n: porosity;i $[mm/h]$: rainfall rate;θ_{mean}: volumetric water content;t $[\mu s]$: average wave period measured by the three WCR sensors; h $[cm]$: average of the water pressure heads measured by the three piezometers

Table 3-2. Calibration curves of the WCR sensors obtained by fitting the data reported in Table 3-1. The last term in each equation is the square root of the residual variance.

	calibration curve for the WCR sensors	95 % confidence interval of law coefficients θ=at+b	
n1=0.585	θ=0.03047t-0.3112 ± 0.0126	a (0.02816; 0.03278)	b (-0.3682; -0.2541)
n2=0.506	θ=0.02371t-0.1456 ± 0.0036	a (0.0219; 0.02552)	b (-0.1924; -0.09876)
n3=0.464	θ=0.03256t-0.4166 ± 0.0029	a (0.02949; 0.0357)	b (-0.4989; -0.3342)

n: porosity;θ: the volumetric water content;t $[\mu s]$: average wave period measured by the three WCR sensors

Table 3-3. Volumetric water content deduced from the weight probe and average of the raw data from the six WCR sensors collected from the experiments performed with the device of Figure 3-7.

	n=0.612		n=0.535		n=0.502		n=0.459	
	θ	t [μs]	θ	t [μs]	θ	t [μs]	θ	t [μs]
initial condition	0.292	18.41	0.336	21.74	0.339	22.44	0.330	24.41
saturated condition	0.612	28.59	0.535	29.31	0.502	28.74	0.459	27.27

n: porosity;θ: the volumetric water content;t $[\mu s]$: average wave period measured by the three WCR sensors

Table 3-4. Calibration curve obtained by fitting the experimental data shown in Figure 3-10 and goodness of fit statistics.

method of data approximation	Least Squares
fitting law	θ=-0.5487+0.02959t+0.454n±0.0149
95 % confidence interval of law coefficients - θ=a+bt+cn	
a	(-0.5845;-0.5128)
b	(0.02871;0.03047)
c	(0.4119;0.469)
goodness of fit	
SSE=0.002324	summed square of residuals
R-square=0.9909	square of the multiple correlation coefficient
RMSE=0.007186	root mean square error

n: porosity;θ: the volumetric water content;t $[\mu s]$: average wave period measured by the three WCR sensors

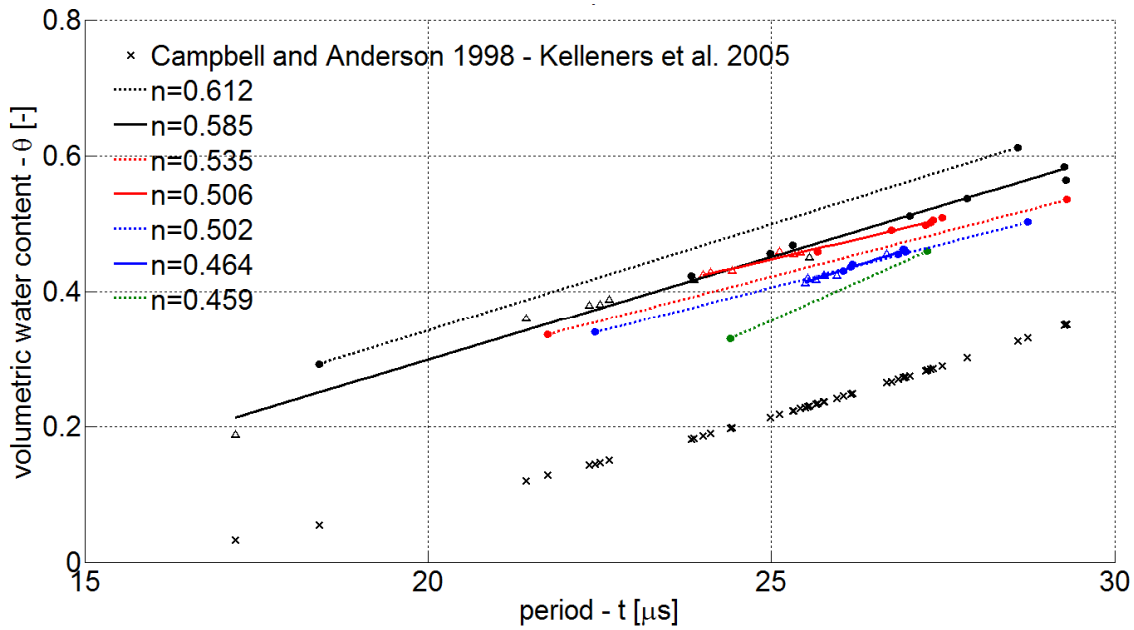

Figure 3-10. Experimental data from the tests conducted with the devices shown in Figure 3-3and Figure 3-7. Solid lines fit the data from the first experimental device (Figure 3-3), while dashed lines fit the data from the second experimental device (Figure 3-7). Symbols x represent data interpreted with the calibration curve provided by the manufacturer of the WCR sensors (Campbell and Anderson, 1998; Campbell Scientific, 2003; Hansson and Lundin, 2006; Kelleners et al., 2005).

4 RAINFALL-TRIGGERED SHALLOW LANDSLIDES: INFILTRATION DYNAMICS IN A PHYSICAL HILLSLOPE MODEL

4.1 INTRODUCTION

Landslides induced by high-intensity rainfall infiltration in hillslopes are complex phenomena that involve hydrological processes operating at different time scales. The models usually adopted to predict susceptible areas are typically calibrated over large areas at the basin scale, with limited soil information and without an in-depth understanding of the involved hydrological processes at the local scale. Moreover, the stability analysis is usually conducted by means of the safety factor, which application for predicting real landslides is too simplistic.

We challenge this issue through the analysis of physical experiments performed in an artificial hillslope (Figure 4-1). In order to analyze and examine the factors leading to the failure and the triggering modes, the hillslope is equipped with sensors to monitor the pore water pressure and moisture content response to rainfall in a 60 cm thick sand layer overlying a sandy clay soil.

A numerical model was then adopted to simulate the experimental data by solving the Richards equation. The numerical model was parameterized by means of measurements of the soil retention properties from data obtained with the large scale experiment described in Section 3.2.1.

4.2 MATERIAL AND METHODS

4.2.1 Landslide model

The device used to simulate shallow landslides consists of a reinforced concrete box 6 m long and 2 m wide; the height varies linearly from 3.5 m to 0.5 m, such that a sloping angle of 32° can be assigned to the soil (Figure 4-1). On each lateral side of the box, 50 openings closed with screw caps allow the insertion of monitoring probes in properly chosen positions. The slope toe consists of a porous wall made of hollow bricks, allowing water to drain from the subsurface.

Topsoil can be arranged inside the model to reproduce a typical geometry of slopes susceptible to landslide, i.e. a shallow permeable soil layer overlying a less permeable basement (Figure 4-1). To minimize three-dimensional effects, the top layer is designed to form a planar surface with a constant thickness equal at 60 cm.

A silty fine sand with a high uniformity coefficient (see Section 3.2.1) was chosen (Figure 3-1) for the top layer, while the basement is formed by a sandy clay soil (plasticity index I_P = 8%). During heavy rainfall, the failure is expected to involve only the sandy layer because of its high hydraulic conductivity and cohesionless nature; the underlying soil is not likely to be involved in the collapse, even though it played a role in the hydrologic process, by absorbing water when the rain-induced infiltration front reaches the interface of the two soils (see Section 4.3.3).

Six pairs of tensiometers and water content reflectometer (WCR) probes were used to continuously measure and record the pore water pressure head and water content in the topsoil. The tensiometers were arranged in the soil by means of the openings in the lateral walls (Figure 4-3): before the installation, a hole was created for each tensiometer using a hollow tube. Afterwards, the tensiometers were inserted into the holes such that their porous cups were completely attached to the soil. The wall openings were then sealed with silicon to avoid water losses during the experiments. The WCR probes were entirely inserted into the soil, ensuring their rods are totally covered by the sand.

To arrange the observations in a convenient 1-D schematization, the sensors were located in an intermediate position (Figure 4-5) of the landslide model. The longitudinal section of Figure 4-1 shows the 6 positions indicating the installation of each tensiometer in front of the corresponding WCR. The instrument positions were far enough from both the slope toe and top, such as the influence of the boundary conditions in the pore water evolution were minimized. In this way, the recorded measurements can be compared with the infinite slope similarity. Furthermore, the data from the three vertical transects provided replicates for the 1-D schematization, which is acceptable when the soil properties are homogeneous in space.

Two V-notch stream gauges (Figure 4-2) were located at the slope toe to collect the surface runoff and the subsurface flow, respectively. All data were collected and recorded by an acquisition system (Figure 4-4) from Campbell Scientific (CR 1000) with a frequency of 0.5 Hz.

The rain input is produced by a rainfall simulator installed on the roof supports of the landslide model (Figure 4-1). It consists of a 1" diameter pipe network equipped with nozzles pointing upwards, and able to realize a steady rainfall intensity ranging from 50 to 150 mm/h. As our main goal is to investigate the role of the hydrological processes in landslide triggering, the nozzles (from Spraying System, www.spray.com) were selected to produce water drops smaller than the typical raindrop, in order to avoid surface splash erosion. In this way the experiments provided information about the evolution of the soil during rain-induced infiltration excluding other external factors such as splash erosion, which could compromise achieving our objectives. The rainfall intensity produced at the soil surface can be changed by controlling either the number of active nozzles or the functioning pressure by means of a global valve. The uniformity of the simulated rainfall has been estimated higher than 85 % for the chosen nozzle configurations as a results of several experimental investigations by means of rain gauges distributed on the rained area.

The landslide tests were performed by applying a steady rainfall intensity equal to 150 mm/h until the mobilization of the soil. By varying the initial porosity of the sandy soil two experiments were carried out. In the first case, high porosity was attained by depositing the soil with a small excavator and leveling it without otherwise touching its surface; in the second case, well-compacted soil was obtained by progressively compacting soil layers of 20 cm parallel to the clay bed.

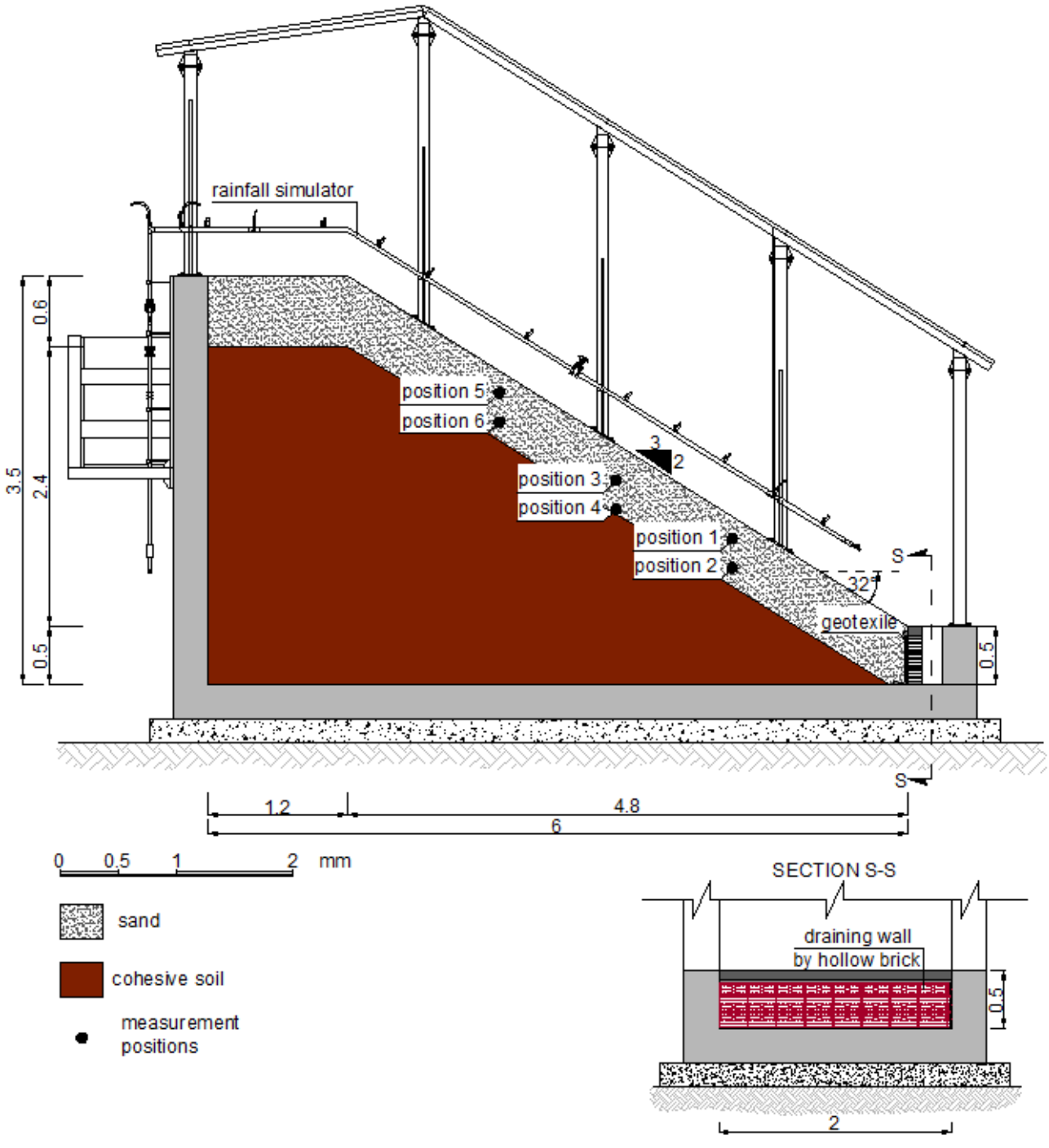

Figure 4-1. Longitudinal section of the landslide model and transversal section of the slope toe

Figure 4-2. V-notch gauge located at the slope toe

Figure 4-3. A view on lateral side of the hillslope model: tensiometers are arranged in the top soil by means of the holes applied in the walls.

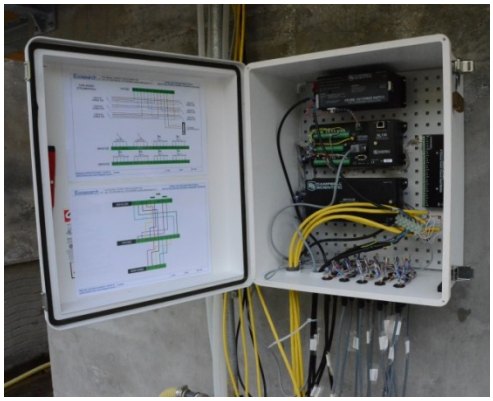

Figure 4-4. Acquisition system for acquiring and recording the output signals from the measuring network

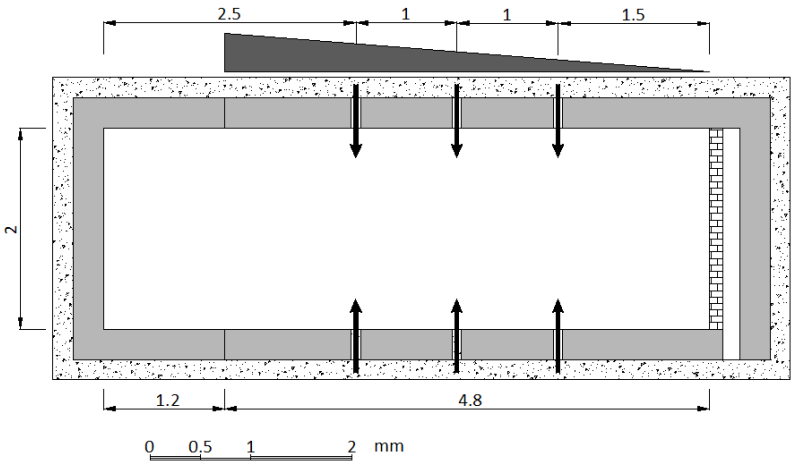

Figure 4-5. Positions of the sensors in a plan view of the landslide model.

4.2.2 Soil characterization

The characterization of the soil was carried out by means of direct shear tests, hydraulic conductivity tests, and water retention tests.

The shear tests were useful to estimate the mechanical parameters of the soil under shear deformation, as well as the porosity range discriminating the hardening behavior from the softening behavior under shear deformation, i.e., the critical porosity. Shear test results helped to interpret correctly the mechanical response of the soil during the landslide mechanism, which was basically assumed as a shear displacement.

The direct shear tests were performed by imposing a shear rupture within a sand sample in a little box, with a circular base area of $36\ cm^2$ and height of $36.5\ mm$ high. The top half of the sample was fixed and the base was moved with a displacement velocity ranging between $600\ \mu m/min$ and $800\ \mu m/min$, until a final displacement of $8\ mm$ was reached in $13\ min$ or $10\ min$, respectively. The vertical effective pressure applied during the shear deformation varied between 10 and $20\ kPa$, consistent with the maximum vertical load in the landslide model for the sand. The tests were conducted on a completely dry soil, previously dried at $105\ °C$.

The conductivity tests were performed for both the silty sand and the sandy clay. In the former case we used a $7.39\ cm$-diameter and $27.15\ cm$-high soil core. Water was supplied from the bottom, imposing an upwards saturating flux. When the flux reached the top, a porous cap allowed the water to exit. By measuring the outflow rate the hydraulic conductivity under saturated condition was inferred. For the sandy clay soil, the estimation was obtained with an oedometer test by ensuring a water flux moving upwards, generated by an unsteady hydraulic head.

For the silty sand, the shear tests and the conductivity tests were carried out for different values of porosity.

The retention tests aimed at detecting the behavior of both the water pressure head and the hydraulic conductivity under partially saturated conditions. The used device (Figure 3-3, hereafter called “retention model”) is described at the Section 3.2.1: it was exploited to calibrate the WCR probes and, concurrently, to derive the retention curves of the soil. Its main properties satisfy the following requirements: i) to assign to the sample a large size representative of soil in field conditions; ii) to reproduce the field process, i.e., rain-induced infiltration; and iii) to ensure an adequate monitoring of the sample hydrologic state.

The data collected for the WCR calibration were used to derive the retention properties of the soil, after turning the raw signals from WCRs (Table 3-1) in water content data.

The collected data give spatially distributed information about the soil sample as a whole: the combination of the suction with the water content yielded an estimation of the retention curves characterizing the soil response to rain infiltration at varying rates. A standard least-square fit allowed us to assess the soil retention curves.

From a theoretical perspective, the retention model can be schematized as a vertical column of homogeneous soil, in which the flux is given by the Darcy's law:

$$v = -K(\theta)\frac{\partial h}{\partial z} = -K(\theta)\left(\frac{\partial \psi}{\partial z} - 1\right), \quad \textbf{(5)}$$

where v is the specific discharge [m/s], θ is the volumetric water content [-], $K(\theta)$ is the relative conductivity of the soil sample [m/s], h is the water potential head [m], z is the vertical axis pointing downward [m] and ψ the water pressure head [m]. In homogeneous conditions, the passage of the wetting front increases the water content and reduces the suction ($-\psi$); when steady state is established, the suction is vertically constant along the whole column, such that the vertical velocity v is equal to the hydraulic conductivity $K(\theta)$, according to equation (5). From the knowledge of the applied rainfall rate $i = v$, we could obtain the hydraulic conductivity $K(\theta)$. The corresponding water content values were estimated by averaging the WCR measurements during the steady state condition.

A preliminary simulation by means of the Richards equation solver Hydrus-1D (Šimůnek et al., 2012) confirmed that the process occurred as described above (Figure 3-4).

Furthermore, the adopted procedure enabled to give an estimation of the hydraulic conductivity in saturated conditions as well. The saturation of the sample could be readily proven by the mean suction equal to zero given by the tensiometers.

The experiments were repeated for three different values of the porosity. The first porosity ϕ_1 corresponded to loose sand, obtained by placing the soil into the box without any compaction; only a gentle hand-packing was performed to minimize consolidation due to the rearrangement of soil grains in response of the vertical flux. The intermediate porosity ϕ_2 was attained by progressively placing 10 cm-thick soil layers and by compacting each layer with a rolling 9 kg metal cylinder. The lowest porosity ϕ_3 was obtained by progressively compacting 5 cm-thick layers with a 9 kg cylinder falling from a height of 1.5 m on a metal sheet located on top of the layer.

To assess the porosity, we increased the rainfall rate until the saturation for each sample. In this condition, the three WCR probes measured the average porosity ϕ, which coincided with the volumetric water content θ.

Brooks and Corey (Brooks and Corey, 1964) and van Genuchten (van Genuchten, 1980) models were adopted to fit $\theta - \psi$ data from the retention tests.

In the Brooks and Corey model:

$$\Theta = \left(\frac{h}{h_b}\right)^{-\lambda} \text{ and } K(\Theta) = K_s\Theta^{\frac{2}{\lambda}+l+2} \text{ if } h < h_b, \quad \textbf{(6)}$$

or $\Theta = 1$ and $K(\Theta) = K_s$ if $h \geq h_b$;

where $\Theta = \frac{\theta-\theta_r}{\theta_s-\theta_r}$ is the effective saturation, with θ_r and θ_s the residual and the saturated volumetric water content respectively; h is the water pressure head and $h_b$the bubbling pressure; $K(\Theta)$ and K_s are the

hydraulic conductivity in partially saturated and saturated conditions, respectively; λ and l are shape parameters.

In the van Genuchten model:

$$\Theta = \left[\frac{1}{1+|\alpha h|^n}\right]^m ; K(\Theta) = K_s \Theta^l \left[1 - \left(1 - \Theta^{1/m}\right)^m\right]^2 \quad \textbf{(7)}$$

where α is the inverse of the bubbling pressure, and n and $m = 1 - 1/n$ are shape parameters.

4.2.3 Hydrus 1-D software

To simulate the measurements in the landslide tests, the Richards equation solver HYDRUS 1-D was used. The HYDRUS software is a widely used tool for evaluating water flow and solute transport in soils and to simulate processes such as precipitation, irrigation, infiltration, evaporation, root water uptake (Šimůnek et al., 2012). HYDRUS 1-D may be used to simulate water flow in variably saturated media, assuming either a vertical, horizontal, or generally inclined direction. The Richards equation for a 1-D domain reads (Figure 4-6):

$$\frac{\partial \theta}{\partial t} = \cos^2 \beta \frac{\partial}{\partial z}\left[K(\theta)\left(\frac{\partial \psi}{\partial z} + 1\right)\right] + i$$

where β is the angle between the impermeable base direction and the horizontal. The program uses a mass-lumped linear finite element method to numerically solve the Richards equation for saturated-unsaturated flow. The unsaturated soil hydraulic properties can be described using van Genuchten (1980), Brooks and Corey (1964), modified van Genuchten (Vogel and Cislerovà, 1988), Durner (1994), and Kosugi (1996) analytical model.

HYDRUS also implements a Marquardt-Levenberg type parameter estimation technique (Marquardt, 1963; Šimůnek and Hopmans, 2002; Šimůnek et al., 2012) for inverse estimation of the soil hydraulic parameters. The adopted method consists in minimizing an objective function (Šimůnek et al., 1998) to serve as a measure of the agreement between measured and modeled data; the input values for the sought parameters have to be reasonable prior data not too far from the “optimal” values.

In the present work, an inverse estimation of retention parameters was performed entering as initial input the values obtained from the retention tests. Optimized retention values were obtained using data collected during the landslide tests by the six tensiometers and the six WCR probes. As a result, the improved values allowed us to optimally simulate the evolution of the hydrologic dynamics in the considered domain.

Parameters that were kept fixed in the inverse problem are the porosity ϕ and the saturated hydraulic conductivity K_s, as their previous estimates by means of the retention tests were assumed to be reliable. Moreover, the inverse problem was solved repeatedly taking ϕ and K_s as fitted parameter, without noting significant variation from their initial measured value. On the other hand, some simulations with residual water content θ_r as a free parameter resulted in unusual values for θ_r, such that we took it fixed and equal to a

reasonable value for silty sand (θ_r = 0.05). Further simulations with little deviations of θ_r around 0.05 did not result in significant variations.

The model domain was represented by the two layers of the landslide model, i.e., the silty sand on top of the sandy clay. All the thickness of the top layer (60 cm) was accounted for in the model, but only 60 cm of cohesive soil was accounted for in the basement. Preliminary simulations demonstrated that this thickness was sufficient to reproduce all the effects of the variable-thickness cohesive basement during the two landslide experiments before the failures.

A Neumann boundary condition was imposed at the top, with a flux equal to the rainfall rate, whereas a free drainage condition was prescribed at the bottom.

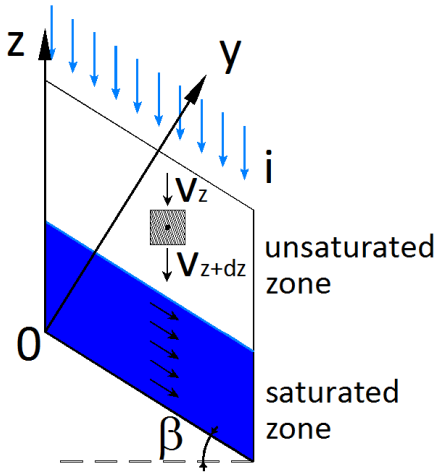

Figure 4-6. Schematic representation of a 1-D domain for Richards' equation.

4.3 RESULTS AND DISCUSION

4.3.1 Direct shear tests

The direct shear tests on sand were conducted for different porosity samples, i.e., $\phi = 0.47 - 0.43 - 0.42 - 0.38$. The corresponding porosities were simply measured by weighting the dried soil sample and from the knowledge of its specific weight.

Figure 4-7 shows the results for increasing values of the vertical load σ', and allow the recognition of the critical porosity range (see Section 4.2.2) for $\phi = 0.47$ (Figure 4-7-a) the sample shear strength increases monotonically approaching the critical value, i.e., the shear strength at constant volume; for $\phi = 0.43$ (Figure 4-7-b) the shear strength increases to a maximum shear resistance, corresponding to the peak resistance, and then decreases approaching the critical value.

The differences between the two porosity values are due to the mutual interlocking evolution of the soil grains. An effective explanation can be given assuming the grains as spherical: when the soil has initially a porosity higher than the critical one, the shear deformation causes a contraction of the soil volume, since the soil grains rearrange in a reduced void ratio configuration. Conversely, densely compacted soils under deformation tends to dilate as the void ratio increases; a large horizontal force is needed to counteract the mutual interlocking of the soil grains, while upon surpassing the peak resistance, the soil contracts and approaches the critical state.

We can assume as the critical porosity a value of $\phi = 0.43$, as for higher values the soil behavior is hardening, otherwise it is softening. At any rate, due to the limited size of the samples, we consider these results only qualitative and useful to recognize the different behavior of the sand under deformation. Moreover they are not reliable to provide an exact value for the critical porosity of the soil in the landslide model having larger size.

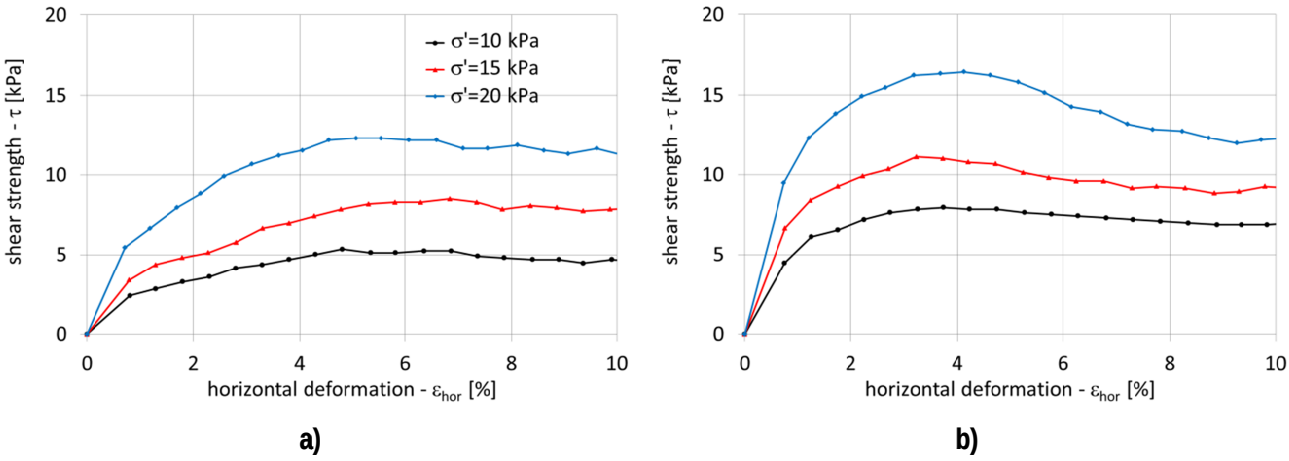

Figure 4-7. Direct shear tests results: the left image (a) shows the behavior of a soil specimen with porosity $\phi = 0.47$ and the right one (b) refers to $\phi = 0.43$. σ' indicates the vertical effective pressure applied to the soil sample during the test.

4.3.2 Retention tests

The retention tests were developed for three different porosities, ϕ_1 = 0.585, ϕ_2 = 0.506, and ϕ_3 = 0.464. These values are much higher than those for the shear test, probably because of the different degree of representativeness related to the size of the samples, i.e., 36 cm^2 × 3.65 cm for the shear tests, instead of 60 × 50 × 60 cm^3 for the retention tests.

The series of rainfall cycles applied during the retention tests are listed in Table 3-1, and the observations from the tensiometers and WCR probes are shown in Figure 4-8. Since the rainfall rate causing saturation was not known a priori, for the experiment with porosity ϕ_2 = 0.506 (Figure 4-8-b), three smaller rainfall rates were applied after the third one causing the saturation. The 10 cm depth tensiometer signal of Figure 4-8-c shows an anomalous behavior at the third rainfall rate, probably caused by an incomplete attachment of the porous cup with the soil. This inconvenience was then corrected for the subsequent rainfall rates.

Table 4-1. Summary of the data collected during the experiments with the device shown in Errore. L'origine riferimento non è stata trovata**.**

FIRST TEST – ϕ=0.585		SECOND TEST – ϕ=0.506		THIRD TEST – ϕ=0.464	
i [mm/h]	θ_{MEAN}	i [mm/h]	θ_{MEAN}	i [mm/h]	θ_{MEAN}
40	0.423	18	0.458	5	0.430
80	0.456	80	0.497	9	0.4360
120	0.468	150	0.505	11	0.440
300	0.511	100	0.501	27	0.458
450	0.537	120	0.505	34	0.462
600	0.564	60	0.490	42	0.462
800	0.583			50 – not complete	0.455

ϕ: porosity; i $[mm/h]$: rainfall intensity; θ_{mean}: volumetric water content

The relationship between the resulting hydraulic conductivity and the water content (Table 3-1) is well-fitted by a power relation (Figure 4-9), consistent with the Brooks and Corey equation (6). The first coefficient of the fitting law represents the hydraulic conductivity in saturated conditions; the results lead to: for ϕ_1 = 0.585, K_s = 827 mm/h; for ϕ_2 = 0.506, K_s = 127 mm/h; for ϕ_3 = 0.464, K_s = 41 mm/h.

Fitting the data with the van Genuchten model, equation (7), yields a significant overestimation of the saturated conductivity found experimentally; therefore, the Brooks and Corey model was preferred for estimating of the saturated hydraulic conductivity.

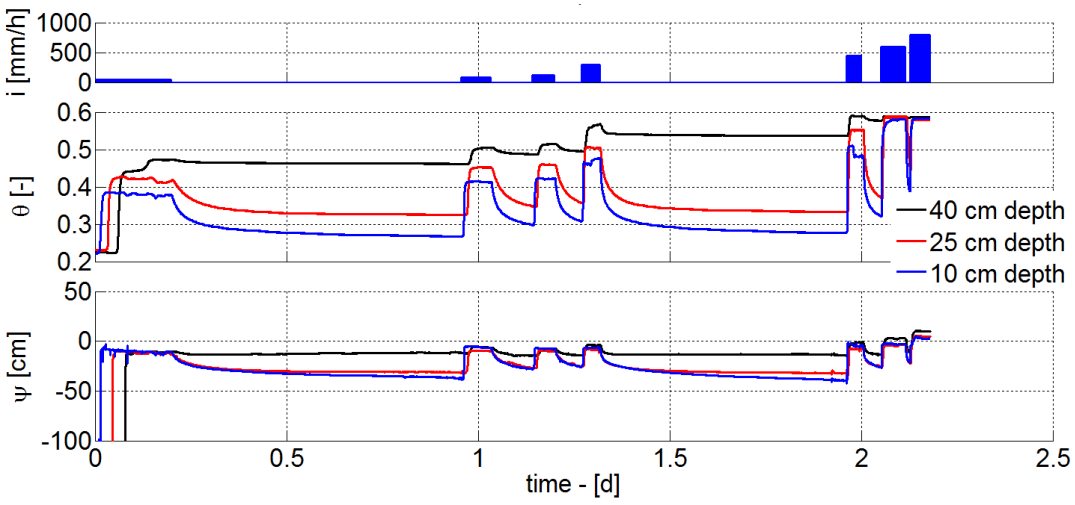

a)

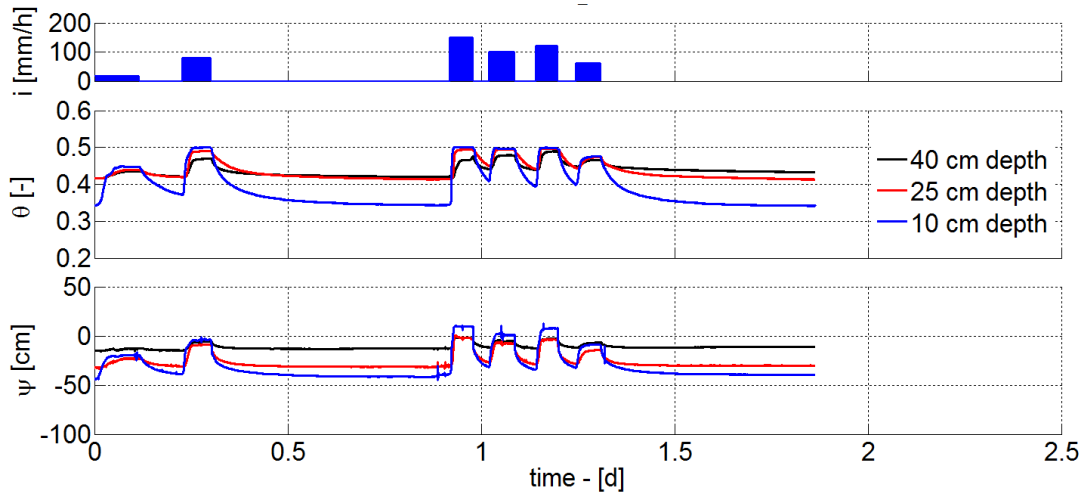

b)

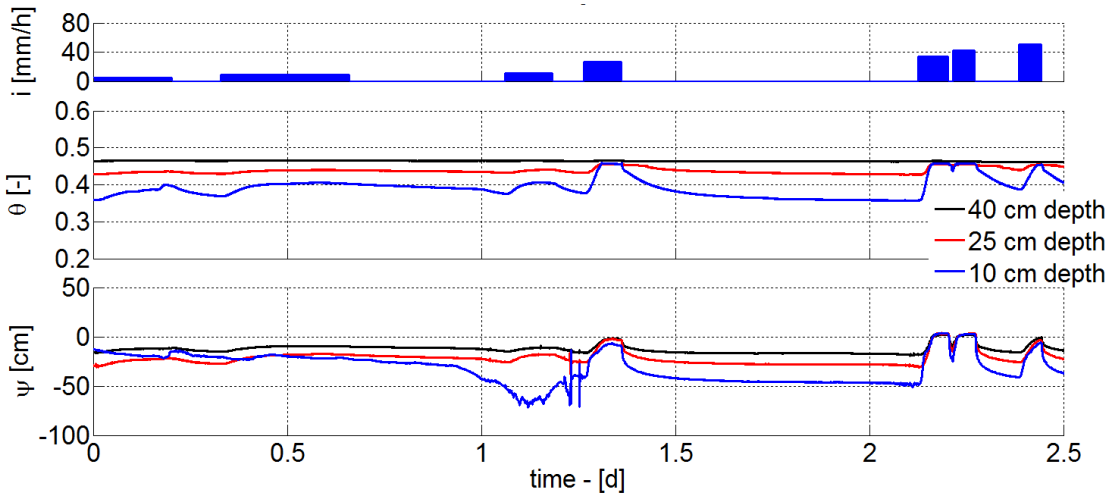

c)

Figure 4-8. Data recorded from three tensiometers and three WCR probes at different elevations during the retention tests (Errore. L'origine riferimento non è stata trovata.**). The three images refer to different values of porosity: a) $\phi = 0.585$; b) $\phi = 0.506$ and c) $\phi = 0.464$.**

1.

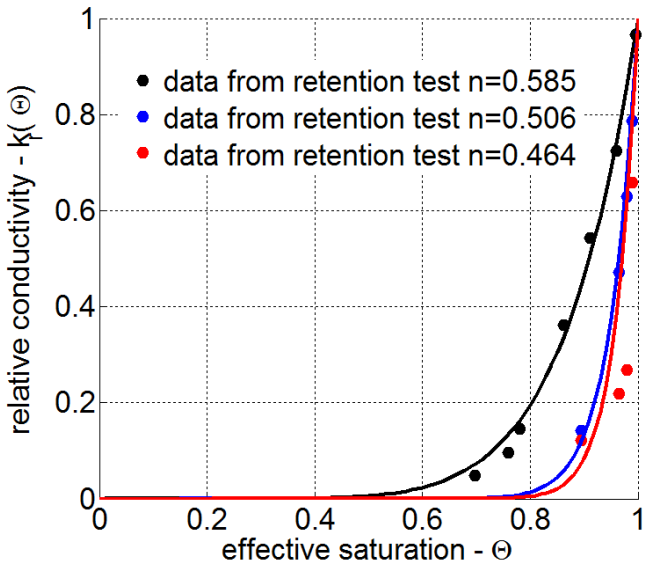

Figure 4-9. Experimental data (dots) obtained from the retention tests; the continuous lines represent the fitting power curves.

A comparison of the conductivity values in saturated conditions as listed before with the analogous results from the permeameter tests (Figure 4-10) shows that the latter overestimate K_s. This may be due to the following reasons: i) the small size of the permeameter may not reproduce the local-scale heterogeneity as in the retention device; ii) the differences in the hydraulic mechanism to generate water flow in the two experiments. In the permeameter a saturated flux is assured with an imposed hydraulic gradient, unlike in the retention test, the gravitational flux occurred by applying a rainfall rate from above; iii) the influence of the lateral boundary of the permeameter cell, causing an increase of the mean water velocity through the transverse section of sand core.

More confidence was then attributed to the results from the retention model, because of the larger size and the similarity of the infiltration processes to the one expected to occur in the landslide model.

The obtained values of saturated conductivity (the red triangles in Figure 4-10) can be fitted with a polynomial law (Figure 4-10) to provide a prediction of K_s as a function of porosity.

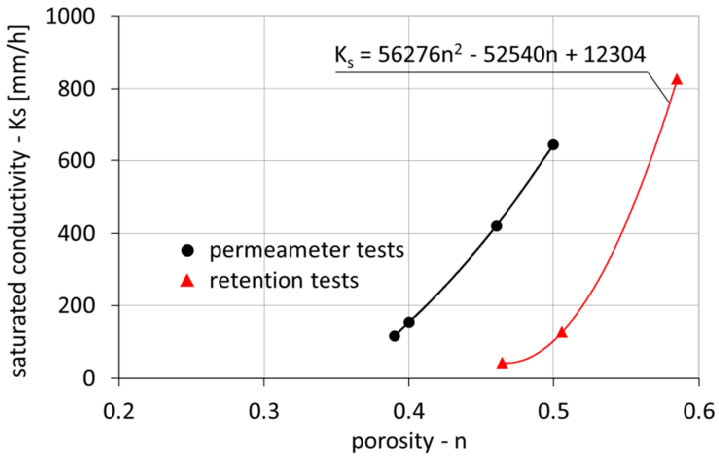

Figure 4-10. Comparison between saturated hydraulic conductivity data obtained from the permeameter and retention tests.

4.3.3 Landslide experiments

The landslide experiments were performed for the soil at different porosities by applying a constant rainfall intensity i = 150 mm/h.

In the first case, the infiltration process evolved for more than 1.5 h until the sand layer failured. At roughly 1.25 h, subsurface flow initiated across the slope toe, consistent with the formation of a water table. The failure occurred suddenly without any warning signs; the sand behavior during the collapse appeared to be smooth and similar to a fluid, with the whole sand surface moving simultaneously downwards. The sand advanced 1 m above the concrete delimiting the slope toe (Figure 4-11 on the left), until the soil surface assumed a sloping angle (about 20°) and the landslide stopped. After the failure, a rapid increase in the subsurface flow was noted to occur.

The failure involved the entire 60 cm sand thickness, as the probes arranged at the interface were found lower than their initial position. The part of sand volume placed horizontally at the top of the model (Figure 4-1) was not mobilized. No surface runoff occurred during the whole experiment.

The experimental data recorded during this first experiment are shown with continuous lines in Figure 4-13. A two-step evolution is noted about the deepest WCR data: the water content initially increases from 0.18 to approximately 0.45, and subsequently it increases again up to 0.578. The first rise involves the probes from the top to the bottom, while the second one progresses from the bottom to the top.

The water pressure data (Figure 4-13-b) shows a delay with respect to the WCR measurements. This delay may be caused by an inertial time needed to reach the hydraulic equilibrium through the ceramic cup, maybe having hydraulic conductivity significantly smaller than that of the loose sand (Watson, 1965).

Nonetheless, the pressure head evolves similarly to the water content In a first step, the wetting front moves downwards and causes a nearly saturated condition. Subsequently, the water pressure increases to positive values and rises linearly.. Then, an immediate peak precedes the failure.

The variability of the measurements from probe to probe seems limited, so that the assumption of soil homogeneity can be justified.

A vertical displacement was observed to involve the cohesive soil basement after a few days the experiment. At the top of the hillslope, the displacement was roughly estimated 40 cm. The most likely reason is the consolidation of the clay layer as a consequence of the infiltration dynamics occurred in the first experiment. To prepare the second experiment, the sand layer was removed, and a volume of sandy clay was added and compacted until the original profile of the basement was obtained. Next, the sand layer was replaced.

The second test lasted slightly more than 2 h, when the sand layer was considered to be collapsed (Figure 4-12).

A consistent surface runoff started developing after some minutes from the beginning of the experiment. The flow gathered in rills and caused a slight erosion of the sand layer, especially at the junction of the sloping part with the horizontal top. Small quantities of soil were transported downwards and deposited at the slope toe. At 1.6 h, some local slips of the top surface occurred episodically, and evolved as fluidized soil flowing down the slope. The phenomenon became significant at 1.75 h, when the amount of flowing soil increased fast due to the mixing with runoff water.

At 1.76 h, the entire mass of sand was seen moving slowly downwards, as a rigid block.

At 2 h, the initial geometry of the sand layer was clearly altered, such that the soil was assumed to be collapsed and the probes were not consistent to the original setup anymore (Figure 4-11 on the right).

The sand transported to the slope toe clogged the transversal streams, compromising the measurements from the stream gauges. In addition, no subsurface outflow was observed during the normal functioning until 1.75 h.

The data are represented with continuous lines in Figure 4-14: the homogeneity assumption is now less acceptable than in the previous case. In particular, the initial conditions differ between the tensiometers installed at the positions 1 and 2 (the two top left graphs in Figure 4-14-b corresponding to position 1 and 2 in Figure 4-1), whose initial suction is much higher than the values recorded by the other probes.

The hydrological dynamics from the WCR observations (Figure 4-14-a) can be synthetized in three steps: a first increase up to $\theta = 0.466$ resulting from the wetting front moving downwards and two following rises, the former to a water content of $\theta = 0.5$, and the latter resulting in a disturbed signal.

The water pressure data (Figure 4-14-a) do not show significant time delays as in the previous case, meaning that the hydraulic conductivity of the ceramic cup is now comparable with that one of the compacted sand. The suction is nearly zero after the first wetting passage (Figure 4-14-b) and then the pressure increases slowly,

reaching the maximum value at approximately $t = 1.78$ h. Subsequently the signal become disturbed, and exhibits some small fluctuations.

Figure 4-11. Images of the sand layer after failure in the two experiments: with loose sand one on the left and dense sand one on the right.

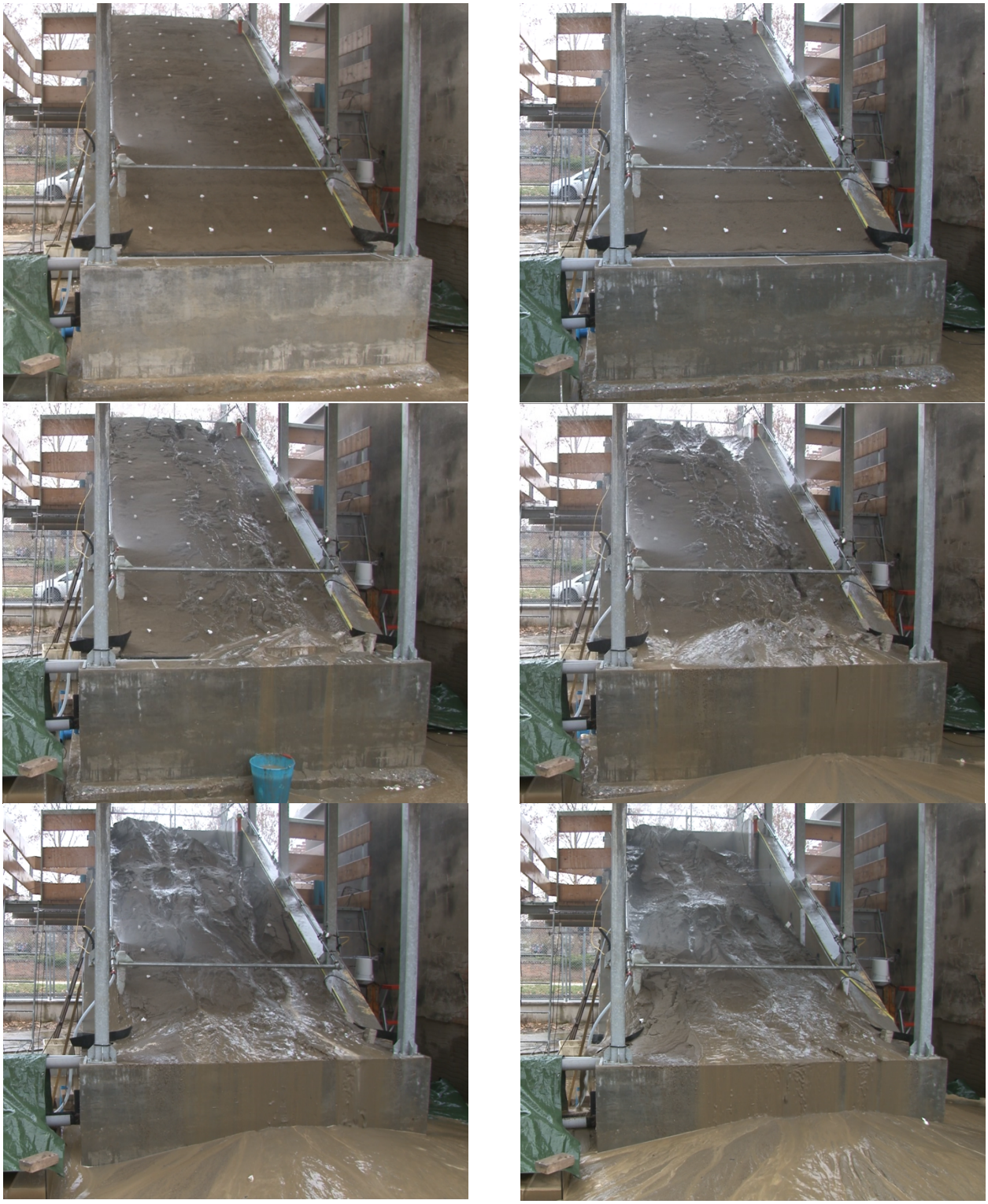

Figure 4-12. Sequence of images at Δt=20 min of the experiment regarding dense sand.

4.3.4 Hydrological modeling

In order to reproduce the two experiments by means of a numerical modeling, it is important to assign correctly the porosity to the sand soil. This is done by observing the WCR data.

In both the experiments, the rain generated a wetting front flowing downwards across the sand layer. In the first experiment, the wetting front did not saturate the sand at its passage and no surface runoff due to infiltration excess (Horton mechanism) occurred. In the second experiment, with dense sand, the passage of the wetting front was expected to saturate the sand, since the infiltration capacity of the soil was exceeded by the rainfall, and the water excess turned into surface runoff.

After this first step, the wetting front reached the interface with the cohesive soil, which represented an unsaturated low-permeability barrier. A small fraction of the infiltrating water was absorbed by the clay layer, and it continues downwards; however, the main contribution stayed in the sand layer. At this time, the dynamics differed significantly between the two cases.

From a theoretical perspective, the continued infiltration determined a perching water table filling the entire pores as it rose in the loose sand. For dense sand the voids were already filled with water and additional infiltration caused the total rain to produce surface runoff, less the small losses in the cohesive soil.

The real water content evolution in the first experiment was consistent with the theory: therefore, the porosity was considered coincident with the average of the steady WCR data after the second rise due to the water table formation (positions $2-4-6$ in Figure 4-13-a), $\phi_{loose} = 0.578$. In the second experiment the detection of the porosity could result uncertain, as the experimental data showed an unexpected second increase of the water content (Figure 4-14-a).

The reason might be related to two distinct phenomena: i) entrapment of air bubbles, which can exit completely only when the water pressure is positive and ii) deformation of the soil matrix as the soil grains rearrange. As a result of these processes, the total porosity would correspond to the second rise of the water content ($\theta = 0.5$). However, our estimation needs to be consistent with the characterization provided by the retention tests, where only a vertical infiltration was applied without water table. Therefore, the chosen value for the initial porosity corresponds to the water content reached after the first step, $\phi_{dense} = 0.466$.

The previously discussed issue is not significant for the loose soil, which has a fairly large porosity and, therefore, limited resistance to air bubble expulsion.

Thus, the porosity values considered to characterize the soil in the two cases are: $\phi_{loose} = 0.578$ for the loose sand and $\phi_{dense} = 0.466$ for the dense sand. These values are close to the first and third porosities found during the retention tests, $\phi_1 = 0.585$ and $\phi_3 = 0.464$, respectively.

The initial estimates of the retention functions for the landslide tests were inferred by fitting the retention tests data. The curves (the continuous and dashed black lines in Figure 4-15 and Figure 4-16) were obtained in accordance to the Brooks and Corey and the van Genuchten models (see Section 4.2.2) .Hysteresis was here neglected, under the assumption that all the other uncertainties (measurement errors, forcing errors, etc.) are more relevant than the effects related to hysteresis.

The saturated hydraulic conductivities in the two experiments are inferred by the polynomial law shown in Figure 4-10 and reported, together with the remaining parameters, in Table 4-2**.**

Table 4-2. Soil parameter values applied to the sand for simulating the two landslide tests with Hydrus 1-D.

Loose sand ϕ = 0.578						
Brooks and Corey model	θ_r	θ_s	K_s [mm/h]	h_b [cm]	λ	l
	0.05	0.578	737	-8.537	0.5865	1.9109
van Genuchten model	θ_r	θ_s	K_s [mm/h]	α [1/cm]	n	l
	0.05	0.578	737	0.059178	1.9534	-1.839
Dense sand ϕ = 0.466						
Brooks and Corey model	θ_r	θ_s	K_s [mm/h]	α [1/cm]	n	l
	0.05	0.466	41	0.018456	2.0366	8.288
van Genuchten model	θ_r	θ_s	K_s [mm/h]	h_b [cm]	λ	l
	0.05	0.466	41	-13.42	0.2355	13.0674

ϕ: porosity; θ_r: residual volumetric water content; θ_r: saturated volumetric water content; K_s: hydraulic conductivity in saturated conditions, h_b: air bubble pressure in the Brooks and Corey model; α: inverse of the air bubble pressure in the van Genuchten model; λ, n and l are shape parameters

The obtained soil characterization (Table 4-2) was used to run the Hydrus 1-D model and to confirm our hypotheses about the hydrological processes occurring during the experiments.

As regards the sandy clay soil of the basement, the only measured parameter was the hydraulic conductivity in saturated conditions (see Section 4.2.2). Other unknown parameters are assigned from the literature (Carsel and Parrish, 1988).

The initial estimates of the parameters reported in Table 4-2 were used as prior data for the inverse modeling procedure described in Section 4.3.4. For the first experiment, only the WCR data were included in the elaboration, as the water pressure data were compromised by the delay effect described earlier. Conversely, in the second landslide experiments, all the data were used for the optimization of the parameters.

The resulting values of the optimized parameters were reported in Table 4-3, while the corresponding model results were shown in Figure 4-13 and in Figure 4-14 (dashed lines).

Table 4-3. Soil parameter values obtained by the inverse method on the two landslide tests.

Loose sand ϕ = 0.578						
Brooks and Corey model	θ_r	θ_s	K_s [mm/h]	h_b [cm]	λ	l
	0.05	0.578	737	-4.805	0.6531	0.1008
van Genuchten model	θ_r	θ_s	K_s [mm/h]	α [1/cm]	n	l
	0.05	0.578	737	0.05066	2.725	0.3935
Dense sand ϕ = 0.466						
Brooks and Corey model	θ_r	θ_s	K_s [mm/h]	α [1/cm]	n	l
	0.05	0.466	41	-11.0791	0.3807	1.475
van Genuchten model	θ_r	θ_s	K_s [mm/h]	h_b [cm]	λ	l
	0.05	0.466	41	0.02734	2.69	3.686

ϕ: porosity; θ_r is the residual volumetric water content; θ_r is the saturated volumetric water content;K_s is the hydraulic conductivity in saturated conditions, h_b is the air bubble pressure in the Brooks and Corey model; α is the inverse of the air bubble pressure in the van Genuchten model; λ, n and l are shape parameters

In the first test (Figure 4-13), the experimental data are well captured by the solution of the Richards equation. The one phase model is then sufficient to reproduce accurately the hydrologic processes until the slope failure in this case. In particular, the Brooks and Corey model appears to approach better the field data than the van Genuchten model, especially in terms of water pressure head (Figure 4-13-b). This is due to the better

description provided by the Brooks and Corey model in wet conditions close to saturation (Figure 4-15-a). In fact, the optimized Brooks and Corey curve (Table 4-3) envelops the highest part of the scattered field data from the retention tests, corresponding to the main wetting curve (Figure 4-15-a). This retention path is highly consistent with the imbibition process of the sand layer during the landslide test.

As regards the second landslide experiment, the numerical solution (Figure 4-14) corresponds adequately to the experimental data only until the development of positive water pressures. Afterwards, the pressure heads in the numerical solution show an instantaneous increase up to the hydrostatic distribution with the water table at the ground surface. The experimental results reveal the water pressure rising much more slow, probably delayed by air bubbling out from the soil and by the soil incipient deformation.

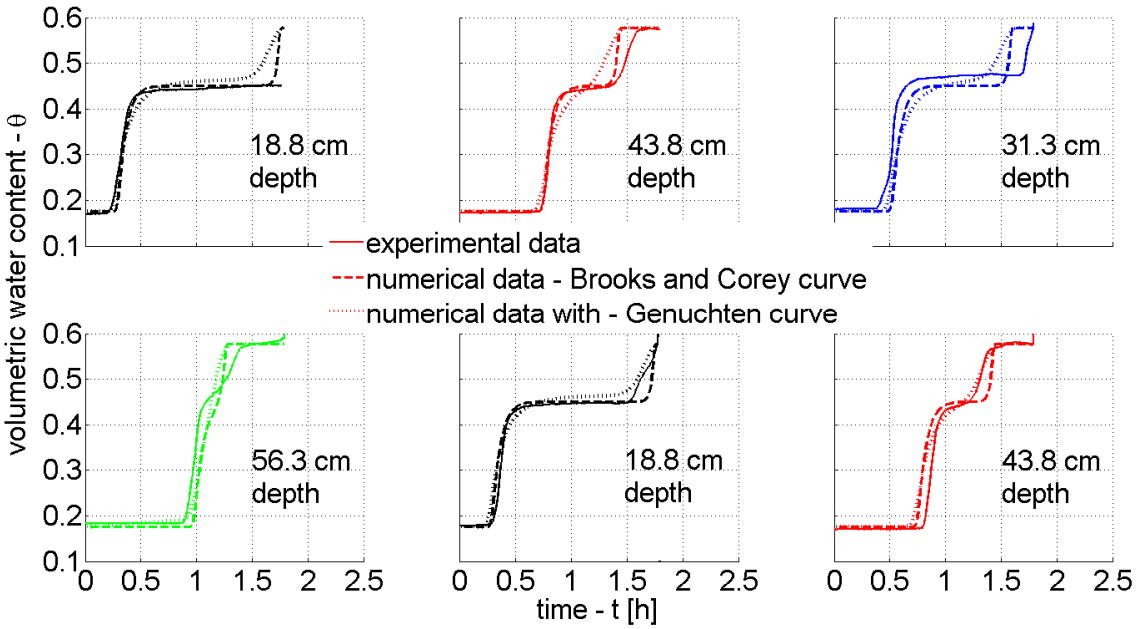

a)

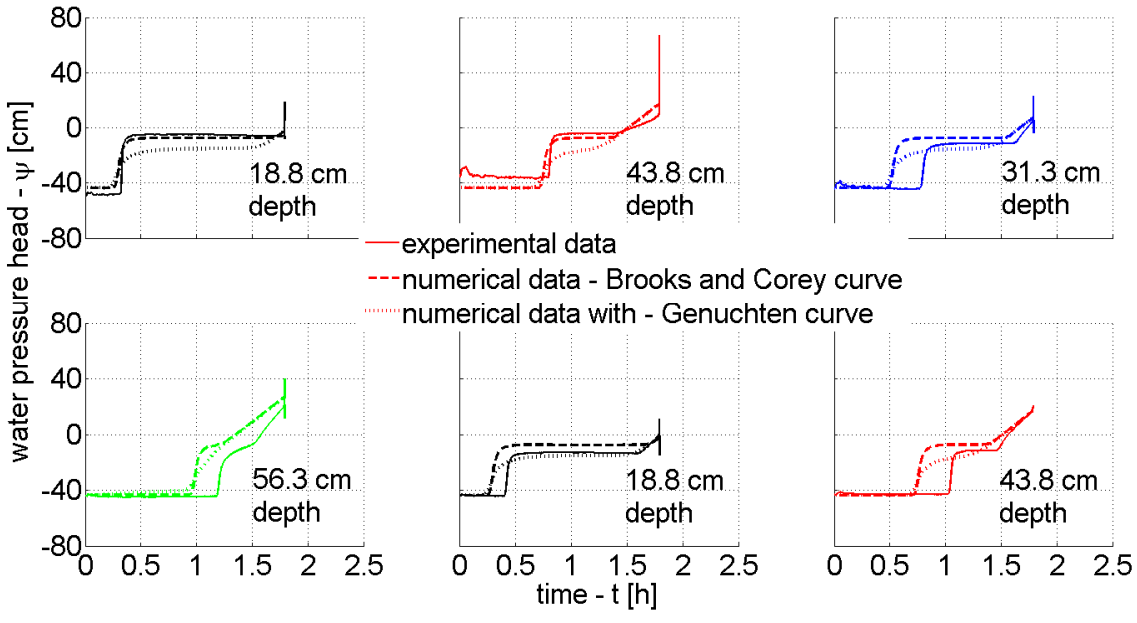

b)

Figure 4-13. Time series of water contentθ(a), and water pressure head ψ (b) at the positions indicated in Figure 4-1 during the first landslide test with porosity $\phi_{loose} = 0.578$: continuous lines represent datafrom WCR probes and the tensiometers during the experiment; the dashed and the dot lines result from numerical simulation with Hydrus 1-D, by adoptinig either the Brooks and Corey model or the van Genuchten model. The first graph on the top left corner refers to the position number 1 in Figure 4-1, and so on to the position number 6 (on the bottom right corner).

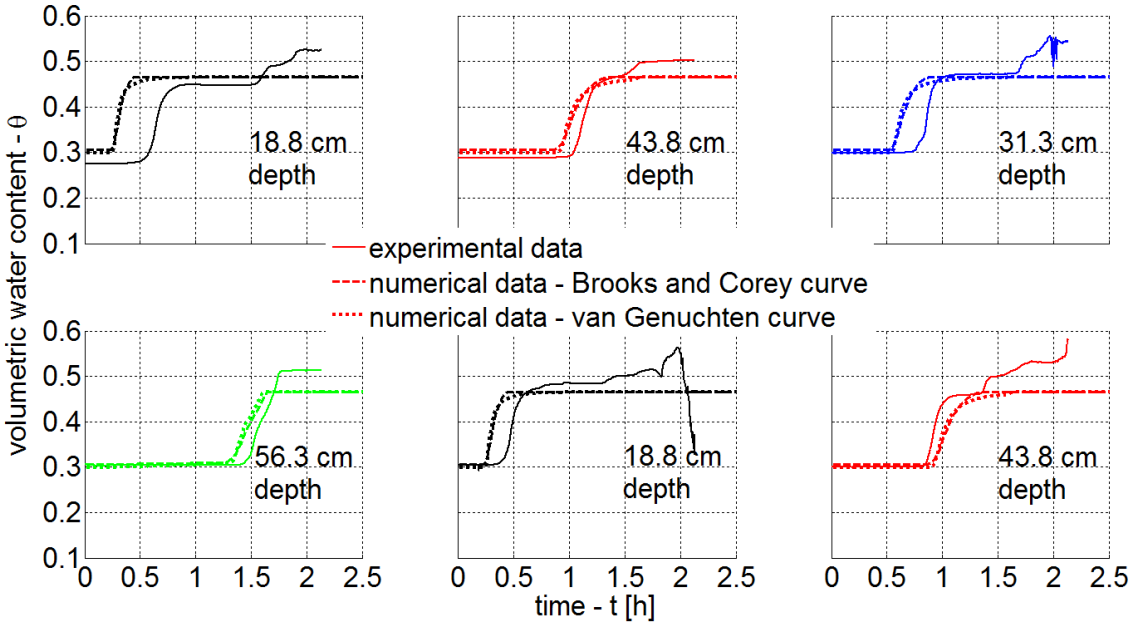

a)

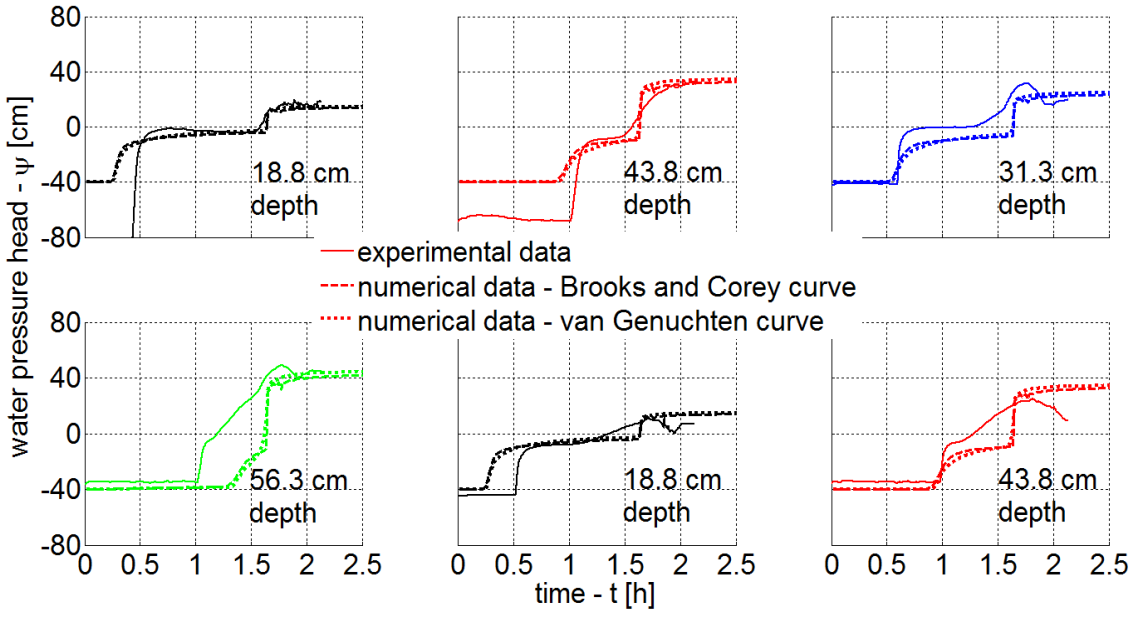

b)

Figure 4-14. Time series of water content θ (a), and water pressure head ψ (b) at the positions indicated in Figure 4-1 during the second landslide test with porosity $\phi_{dense} = 0.466$: continuous lines represent data from WCR probes and the tensiometers during the experiment; the dashed and the dot lines result from numerical simulation with Hydrus 1-D, by adoptinig either the Brooks and Corey model or the van Genuchten model. The first graph on the top left corner refers to the position number 1 in Figure 4-1, and so on to the position number 6 (on the bottom right corner).

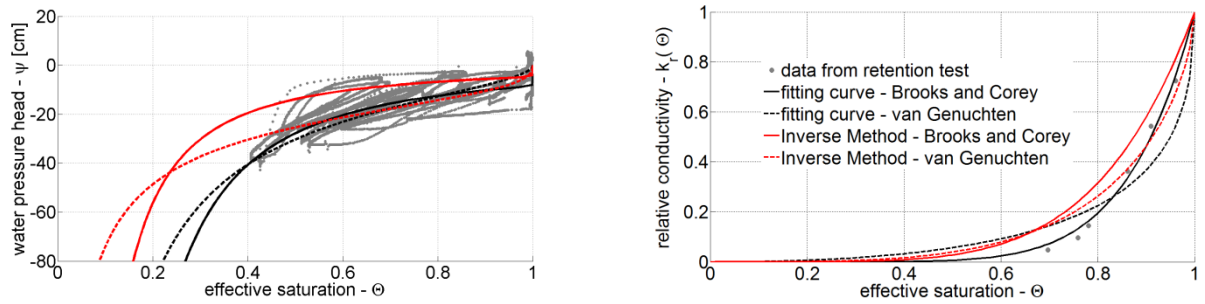

Figure 4-15. Retention curves of loose sand as fitted from the retention test data with $\phi = 0.585$ and obtained from the inverse method applied with measurement data from the first landslide test with $\phi = 0.578$: a) effective saturation as a function of water pressure head; b) relative hydraulic conductivity as a function of effective saturation.

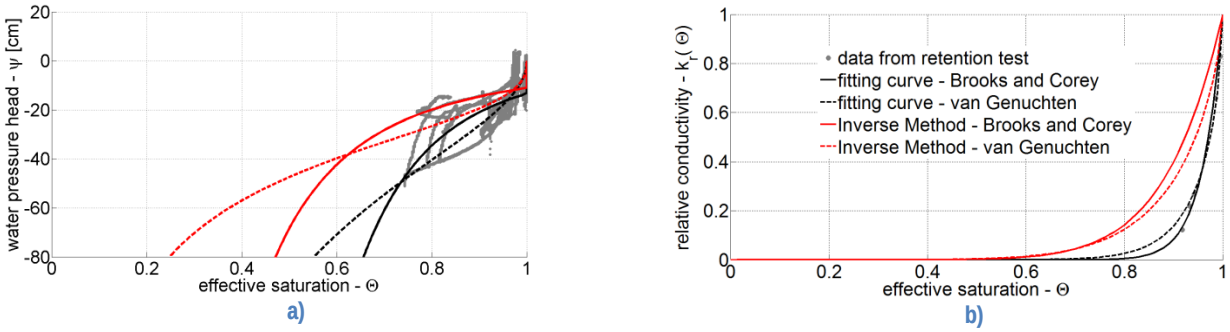

Figure 4-16. Retention curves of dense sand as fitted from the retention test data with $\phi = 0.464$ and obtained from the inverse method applied with measurement data from the second landslide test with $\phi = 0.466$: in a) the relation of the effective saturation with the water pressure head; in b) the relation of the relative conductivity with the effective saturation

4.3.5 Failure triggering factors

In the loose sand, the failure was clearly caused by two consequential factors: i) initially, the seepage forces drove the mechanical instability at the interface, and ii) the consequent shear deformation caused an undrained contraction of the sand soil. A wave pressure developed and involved saturated and previously unsaturated parts in the failure. The time duration of the collapse lasted a few seconds.

In the dense sand the triggering factors worked synergically: i) initially, surface runoff occurred in unsaturated conditions; ii) the soil suction becomes zero as the air exits the soil; as a consequence the shallowest sand layers slipped downward, since the effective stresses were null at the ground surface; iii) when positive water pressure developed, the global stability was violated, and the mobilization of the whole volume started. Since the soil shear deformation was counteracted by the increasing resistance, the failure matured slowly, and sudden failures are excluded.

Figure 4-17 shows the water pressure evolution for the two cases as resulting from the numerical solution of Richards equation. The domain consists of a vertical column composed by the first 60 cm of sand overlying

60 cm of sandy clay. The comparison provides further insights on the hydrological processes preceding the failure in terms of water pressure: the change from negative to positive water pressures is gradual in loose sand and immediate in dense sand. However, in the real field, the last case is probably influenced by interactions of water with the air and soil phases (i.e., air bubbles entrapped and incipient soil deformation) which plays a significant role in slowing down the failure mobilization. Conversely, the Richards equation does not take in account for these factors, since it assumes only the water phase as mobile and rigid soil matrix.

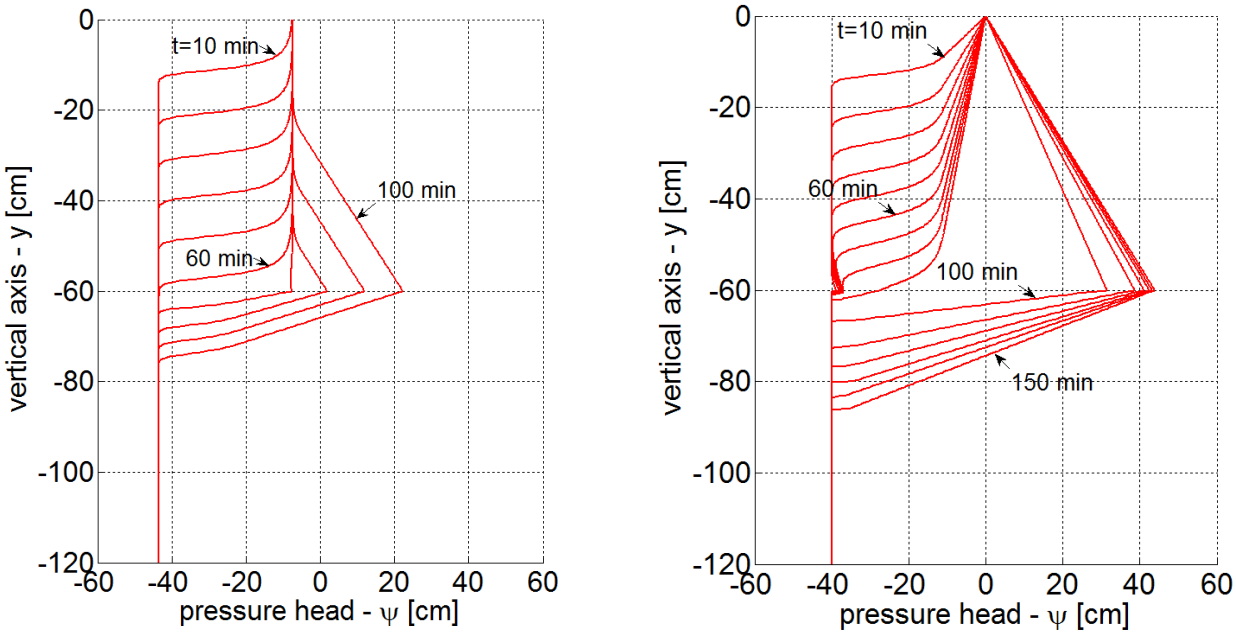

Figure 4-17. Soil water pressure head profiles for time steps Δt=10 min as simulated by Hydrus 1D in a vertical column: on the left for a loose sand (n=0.578) and on the right for a dense sand ($\phi = 0.466$).

4.3.6 Discussion

Our experimental results are consistent with the theory and tests described by Iverson et al. (1997, 2005) (see Section 4.1). Furthermore, the comparison with the numerical results allowed a detailed interpretation of the hydrologic variables evolution as well as an accurate and effective soil characterization.

Some differences with the literature come out about the initial conditions assumed before applying rainfall. In the first case with loose sand, the initial condition recorded for sand was partially unsaturated, constant and without gradient along the vertical. In Iverson (2000), the initial condition assumed for the sandy soil was nearly saturated, obeying to a hydrostatic distribution with the water table placed at the interface with the underlying bedrock. This last assumption justified, in Iverson (2000), to use the only diffusion equation to characterize the water pressure evolution during the rain infiltration until the failure.

Results from the research presented in this work enhance as the complete Richards equation, is needed to explain exhaustively the evolution of hydrological processes leading to the collapse, at least for the first test.

Concerning the second experiment with dense sand, the Richards equation is not able to achieve an accurate reproduction of the observed data. In this case, the factors leading to failure seem affected by the air phase dynamics and the deformation of the soil matrix due to grain rearrangement prior to the total mobilization of the sand layer. These aspects have been neglected in the past literature on shallow landslides induced by heavy rainfall (Iverson et al., 1997; Casadei et al., 2003; Lehmann and Or, 2012; Eichenberger, 2013).

5 CONCLUSIONS

5.1 RAINFALL SIMULATOR

A rainfall simulator was designed and realized for reproducing heavy rainfall intensities between 50 and 150 mm/h. The device consists of a looped pipe network that can accommodate a maximum of 18 nozzles. The experimental investigations considered four configurations, characterized by different numbers and locations of the nozzles, in order to reproduce the desired interval of rainfall intensities. The tests were carried out by varying both the operating pressure and the vertical position of the network, which are the main factors affecting the rainfall rate and distribution. Functional laws were then found for predicting, with a reasonable accuracy, the produced intensity as a function of pressure and nozzle elevation, resulting in a flexible manageability of the simulator for reproducing the desired intensity with a minimum uniformity coefficient over 80 %. The drop size distribution, derived from tests with a single nozzle and different operating conditions, was obtained by capturing the raindrops with petri dishes containing an oil mixture and exposed to the produced rainfall. By combining the drop size distributions with a numerical model able to calculate the trajectories of the drops in 3D we assessed the soil erosion potential associated to the rainfall, in terms of kinetic energy at the impact with the soil surface. Our results highlight a potential erosion similar to natural rains with intensities of around 10 mm/h, confirming that the proposed rainfall simulator can be employed for experimental investigations on an artificial hillslope excluding possible erosion processes and soil crust development that may alter the infiltration process.

5.2 WCR CALIBRATION

An experimental procedure to calibrate Water Content Reflectometer (WCR) sensors is proposed. The original features of the procedure are related to i) the size of the sample, large enough to be representative of the local spatial variability of the soil, which is used in subsequent experiments on a full-scale hillslope model, ii) the experimental device, designed to reproduce infiltration dynamics as similar as possible to those expected to occur in the hillslope model, and iii) the inclusion in the calibration curve of soil porosity, typically neglected in the most popular formulations of TDR and WCR calibration relationships.

The soil sample, much larger than the typical size previously used in the development of TDR and WCR calibration curves, is placed in a box subjected to an assigned infiltration rate at the top and free drainage at the bottom. Pressure head and total weight are carefully monitored by means of three tensiometers and a weight probe, respectively, while three WCR probes provide the raw data for the calibration. Different experiments were carried out by changing the soil porosity and collecting data pairs of water content-wave period at steady-states corresponding to different infiltration rates and subsequent drying.

Our experimental results provide a robust and accurate WCR calibration curve where volumetric water content is expressed as a function of the WCR output (wave period) and soil porosity. The latter has been usually neglected in previous studies carried out on smaller soil samples, while in this application, where WCR probes will be used to monitor soil moisture in large control volumes (approximately 10^{-1} m^3), it can play a significant role.

5.3 LANDSLIDE EXPERIMENTS

Two experiments of shallow landslides triggered by heavy-rainfall were carried out on a monitored artificial hillslope to investigate the hydrological processes leading to failure. The soil considered consists of 60 cm thick layer of fine sand placed over a clay basement with a 60° sloping angle. The horizontal projection occupies a $6\,m \times 2\,m$ surface. The soil was subject to $150\,mm/h$ rainfall until failure. The hydrological state was continuously monitored with six tensiometers and six WCR (Water Content Reflectometer) probes to provide water pressure head and water content, respectively. The two experiments were performed by varying the initial porosity of the soil.

In the first case with initial loose soil, the failure occurred suddenly and was accompanied by a rapid peak of the water pressure. In the second case the soil was densely compacted, and the failure occurred slowly, showing several factors of instability.

To achieve an effective soil characterization, an analysis of the soil retention properties was performed with the device previously used for WCR calibration, consisting of a Plexiglas box ($60 \times 50\,cm^2$ base area and 60 cm high). A series of increasing rainfall rates were applied to three different soil samples with different porosities; the recorded data allowed the definition of the soil retention parameters with both the Brooks and Corey model and the van Genuchten model.

The soil properties were then optimized by running the Richards equation solver Hydrus-1D in inverse modeling mode, using the observations collected during the landslide experiments. The numerical simulation also allowed us to interpret correctly the hydrological dynamics of the soil response to the rainfall input leading to the collapse.

With loose sand, the Richards equation showed a good agreement with the experimental data: the rain input caused a wetting front moving downward and a perched water table formed upon reaching the interface with the clay. When water table exceeded half of the sand layer thickness, the failure started, and the shear deformation produced an undrained slip of soil grains. As a result an immediate wave pressure involved the whole volume in the rapid failure.

With dense sand, the Richards equation did not provide an exhaustive explanation of the hydrological process observed experimentally. The observed data showed a wetting front propagating downward with production of abundant surface runoff. As the front reached the clay layer, the water pressure became positive and the entrapped air starting exiting. The gas phase continuing to exit from the soil while the hydrostatic pressures were increasing. Three factors of instability were noted: i) a first abundant runoff; ii) local detachments of shallow layers when the suction become null and the effective stresses at the ground surface are null; iii) a global downward advancement of the entire sand volume with when the hydrostatic pressure distribution developed.

The comparison between the Richards equation solution and the observations points out the importance of considering the water pressure evolution due to the soil matrix deformation during the landslide triggering. In the first case with loose sand, the Richards solution covers well the real phenomenon, but it fails to identify the pressure head increase at the incipient deformation of the soil matrix soil. A stability analysis based on the undrained soil deformation and the water pressure peak propagation is needed to fully identify the mobilization dynamics and the total soil volume involved.

As regards the second experiment with compacted soil, the experimental data suggest the importance of the expulsion of the air phase as well as the soil matrix deformation. Further experiments are needed to confirm the impact of these processes and to take them into account in future models for landslide prediction.

Bibliography

- Abudi, I., Carmi, G., Berliner, P., 2012. Rainfall simulator for field runoff studies. J. Hydrol., 454-455, 76-81.
- Anderson, S. A., Sitar, N., 1995. Analysis of rainfall-induced debris flows. J. Geotech. Eng.-ASCE, 121, 544-552.
- Assouline, S., El Idrissi, A., Persoons, E., 1997. Modeling the physical characteristics of simulated rainfall: a comparison with natural rainfall. J. Hydrol., 196, 336–347.
- Ballard, D. H., 1981. Generalizing the Hough Transform to detect arbitrary shapes. Pattern Recogn., 13, 111-122.
- Beard, K. V., 1977. Terminal velocity and shape of cloud and precipitation drops aloft. Journal of Atmospheric Sciences, 33, 851-864.
- Beard, K. V., Pruppacher, H. R., 1969. A determination of the terminal velocity and drag of small water drops by means of a wind tunnel. Journal of Atmospheric Sciences, 26, 1066-1072.
- Bilskie, J., 1997. Using dielectric properties to measure soil water content. Sensors Magazine, 14, 26–32.
- Blanquies, J., Scharff, M., Hallock, B., 2003. The design and construction of a rainfall simulator. In: IECA, 34th Annual conference and Expo., Las Vegas, Nevada, February 24–28, 2003.
- Borga M., Dalla Fontana, G., Gregoretti, C. and L. Marchi, 2002. Assessment of shallow landsliding by using a physically based model of hillslope stability. Hydrol Process, 16, 2833-2851.
- Brisco, B., Pultz, T. J., Brown, R. J., 1992. Soil moisture measurement using portable dielectric probes and time domain reflectometry. Water Resour. Res., 28, 1339-1346.
- Brooks, R.H., Corey, A.T., 1964. Hydraulic properties of porous media. Hydrology Papers, Colorado State University, 24 pp..
- Campbell Scientific, 2003. CS616 and CS625 water content reflectometers instruction manual. Campbell Scientific, Logan, UT.
- Campbell, G.S., Anderson, R. Y., 1998. Evaluation of simple transmission line oscillators for soil moisture measurement. Comput. Electron. Agric., 20, 31-44.
- Caracciolo, C., Napoli, M., Porcù, F., Prodi, F., Dietrich, S., Zanchi, C., Orlandini, S., 2012. Raindrop Size Distribution and Soil Erosion. J. Irrig. Drain. Eng., 138, 461-469.

- Carsel, R. F., and R. S. Parrish, 1988. Developing joint probability distributions of soil water retention characteristics. Water Resour Res, 24, 755-769.
- Casadei, M., Dietrich, W. E., and N. L. Miller, 2003. Testing a model for predicting the timing and location of shallow landslide initiation in soil-mantled landscapes. Earth Surf Process Landforms, 28, 925-950.
- Cerda, A., Ibanez, S., Cavlo, A., 1997. Design and operation of a small and portable rainfall simulator for rugged terrain. Soil Technol., 11, 163–170.
- Chirico, G. B., Claps, P., Rossi, F., and P. Villani, 2000. Hydrologic conditions leading to debris-flow initiation in the Campanian volcanoclastic soil. Mediterranean Storms, in: Proceedings of the EGS Plinius Conference, 14–16 October 1999, edited by: Claps, P. and Siccardi, F., Mediterranean Storms BIOS, Cosenza, Italy, 473–484.
- Christiansen, J.E., 1942. Irrigation by sprinkling. Univ. Calif. Agric. Exp. Stn. Bull. 670.
- Crosfield, R., Cavallo, A., Colella, F., Carvel, R., Torero, J.L., Rein, G., 2009. Landing distance of droplets from water mist suppression systems in tunnels with longitudinal ventilation. Advanced research workshop in fire protection and life safety and transporting systems. Santander, 2009.
- Crude, D. M., 1991. A simple definition of a landslide. Bulletin of the International Association of Engineering Geology, 43, 27-29.
- Cruvinel, P.E., Vieira, S.R., Crestana, S., Minatel, E.R., Mucheroni, M.L., Neto, A.T., 1999. Image processing in automated measurements of raindrop size and distribution. Comput. Electron. Agric., 23, 205–217.
- D'Odorico, P., Fagherazzi, S., and R. Rigon, 2005. Potential for landsliding: Dependence on hyetograph characteristics. J. Geophys. Res., 2005, F01007.
- Davis, J. L., Annan, A. P., 1977. Electromagnetic detection of soil moisture: Progress report 1. Can. J. Remote Sens., 3, 76-86.
- Dobson, M. C., and F. T. Ulaby, 1986. Active microwave soil moisture research. IEEE Trans. Geosci. Remote Sens., 24, 23-36.
- Durner, W., 1994. Hydraulic conductivity estimation for soils with heterogeneous pore structure, Water Resour. Res., 30, 211-223.
- Eichenbeger, J., Ferrari, A., and L. Laloui, 2013. Early warning thresholds for partially saturated slopes in volcanic ashes. Comput. Geotech., 49, 79-89.

- Eigel, J. D., Moore, I. D., 1983. A simplified technique for measuring raindrop size and distribution. Transactions of the ASAE 26:1079-1084.
- Esteves, M., Planchon, O., Lapetite, J. M., Silvera, N., Cadet, P., 2000. The 'Emire' large rainfall simulator: design and field testing. Earth Surf. Process. Landforms, 25, 681-690.
- Feyen, J., Jacques, D., Timmerman, A., Vanderborght, J., 1998. Modelling water flow and solute transport in heterogeneous soils: a review of recent approaches. J. Agr. Eng. Res., 70, 231-256.
- Fox, N. I., 2004. Technical Note: The representation of rainfall drop-size distribution and kinetic energy. Hydrol. Earth Syst. Sc., 8, 1001-1007.
- Frattini, P., Crosta, G. B., Fusi, N., Dal Negro, P., 2004. Shallow landslides in pyroclastic soils: a distributed modelling approach for hazard assessment. Eng. Geol., 73, 277-295.
- Gabet, E. J., Mudd, S. M.,2006. The mobilization of debris flows from shallow landslides. Geomorphology, 74, 207-218.
- Haider, A., Levenspiel, O., 1989. Drag coefficient and terminal velocity of spherical and non-spherical particles. Powder Technol. 58–70.
- Hallikainen, M., F. T. Ulaby, M. C. Dobson, M. EI-Rayes, Wu, L. K. , 1985. Microwaved dielectric behavior of wet soil, I, Empirical models and experimental observations. IEEE Trans. Geosci. Remote Sens., 23, 25-34.
- Hansson, K., Lundin, L. C., 2006. Water content reflectometer application to construction materials and its relation to time domain reflectometry. Vadose Zone J., 5, 459-468.
- Highett, C.T., Gusli, S., Cass, A., Besz, W., 1995. An automated laboratory rainfall simulation system with controlled rainfall intensity, raindrop energy and soil drainage. Soil Technol. 8, 31-42.
- Ioannou, D., Huda, W., Laine, A. F., 1999. Circle recognition through a 2D Hough Transform and radius histogramming. Image Vision Comput. 17: 15-26.
- Iverson, R. M., 2000. Landslide triggering by rain infiltration. Water Resour. Res., 36, 1897-1910.
- Iverson, R. M., 2005. Regulation of landslide motion by dilatancy and pore pressure feedback. J. Geophys. Res., 110, F02015.
- Iverson, R. M., Reid, M. E., Iverson, N. R., LaHusen, R. G., Logan, M., Mann, J. E., Brien, D. L., 2000. Acute sensitivity of landslide rates to initial soil porosity. Science, 290, 513-516.

- Iverson, R. M., Reid, M. R., LaHusen, R. G., 1997. Debris-flow mobilization from landslides. Annu. Rev. Eart Pl. Sc., 25, 85-138.
- Iverson, R . M., 1997. The physics of debris flows. Rev. Geophys. ,35 , 245-296.
- Johnson, A. M., 1984. Debris flow. In Slope Instability, ed. D Brunsden, DB Prior, pp. 257–361. New York: Wiley.
- Jones, S.B., Wraith, J.M., Or, D., 2002. Time domain reflectometry measurement principles and applications. Hydrol. Process., 16,141–153.
- Kelleners, T.J., Robinson, D.A., Shouse, P.J., Ayars, J.E., Skaggs, T.H., 2005. Frequency dependence of the complex permittivity and its impact on dielectric sensor calibration in soils. Soil Sci. Soc. Am. J., 69, 67-76.
- Kincaid, D. C., Solomon, K. H., Oliphant, J. C., 1996. Drop size distributions for irrigation sprinklers. Transactions of the ASAE 39, 839-845.
- Kosugi K., 1996. Lognormal distribution model for unsaturated soil hydraulic properties. Water Resour. Res., 32, 2697-2703.
- Krajewski, W.F., Kruger, A., Caracciolo, C., Gole, P., Barthes, L., Creutin, J.D., Delahaye, J.Y., Nikolopoulos, E.I., Ogden, F., Vinson, J.P., 2005. DEVEX-disdrometer evaluation experiment: basic results and implications for hydrologic studies. Adv. Water Resour., 29, 311–325.
- Lanni, C., 2012. Hydrological controls on the triggering of shallow landslides: from local to landscape scale. Ph. D. thesis, University of Trento, Department of Civil and Environmental Engineering, Doctoral School in Environmental Engineering.
- Laws, J. O., Parsons, D. A., 1943. The relation of raindrop size to intensity. Transactions of the American Geophysical Union 26, 452-460.
- Lehmann, P., Or, D., 2012. Hydromechanical triggering of landslides: from progressive local failures to mass release. Water Resour. Res., 48.
- Lepore, C., Arnone, E., Noto, L. V., Sivandran, G., Bras, R. L., 2013. Physically based modeling of rainfall-triggered landslides: a case study in the Luquillo forest, Puerto Rico. Hydrol. Earth Syst. Sci., 17, 13371-3387.
- Luk, S. H., Abrahams, A. D., Parsons, A. J., 1993. Sediment sources and sediment transport by rill flow and interrill flow on a semi-arid piedmont slope, Southern Arizona. Catena 20 (1/2): 93-111.
- Marquardt, D. W., 1963. An algorithm for least-squares estimation of nonlinear parameters. SIAM J. Appl. Math., 11, 431-441.

- Marshall, J. S., Palmer, W. McK., 1948. The distribution of raindrops with size. J. Meteorol., 5, 165-166.
- Meyer, L.D., Harmon, W.C., 1978. Multiple-intensity rainfall simulator for erosion research on roe side slopes. ASAE 77, 100–104.
- Meyer, L. D., McCune, D. L., 1958. Rainfall simulator for runoff plots. Agr. Eng., 39, 644-648.
- Miller, W.P., 1987. A solenoid-operated, variable intensity rainfall simulator. Soil Sci. Am. J., 51, 832–834.
- Montgomery, D. R., Dietrich, W. E., 1994. A physically based model for the topographic control on shallow landsliding. Water Resour. Res., 30, 1153-1171.
- Morin, J., 1993. Soil Crusting and Sealing, FAO Soils Bulletin, vol. 69. Chapter 5.
- Morin, J., Goldberg, S., Seginer, I., 1967. A rainfall simulator with a rotating disc. Trans. Am. Soc. Agric. Eng., 10, 74–79.
- Morrissey, M. M., Wieczorek, G. F., Morgan, B. A., 2008. A comparative analysis of simulated and observed landslide locations triggered by Hurricane Camille in Nelson County, Virginia. Hydrol. Process., 22, 524-531.
- Moriwaki, H., Inokuchi, T., Hattanji, T., Sassa, K., Ochiai, H., Wang, G., 2004. Failure processes in a full-scale landslide experiment using a rainfall simulator. Landslide, 1,277-288.
- Niebling, W. H., Foster, G. R., Nattermann, R .A., Nowlin, J. D., Holbert, P. V., 1981. Laboratory and field testing of a programmable plot-sized rainfall simulator. In Erosion and Sediment Transport Measurement (Proceedings of the Florence Symposium, June 1981). IAHS Publication 133, 405-414.
- Ochiai, H., Okada, Y., Furuya, G., Okura, Y., Matsui, T., Sammori, T., Terajima, T., Sassa, K., 2004. A fluidized landslide on a natural slope by artificial rainfall. Landslide 1:211-219.
- Parsons, A. J., Abrahams, A. D., Luk, S. H., 1990. Hydraulics of interrill overland flow on a semi-arid hillslope, southern Arizona. J. Hydrol., 177(3-4), 255-273.
- Pérez-Latorre, F. J., de Castro, L., Delgado, A., 2010. A comparison of two variable intensity rainfall simulators for runoff studies. Soil Till. Res., 107, 11-16.
- Pierson, T. C., Costa, J. E., 1987. A rheologic classification of subaerial sediment-water flows. See Costa & Wieczorek, pp. 1–12.

- Pierson, T. C., Janda, R. J., Thouret, J. C., Borrero, C. A., 1990. Perturbation and melting of snow and ice by the 13 November 1985 eruption of Nevado del Ruiz, Colombia, and consequent mobilization, flow and deposition of lahars. J. Volcanol. Geoth. Res., 41, 17-66.
- Rahardjo, H., Leong, E. C., Rezaur, R. B., 2002. Studies of rainfall-induced slope failure. Proceedings of the National Seminar, Slope 2002. 27 April 2002. Bandung. Indonesia. 15-19.
- Reid, M. E., Iverson, R. M., Logan, M., Lahusen, R. G., Godt, J. W., Griswold, J. P., 2011. Entrainment of bed sediment by debris flow: results from large-scale experiments. 5th International Conference on Debris-Flow Hazards Mitigation: Mechanics, Prediction and Assessment. Padua, Italy 14-17 June 2011.
- Reid, M. E., LaHusen, R. G., Iverson, R. M., 1997. Debris-flow initiation experiments using diverse hydrologic triggers. Conference paper: International Conference on Debris-Flow Hazards Mitigation: Mechanics, Prediction and Assessment. San Francisco, California 7-9 August 1997.
- Riley, S.J., Hancock, F., 1997. A rainfall simulator for hydrologic and erosion experiments on mines, with an example of its applications at Ranger Uranium Mine, Northern Territory, Australia. The Australasian Institute of Mining and Metallurgy Proceedings 1, 3-8.
- Robinson, D.A., S.B. Jones, J.M. Wraith, D. Or, and S.P. Friedman, 2003. A review of advances in dielectric and electrical conductivity measurement in soil using time domain reflectometry. Vadose Zone J., 2:444-475.
- Topp, G. C., J. L. Davis and A. P. Annan, 1980. Electromagnetic determination of soil water content: Measurements in coaxial transmission lines. Water Resour. Res., 16, 574-582.
- Tossell, R. W., Dickinson, W. T., Rudra, R. P., Wall, G. J., 1987. A portable rainfall simulator. Can. Agr. Eng., 29, 155-162.
- Schmugge, T. J., T. J. Jackson, McKim, H. L., 1980. Survey of methods for soil moisture determination. Water Resour. Res., 16, 961-970.
- Schmugge, T. J., O'Neill, P. E., Wang, J. R., 1986. Passive microwave soil moisture research. IEEE Trans. Geosci. Remote Sens., I4,12-22.
- Simoni, S., 2009. A comprehensive approach to landslide triggering. Ph. D. thesis, University of Trento, Department of Civil and Environmental Engineering, Doctoral School in Environmental Engineering.

- Šimůnek, J., van Genuchten, M. Th., Šejna, M., 2012. Hydrus: model use, calibration, and validation. Transactions of the ASABE, 55, 1261-1274.
- Šimůnek, J., Hopmans, J. W., 2002. Parameter Optimization and Nonlinear Fitting. In: Methods of Soil Analysis, Part 1. Physical Methods, Chapter 1.7, Dane, J. H., Topp, J. W. Third edition, Madison, 139-157.
- Šimůnek, J., M. Šejna, van Genuchten, M. Th., 1998. The HYDRUS-1D software package for simulating the one dimensional movement of water, heat, and multiple solutes in variably saturated media. Version 1.0. IGWMC-TPS-70. Golden, Colo.: Colorado School of Mines, International Ground Water Modeling Center.
- Singh, R., Panigrahy, N., Philip, G., 1999. Modified rainfall simulator infiltrometer for infiltration, runoff and erosion studies. Agric. Water Manage., 41, 167–175.
- Solomon, K. H., Zoldoske, D. F., Oliphant, J. C., 1991. Laser optical measurement of sprinkler drop sizes. In Automated Agriculture for the 21st Century Proc., Chicago, 16-17 December.
- Swanson, N. P., 1965. Rotating boom rainfall simulator. Transactions of the American Society of Agricultural Engineers 8, 71-72.
- Talebi, A., Troch, P. A., Uijlenhoet, R., 2008. A steady-state analytical slope stability model for complex hillslopes. Hydrol. Process., 22, 546-553.
- Tarolli, P., Aronica, G. T., Penna, D., Borga, M., Brigandì, G., 2012. Valutazione della suscettibilità al franamento diffuso per il bacino di Giampilieri (Sicilia). XXXIII Italian Conference of Hydraulics and Hydraulic Constructions, Brescia.
- Tsai, T. L., Chen, H. E., Yang, J. C., 2008. Numerical modeling of rainstorm-induced shallow landslides in saturated and unsaturated soils. Environ. Geol., 55, 1269-1277.
- Uijlenhoet, R., Stricker, J.N.M., 1999. A consistent rainfall parameterization based on the exponential raindrop size distribution. J. Hydrol., 218, 101–127.
- Van Dijk, A. I. J. M., Bruijnzeel, L. A., Rosewell, C. J., 2002. Rainfall intensity-kinetic energy relationships: a critical literature appraisal. J. Hydrol., 261, 1-23.
- Van Genuchten, M. Th., 1980. A closed-form equation for predicting the hydraulic conductivity of unsaturated soils. Soil Sci. Soc. Am. J., 44, 891-898.
- Varnes, D. J., 1978. Slope movement types and processes. In Landslides—Analysis and Control, Transportation Res. Board Special Rep. 176, ed. RL Schuster, RJ Krizek, pp. 11–33. Washington, DC: Natl. Acad. Sci..

- Vaz, C. M. P., Hopmans, J. W., Macedo, A., Bassoi, L. H., Wildenschild, D., 2002. Soil water retention measurements using a combined tensiometer-coiled time domain reflectometry probe. Soil Sci. Soc. Am. J., 66, 1752-1759.
- Vogel, T., Císlerová, M., 1988. On the reliability of unsaturated hydraulic conductivity calculated from the moisture retention curve. Transport in Porous Media, 3, 1-15.
- Watson, K. K., 1965. Some operating characteristics of a rapid response tensiometer system. Water Resour. Res., 1, 577-586.
- Wischmeier, W. H., Smith, D. D., 1958. Rainfall energy and its relation to soil loss. Transactions of the American Geophysical Union, 39, 258-291.
- Wischmeier, W. H., Smith, D. D., 1978. Predicting rainfall Erosion Losses, Agricultural Handbook 537. Science and Education Administration, USDA, Washington, DC 58 pp..